GEOCHEMISTRY OF DIKES AND LAVAS FROM TECTONIC WINDOWS

by

Meagen Ann Pollock

Division of Earth and Ocean Sciences
Duke University

Date:_____
Approved:

_____
Dr. Emily M. Klein, Supervisor

_____
Dr. Alan E. Boudreau

_____
Dr. Drew S. Coleman

_____
Dr. Jeffrey A. Karson

Dissertation submitted in partial fulfillment of
the requirements for the degree of Doctor
of Philosophy in the Division of
Earth and Ocean Sciences in the Graduate School
of Duke University

2007

ABSTRACT

GEOCHEMISTRY OF DIKES AND LAVAS FROM TECTONIC WINDOWS

by

Meagen Ann Pollock

Division of Earth and Ocean Sciences
Duke University

Date:_____
Approved:

_____
Dr. Emily M. Klein, Supervisor

_____
Dr. Alan E. Boudreau

_____
Dr. Drew S. Coleman

_____
Dr. Jeffrey A. Karson

An abstract of a dissertation submitted in partial
fulfillment of the requirements for the degree
of Doctor of Philosophy in the Division of
Earth and Ocean Sciences in the Graduate School
of Duke University

2007

Abstract

Tectonic windows are faulted escarpments that expose extensive sections of *in situ* oceanic crust, providing valuable opportunities to examine upper crustal architecture from a perspective unmatched by other approaches. Recent investigations of tectonic windows by submersible (*Alvin, Nautile*) and remotely-operated vehicle (*Jason II*) have recovered an unprecedented suite of dikes and lavas. We focus on compositions of dikes and lavas from intermediate- and super-fast rate crust exposed, respectively, in the Western Blanco Transform (BT) fault and the Pito Deep Rift (PD), to better understand accretionary processes at mid-ocean ridges.

In the BT, the upper lavas are generally more primitive than the lower lavas, supporting geophysical and geological studies that suggest off-axis volcanism plays an important role in constructing the upper crust at intermediate-rate spreading centers. The wide range in lava compositions exposed along the BT scarp also lends caution to studies that rely on surface lavas alone to determine the evolution of sub-axial magmatic conditions.

The PD suite allows us to examine accretionary processes over an impressive temporal range, including long-term (millions of years) changes in mantle composition and medium-rate (100s of ka) changes in magmatic regime. Compositions of adjacent dikes reveal that the ocean crust is heterogeneous on short time (<10 ka) and spatial (meters) scales, reflecting along-axis transport of magma from chemically heterogeneous portions of the melt lens. High compositional variability was also observed in adjacent dikes from Hess Deep (HD), a tectonic window into fast-rate crust, probably best explained by lateral dike intrusion at all mid-ocean ridges. PD calculated liquid densities of lavas are offset to lower density compositions compared to dikes, an

observation previously made in HD, but made here for the first time in other dike-lava populations, suggesting that buoyancy may play a major role in partitioning magma between dikes and lavas. A model for intrusion of a single dike shows that crustal density, magma pressure, and tectonic stress, among other factors, affect the intensity of density-based magma partitioning in a systematic way that can be related to compositions of dike-lava populations.

Contents

List of Tables

List of Figures

1. Temporal and Spatial Variability in the Composition of Lavas Exposed along the Western Blanco Transform Fault[1]

1.1 Introduction

Our understanding of variations in magma composition at intermediate to fast-rate spreading centers has been based largely on studies of the lava carapace that caps the surface of the igneous ocean crust. Sampling of very young lavas along-axis demonstrates that sub-axial magmatic processes often generate magmas of similar compositions within distinct axial segments, while sampling along a flow-line reveals the evolution of these processes over time (e.g., Batiza et al., 1996; Perfit and Chadwick, 1998; Regelous et al., 1999). In each of these types of studies, it is assumed that the lavas sampled on the surface provide information on the axial processes that produce the crust of that age (i.e., near "zero-age" for along-axis samples; progressively older lavas along a flow-line perpendicular to the axis). The existence of young off-axis volcanism (Perfit et al., 1994; Goldstein et al., 1994) or axial flows extending a few kilometers from the axis (Perfit and Chadwick, 1998; Schouten et al., 1999; Soule et al., 2005), however, clearly complicate this simple approach to studying variations in lava composition through time. In addition, studies of lavas from ophiolites and ODP drill cores reveal that the compositions of lavas within a lava pile may vary significantly with depth below the seafloor. Thus, inferences based on surface sampling of off-axis lavas may provide an incomplete view of the true variability of magmatic processes occurring over a limited time span (Perfit and Chadwick, 1998).

---

[1] Pollock, M.A., E.M. Klein, J.A. Karson, and M.A. Tivey, Temporal and spatial variability in the composition of lavas exposed along the Western Blanco Transform Fault, Geochem. Geophys. Geosyst., 6, Q110009, doi:10.1029/2005GC0001026, 2005.

Ocean drilling and ophiolites provide valuable opportunities to investigate the variability of the ocean crust with depth, but each is limited in its applicability. While much has been learned about the structure and composition of the crust through ocean drilling (e.g., Pariso and Johnson, 1989; Alt et al., 1996), by their nature these drill cores provide only a one-dimensional perspective on the ocean crust. Ophiolites, such as the Troodos ophiolite in Cyprus and the Semail ophiolite in Oman, provide accessible two- and three-dimensional exposures of oceanic lithosphere (e.g., Moores and Vine, 1971; Pallister and Hopson, 1981; Nicolas, 1989), but uncertainties regarding tectonic setting, spreading rate, and emplacement overprinting make ophiolites an imperfect analog for *in situ* ocean crust (Moores and Vine, 1971; Dewey and Bird, 1971; Dilek et al., 2000; Hawkins, 2003).

The study of tectonic windows into the oceanic crust presents an alternative and complement to both drilling and ophiolite studies. Tectonic windows occur at faulted escarpments where kilometer-scale vertical crustal sections of the oceanic crust are exposed. Tectonic windows into intermediate- to fast-spread crust are relatively rare and limited to propagating rifts and major transform faults. Direct observations of the structural, geochemical, and hydrothermal relationships offer insights into ocean crust accretion unmatched by other approaches, provided the effects of exposure mechanisms are recognized (see Karson, 1998 for references and review). Studies of fast-spread crust exposed at the Hess Deep Rift, for example, suggest a 4-D model for accretion in which dikes transport magma along-axis and rapid sub-axial subsidence accommodates thickening of the lava unit (Karson et al., 2002a; Stewart et al., 2002).

The north wall of the Western Blanco Transform (BT) Fault Zone also represents a tectonic window, in this case exposing crust generated at an intermediate-rate

spreading center. This study focuses on the spatial and temporal geochemical relationships among lavas exposed along a 13-km-long portion the BT scarp. These lavas provide information on the processes of crustal accretion that occurred over 400 ka ~1 Ma at the southern end of the intermediate-spreading Cleft Segment of the Juan de Fuca Ridge. Through studies of tectonic windows like the BT, we hope to gain a better understanding the processes that lead to the development of the ocean crust through time.

1.2 Geologic Setting of the Blanco Transform

The BT is a 360 km-long, left-lateral, dextrally slipping transform zone in the northeast Pacific (Figure 1.1; Embley and Wilson, 1992; Karson et al., 2002b). It links the Cleft Segment of the Juan de Fuca Ridge (JdFR) in the north to the Gorda Ridge in the south. A pseudofault trace located about 60 km east of the current JdFR-BT intersection indicates previous southward propagation of the JdFR (Juteau et al., 1995), terminating at the transform between 1.5 and 2 Ma ago (Wilson et al., 1984). Since then, the BT and Cleft Segment have been stable spreading features, separating the Juan de Fuca and Pacific plates. The western portion of the BT, located between the ridge-transform intersection (RTI) and the pseudofault, consists of a deep trough (~4800 mbsl) and a steep northern scarp (45°-50°). The north wall exposes just over 2 km of the upper oceanic crust, including the lava unit and upper portion of the dike unit (Delaney et al., 1987; Karson et al., 2002b). Lavas exposed on the north wall of the BT were erupted along the southern Cleft Segment, which is spreading at an intermediate full rate of 60 mm/yr (Delaney et al., 1981; Riddihough, 1984).

Figure 1.1: (Next Page) (A) Bathymetric map of the western Blanco Transform (100 m contour interval) with regional setting shown in inset. Box defines the boundaries of the study area enlarged in panel B. (B) Bathymetric map (50 m contour interval) of study area. *Alvin* dives from the *Blancovin* program, studied here, are shown in red (M.A. Tivey, unpublished data, 1995); *Blanconaute* (BN) dives, not studied here, are shown in blue (T. Juteau, unpublished data 1991; Naidoo, 1998). Side-scan sonar investigations are located within outlined box at right (Delaney et al., 1987; Naidoo, 1998). Bathymetric maps are modified after Tivey (1996). Inset is modified from the National Oceanographic and Atmospheric Association's Pacific Marine Environmental laboratory "Vents Program" website (http://www.pmel.noaa.gov/vents/).

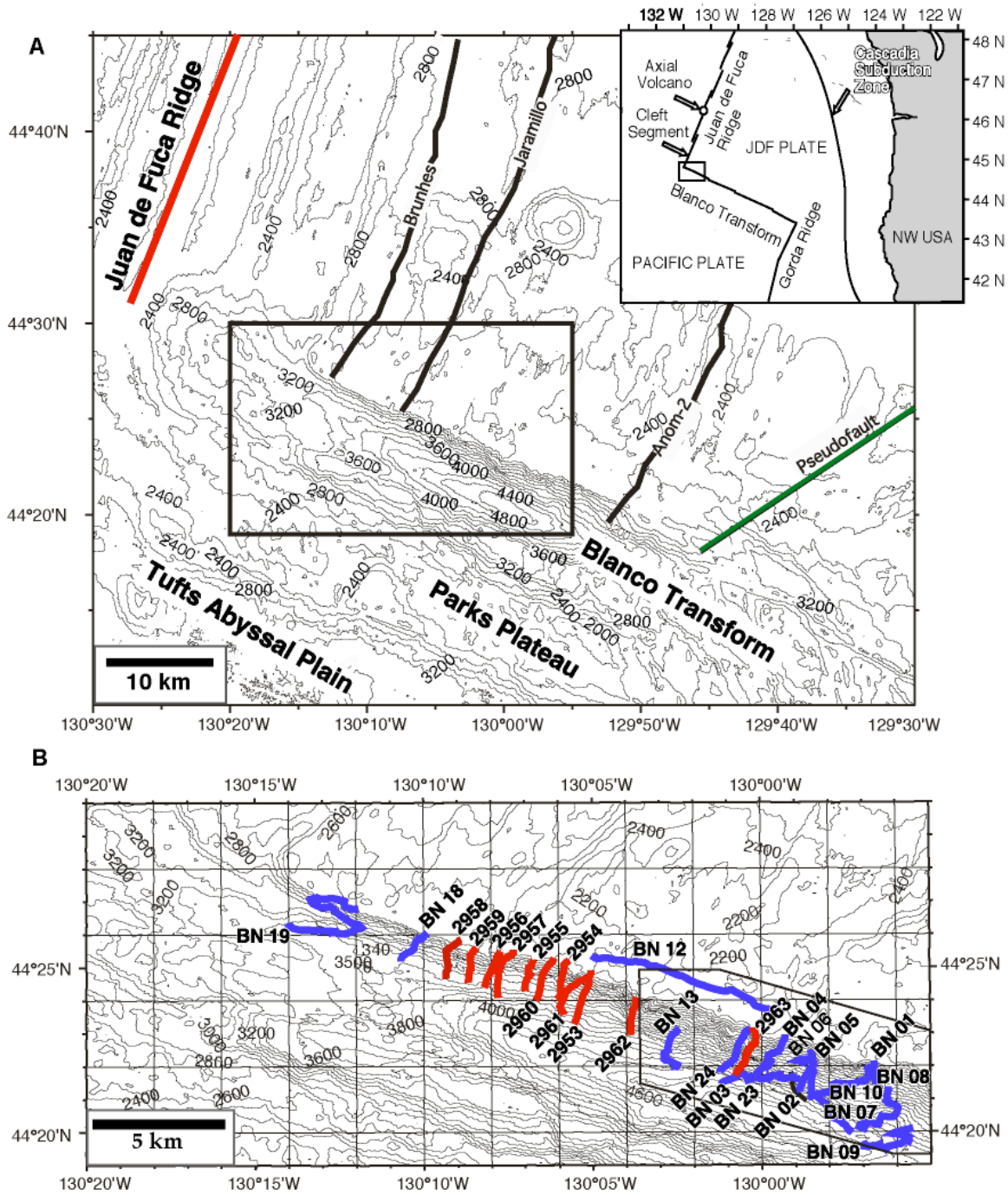
A
Juan de Fuca Ridge
Brunhes
Jaramillo
Anom-2
Pseudofault
Blanco Transform
Parks Plateau
Tufts Abyssal Plain
10 km
44°40'N
44°30'N
44°20'N
130°30'W
130°20'W
130°10'W
130°00'W
129°50'W
129°40'W
129°30'W
132 W
130 W
128 W
126 W
124 W
122 W
48 N
47 N
46 N
45 N
44 N
43 N
42 N
Axial Volcano
Cleft Segment
Juan de Fuca Ridge
JDF PLATE
Cascadia Subduction Zone
Blanco Transform
Gorda Ridge
PACIFIC PLATE
NW USA
B
130°20'W
130°15'W
130°10'W
130°05'W
130°00'W
44°25'N
44°20'N
5 km
BN 19
BN 18
BN 12
BN 13
BN 24
BN 03
BN 23
BN 02
BN 04
BN 06
BN 05
BN 01
BN 08
BN 10
BN 07
BN 09
2958
2959
2956
2957
2955
2954
2960
2961
2953
2962
2963

Previous investigations include extensive sampling by submersible and dredging, geologic observations by side-scan sonar, deep sea and submersible photos, and detailed magnetic profiling of ~30 km of the north wall along the western Blanco scarp (Delaney et al., 1987; Juteau et al., 1995; Tivey, 1996; Tivey et al., 1998; Naidoo, 1998; Karson et al., 2002b). The exposure consists mainly of an extrusive unit, ~900-1000 m thick, underlain by a sheeted dike complex (Figure 1.2; Juteau et al., 1995; Karson et al., 2002b). In general, the upper lavas are undeformed within the upper 200-500 m (exhibiting well-developed pillow and lobate morphologies with rare sheet flows) and grade downward into more fractured lavas. The lava flows dip toward the spreading; the dip of lava flows increases with depth from an average dip of 23.8° in the upper lavas to 37.2° in the lower lavas (Karson et al., 2002b). Beneath the extrusive unit lies the sheeted dike complex, which is exposed for vertical intervals of as much as ~500 m before it is obscured by talus lower on the scarp. Dikes dip away from the spreading axis at angles typically between 40° and 50° (Karson et al., 2002b). Rare exposures of massive, possibly gabbroic rocks were observed beneath the sheeted dike unit (Karson et al., 2002b).

Additional information on the architecture of the upper ocean crust derives from studies of the magnetic reversal boundaries within the lava unit. In a study of the BT, Tivey et al. (1998) showed that magnetic reversal boundaries extend horizontally over ~3-4 km and systematically dip toward the spreading axis (Tivey et al., 1998). In the upper, undeformed lavas, the polarity boundaries dip at shallow angles (<5°), while in the lower lava section, the boundaries have a steeper dip (30°-45°).

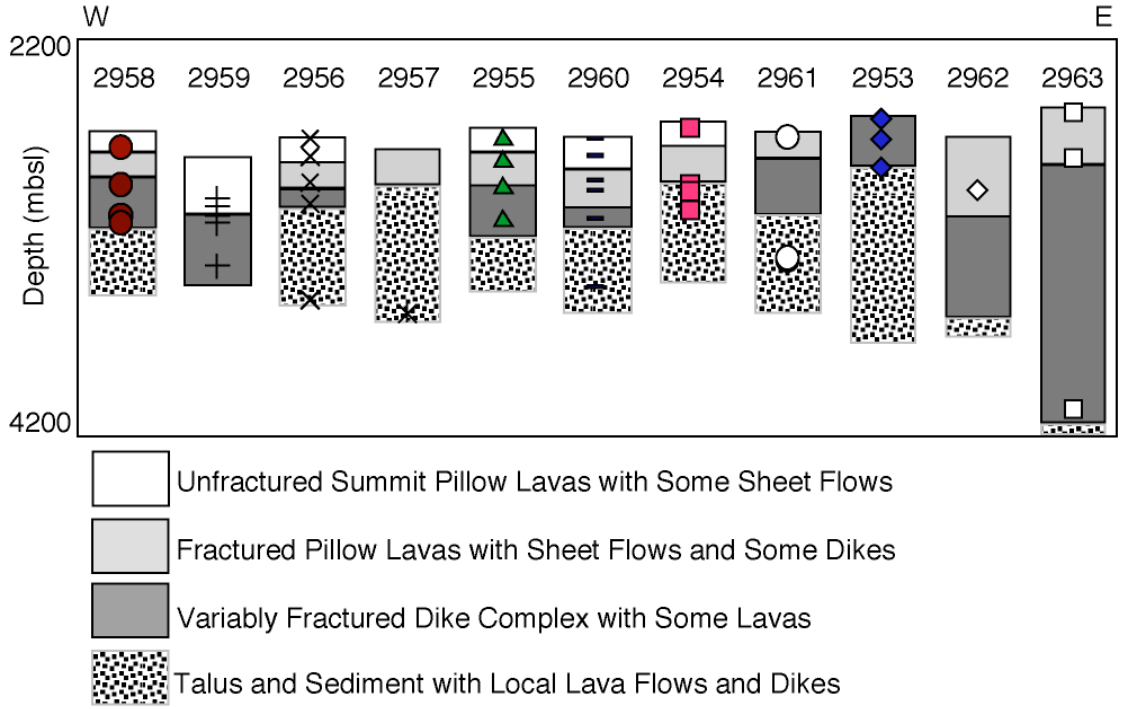

Figure 1.2: Schematic representation of the lithologies observed along the north wall of the BT during the *Blancovin* program. Alvin dive numbers are labeled at the top of the scarp. The dives are ordered across the exposure according to relative distance from the JdFR-BT intersection. Symbols indicate sample locations.

1.3 Sampling and Sample Description

This study focuses on the geochemistry of lavas collected during the 1995 Blancovin dive program to the north wall of the Blanco Transform between 130 º 04'W and 130 º 09'W (Figure 1.1). The dives are located between 24 and 37 km east of the intersection of the southern JdFR and the BT. Eleven *Alvin* dives, spaced approximately 1 km apart, recovered 61 samples from the extrusive unit, including 53 basalts and 8 breccias (Figure 1.2). Each dive traversed ~2000 m of vertical exposure and collected an average of 5 samples. Assuming a constant half-spreading rate of 30 mm/yr for the JdFR (Delaney et al., 1981; Riddihough, 1984), the sample suite spans from 0.8 to 1.2 Ma in age and represents ~400 ka of accretion.

The lavas range in morphology from sheet flows to pillow lavas. Brown alteration rinds penetrate the outer ~1 cm of most of the samples. Millimeter-scale glass rims border some of the lavas. Thin-section observations show that the lavas are aphyric to weakly porphyritic, ranging from 1-9% (by volume) phenocrysts, although most have <3%. Plagioclase is the dominant phenocryst phase and exists as euhedral laths (<1 mm long) or as glomerocrysts in a fine-grained or glassy matrix. Some larger plagioclase grains enclose smaller laths while other large plagioclase crystals show partial resorption textures. Phenocrysts of clinopyroxene occur in some of the more evolved samples while microphenocrysts of olivine are present in some of the primitive samples. Across the range of basalt compositions, the variolitic groundmass consists of clinopyroxene and plagioclase with less abundant opaque oxides and glass. Many of the samples are finely (<1 mm) vesicular (0-10% vesicles).

All of the samples are altered to various extents, as demonstrated by brown alteration rinds and mineral alteration products. Visibly altered material was avoided

during sample preparation by selecting samples with fresh gray interiors and by excluding alteration halos. Of the 53 basalts recovered, 40 samples appeared sufficiently fresh for chemical analysis. Some obviously altered samples (2962-1, 2962-2, 2963-5, 2963-6) were analyzed for comparison, but are excluded from the interpretations. Comparison of the fresh and altered samples reveals the effects of low-temperature seawater alteration (i.e., secondary chlorite and epidote). The altered samples show high (>1.5%) loss on ignition (LOI), a good indicator of alteration by seawater (Alt, 1993). All of the lavas that are considered fresh have LOI <1.5%. Generally, the fresh interiors appear unaltered; however the elements K, Rb, Ba, and Sr may have been mobilized by seawater reactions, as evidenced by their high variability (K, Rb, and Ba concentrations vary more than 100% while Sr abundances vary by ~60%). These elements are excluded from further interpretation.

1.4 Analytical Methods

Major and trace element analyses were performed at Duke University on whole rock powders prepared with an agate mortar and pestle. Major elements (in a 1:4750 dilution) and high-abundance trace elements (in a 1:250 dilution) were measured by direct current plasma emission spectrometry (DCP; Fisons SpecterSpan 7) using a procedure modified after Klein et al. (1991). The standards used for calibration of DCP data were NBS-688, AII92-29-1, and K1919 (similar to BHVO-1). Low-abundance trace element concentrations were analyzed by inductively coupled plasma mass spectroscopy (ICP-MS; VG-Elemental PlasmaQuad 3) using a procedure modified after Cheatham et al. (1993). The standards used for calibration in the ICP-MS analyses were U.S. Geological Survey standards: BHVO-1, BIR-1, DNC, and W2-1. Each run

consisted of repeat analyses of samples (duplicate for DCP runs and triplicate for ICP runs), standards, blank, and a solution to monitor machine drift. Additionally, some samples were prepared in duplicate and analyzed in separate runs.

1.5 Results

1.5.1 Major Elements

The abundance of major and trace elements in the BT lavas are presented in Table 1.1. Unlike glasses, which may be assumed to be equivalent to liquid compositions, whole rock analyses represent melt plus crystals. Generally, the effects of crystal accumulation on the BT lavas appear to be minimal. Plagioclase is the dominant phenocryst phase in the BT lavas, but the effects of plagioclase accumulation (i.e., systematic changes in MgO, FeO*, CaO, Al_2O_3) are only observed in a small number of samples (2958-2, 2956-2). In contrast, evidence of plagioclase fractionation is expressed throughout the BT suite by negative Eu anomalies (Figure 1.4). Elevated abundances of Ni (2958-1, 2956-6) and Sc (2961-4) in a small number of samples also suggest minor accumulation of olivine and clinopyroxene, interpretations corroborated by thin section and hand sample observations.

Compared to the global range in major element compositions, the compositions of the BT lavas generally overlap with and span the variability observed among MORB from the northern EPR (Figure 1.3; Klein and Langmuir, 1987; Klein et al., 1991). The BT samples exhibit substantial overlap with axial and off-axis lavas specifically from the southern JdFR (M. Perfit, pers. comm.), with an average MgO concentration of 6.9±0.9 wt% and an average of 11.5±1.5 wt% FeO*. The BT lavas have Mg# values of 65-40,

Table 1.1: (Next Page) Major and trace element data for whole rock samples from the Blanco Transform. Major element oxides are reported in weight%; trace elements in ppm. FeO* is total Fe recalculated as FeO. Mg# is calculated as cation mole % [Mg/[Mg+Fe)]. Major elements and Sr, Sc, Zn, and V were analyzed by DCP. Reproducibility for DCP analyses is 1-2% for all major and minor elements with the exception of the following: <4% for Zn; <3% for Sc and V. The remaining trace elements were analyzed by ICP-MS, for which the reproducibility is 1-3% for REE and 1-5% for all other elements. Replicate analyses of standards are in agreement with previously published values (see electronic database of Stewart et al., 2002).

Table 1.1 Major and trace element data for Blanco Transform samples

Sample ID	2953-3	2953-5	2953-6	2954-4	2954-5	2954-6	2954-7	2954-8	2955-2	2955-3	2955-7	2955-8	2956-1	2956-2	2956-3	2956-5	2956-6	2957-1
Depth (m)	2679	2456	2336	3039	2896	2877	2877	2412	3053	2881	2644	2494	3645	2932	2797	2581	2498	3784
Latitiude	44.409	44.411	44.413	44.409	44.411	44.412	44.412	44.421	44.416	44.417	44.419	44.421	44.408	44.420	44.421	44.424	44.427	44.403
Longitude	130.086	130.085	130.084	130.099	130.099	130.098	130.098	130.094	130.115	130.114	130.113	130.112	130.136	130.131	130.131	130.129	130.129	130.130
Dist from Axis (km)	32.95	33.00	33.07	31.90	31.90	31.94	31.94	32.32	30.64	30.73	30.78	30.82	28.92	29.33	29.38	29.50	29.52	29.40
SiO_2 (wt%)	51.41	50.40	49.61	50.49	49.69	50.07	49.64	49.83	50.05	50.30	49.98	48.77	50.18	50.21	49.40	49.93	50.27	49.53
TiO_2	2.48	1.74	1.69	1.62	2.86	1.95	1.96	1.49	2.18	2.04	1.40	1.19	2.05	2.43	2.62	1.49	2.68	1.85
Al_2O_3	14.21	14.47	13.92	14.85	12.62	13.80	14.25	14.29	13.94	13.90	15.13	16.17	14.00	14.07	13.69	14.03	13.15	13.88
Fe_2O_3	12.72	11.90	12.72	11.01	16.36	13.23	13.07	10.88	13.36	12.69	10.75	10.10	12.88	13.79	14.55	11.83	14.24	12.96
FeO*	11.45	10.71	11.45	9.91	14.72	11.90	11.76	9.79	12.02	11.42	9.67	9.09	11.59	12.41	13.09	10.65	12.81	11.66
MnO	0.22	0.19	0.20	0.19	0.24	0.21	0.19	0.23	0.21	0.21	0.18	0.17	0.21	0.20	0.22	0.21	0.22	0.21
MgO	5.89	7.16	8.11	7.05	5.96	6.77	6.58	7.68	6.20	6.68	7.32	8.82	6.67	5.93	5.95	7.85	6.33	7.08
CaO	11.19	12.44	11.28	13.19	10.09	11.46	11.33	12.50	11.35	11.52	12.15	12.40	11.70	10.72	10.74	12.51	10.07	11.31
Na_2O	2.83	2.56	2.57	2.76	2.75	2.66	2.77	2.57	2.63	2.48	2.34	2.20	2.66	2.74	2.92	2.53	2.83	2.48
K_2O	0.35	0.08	0.16	0.13	0.28	0.14	0.11	0.16	0.23	0.21	0.17	0.15	0.24	0.25	0.36	0.44	0.35	0.30
Total	101.30	100.95	100.26	101.29	100.83	100.29	99.89	99.61	100.15	100.02	99.42	99.97	100.59	100.35	100.46	100.82	100.14	99.60
Mg#	47.9	54.4	55.8	55.9	41.9	50.3	49.9	58.3	47.9	51.1	57.4	63.3	50.6	46.0	44.8	56.8	46.8	52.0
LOI	0.7	0.1	0.7	0.8	1.1	1.3	1.1	0.5	1.1	0.6	0.3	0.0	0.0	0.3	0.2	0.9	0.2	0.3
Sr (ppm)	124	108	106	131	107	104	108	123	103	90	100	108	112	113	115	103	101	112
Ba	26.27	10.41	10.26	15.06	16.84	11.67	11.85	18.31	13.92	13.98	10.28	10.64	15.31	13.34	28.01	33.81	43.28	16.84
Zn	127	140	93	82	137	101	102	87	116	101	81	72	101	98	120	152	137	98
Cu	59	76	62	63	54	57	68	70	59	55	60	71	62	62	59	52	50	64
Ni	88	98	91	95	65	84	88	102	105	92	93	121	84	88	67	137	114	86
V	441	355	336	351	524	409	389	331	437	420	335	275	374	388	404	506	494	368
Sc	46.1	45.3	43.8	46.3	45.6	46.0	43.9	47.9	46.4	44.3	42.6	37.2	44.9	44.4	44.2	40.1	41.8	45.1
Cr	126	203	146	251	60	157	143	301	169	225	262	310	174	240	95	204	214	184
P	1252	606	810	664	1319	947	972	714	928	946	686	531	925	860	1214	1615	1589	999
Y	58	32	40	35	66	46	44	34	53	48	35	28	46	41	66	76	73	46
Zr	175	98	117	99	192	130	127	99	165	145	111	85	146	116	234	225	233	171
Be	1.40	0.83	0.75	0.74	2.95	1.06	1.01	0.83	3.01	0.99	0.73	0.63	1.05	1.01	1.55	1.67	1.67	1.16
Co	52.5	43.1	46.7	42.0	46.8	44.6	46.9	42.9	48.1	44.7	40.0	44.1	45.4	43.7	45.1	59.4	45.5	45.2
Ga	16.5	13.7	13.4	13.4	16.4	14.1	14.4	13.0	15.0	14.1	13.1	12.2	14.0	13.6	16.4	17.1	17.9	13.9
Rb	3.65	0.79	2.17	1.48	1.94	1.83	1.09	1.84	2.58	2.04	2.37	1.30	1.68	2.34	4.69	9.26	3.32	2.65
Nb	6.63	2.97	3.18	3.45	6.18	3.86	3.81	3.33	4.52	4.07	2.85	2.42	4.71	4.21	6.22	7.55	7.37	4.64
Cs	0.073	0.016	0.016	0.055	0.015	0.015	0.038	0.016	0.049	0.055	0.046	0.021	0.019	0.060	0.070	0.407	0.038	0.018
La	6.38	2.86	3.45	3.46	6.36	4.17	4.04	3.48	4.65	4.28	3.17	2.57	4.78	4.27	7.31	7.97	7.61	4.69
Ce	19.23	9.11	11.25	10.78	19.94	13.24	13.01	10.83	14.59	13.67	10.01	8.05	14.83	13.04	22.57	24.47	23.55	14.45
Pr	3.17	1.57	2.00	1.84	3.43	2.32	2.25	1.83	2.52	2.35	1.70	1.38	2.49	2.22	3.76	4.10	3.97	2.41
Nd	17.26	8.80	10.89	9.99	18.79	12.84	12.47	9.98	13.80	13.09	9.38	7.78	13.33	11.84	19.46	21.93	21.34	12.80
Sm	5.94	3.32	3.80	3.48	6.45	4.64	4.46	3.53	4.88	4.69	3.34	2.77	4.41	4.17	6.44	7.33	7.26	4.36
Eu	1.86	1.18	1.28	1.21	2.00	1.55	1.47	1.20	1.65	1.54	1.15	1.00	1.54	1.41	1.91	2.19	2.18	1.41
Gd	8.38	4.70	5.53	5.01	9.33	6.45	6.33	5.01	7.00	6.77	4.94	3.92	6.50	5.99	9.02	10.48	10.25	6.33
Tb	1.49	0.85	1.03	0.90	1.70	1.22	1.16	0.91	1.33	1.24	0.91	0.74	1.22	1.11	1.65	1.92	1.89	1.14
Dy	9.37	5.43	6.47	5.63	10.61	7.46	7.21	5.64	8.12	7.80	5.75	4.56	7.41	6.84	10.78	11.86	11.80	7.19
Ho	2.00	1.16	1.39	1.22	2.29	1.64	1.57	1.23	1.82	1.69	1.23	0.97	1.60	1.45	2.30	2.56	2.54	1.54
Er	5.70	3.27	3.94	3.48	6.43	4.66	4.52	3.44	4.95	4.84	3.61	2.78	4.59	4.15	6.37	7.33	7.24	4.52
Yb	5.64	3.25	3.84	3.37	6.31	4.59	4.34	3.31	4.93	4.75	3.51	2.71	4.54	4.09	6.50	7.02	7.05	4.24
Lu	0.86	0.51	0.60	0.51	0.99	0.71	0.69	0.52	0.84	0.74	0.54	0.42	0.72	0.65	1.02	1.14	1.13	0.71
Hf	4.58	2.70	3.11	2.65	5.13	3.41	3.40	2.67	4.25	3.91	2.81	2.21	3.68	3.06	5.83	6.14	6.08	4.21
Ta	0.41	0.20	0.21	0.23	0.40	0.27	0.26	0.22	0.30	0.27	0.18	0.18	0.34	0.28	0.42	0.51	0.49	0.31
Pb	0.589	0.235	0.436	0.295	0.596	0.380	0.327	0.431	0.377	0.362	0.310	0.288	0.437	0.327	1.475	1.181	0.671	0.435
Th	0.398	0.169	0.188	0.203	0.356	0.231	0.213	0.203	0.232	0.236	0.184	0.157	0.272	0.260	0.504	0.478	0.468	0.281
U	0.274	0.248	0.655	0.525	0.814	0.401	1.126	0.834	4.152	4.579	0.089	0.137	0.107	0.549	0.762	0.170	0.213	0.949
Zr/Y	3.0	3.0	2.9	2.9	2.9	2.8	2.9	2.9	3.1	3.0	3.2	3.1	3.2	2.8	3.5	3.0	3.2	3.7
La/SmN	0.69	0.56	0.59	0.64	0.64	0.58	0.58	0.64	0.62	0.59	0.61	0.60	0.70	0.66	0.73	0.70	0.68	0.69

Table 1.1 (continued)

Sample ID	2958-1	2958-2	2958-3	2958-5	2959-1	2959-2	2959-3	2959-5	2959-6	2960-1	2960-3	2960-4	2960-5	2960-6	2960-7	2961-2	2961-3	2961-4
Depth (m)	2956	2949	2765	2549	3366	2992	2953	2920	2892	3534	3093	3036	3008	2599	2492	3363	3363	2500
Latitiude	44.425	44.426	44.428	44.429	44.416	44.422	44.422	44.423	44.423	44.405	44.413	44.414	44.415	44.420	44.430	44.403	44.403	44.411
Longitude	130.155	130.155	130.152	130.150	130.144	130.144	130.143	130.143	130.143	130.109	130.108	130.107	130.107	130.103	130.102	130.097	130.097	130.086
Dist from Axis (km)	27.42	27.42	27.64	27.81	28.32	28.33	28.36	28.36	28.36	31.07	31.19	31.24	31.25	31.59	31.64	32.08	32.08	32.92
SiO_2 (wt%)	49.51	49.87	50.03	50.86	50.13	50.42	49.31	50.49	50.47	50.57	50.07	49.54	49.88	50.21	49.18	49.26	48.97	50.09
TiO_2	2.43	2.94	2.16	2.00	2.48	2.35	2.43	2.17	1.73	1.78	1.97	1.82	1.78	1.58	1.36	1.00	1.02	1.55
Al_2O_3	13.20	13.09	13.58	14.04	13.79	13.93	13.52	13.39	14.58	14.30	13.66	13.51	13.40	14.46	14.74	16.16	15.90	14.51
Fe_2O_3	14.58	15.63	13.31	12.07	13.59	12.88	13.99	13.02	12.10	11.95	13.55	13.31	13.43	11.27	10.98	10.20	9.92	11.35
FeO*	13.12	14.07	11.98	10.86	12.23	11.59	12.59	11.72	10.89	10.75	12.19	11.98	12.08	10.14	9.88	9.18	8.93	10.21
MnO	0.21	0.21	0.22	0.20	0.22	0.22	0.22	0.21	0.21	0.20	0.21	0.20	0.20	0.18	0.19	0.16	0.15	0.19
MgO	6.67	5.79	6.47	6.48	6.23	6.43	6.32	6.10	7.03	7.16	7.20	7.61	7.73	7.57	8.37	9.26	8.45	7.30
CaO	10.53	9.82	11.33	11.22	10.73	10.92	10.67	10.88	12.21	12.12	11.28	11.40	11.40	12.54	12.32	12.67	12.73	12.37
Na_2O	2.61	2.76	2.83	2.72	2.79	2.81	2.68	2.68	2.61	2.62	2.56	2.57	2.48	2.55	2.30	2.07	2.12	2.55
K_2O	0.28	0.17	0.21	0.26	0.38	0.34	0.30	0.23	0.26	0.25	0.17	0.11	0.17	0.17	0.14	0.08	0.05	0.11
Total	100.02	100.29	100.14	99.87	100.34	100.31	99.45	99.18	101.21	100.94	100.67	100.08	100.48	100.52	99.58	100.86	99.34	100.02
Mg#	47.5	42.3	49.1	51.5	47.6	49.7	47.2	48.1	53.5	54.3	51.3	53.1	53.3	57.1	60.2	64.3	62.8	56.0
LOI	0.5	0.7	0.2	0.7	1.5	0.2	0.2	0.3	0.4	0.1	1.1	1.1	1.4	0.8	0.2	1.2	1.1	0.0
Sr (ppm)	112	106	108	113	101	138	125	133	110	129	101	112	106	142	108	76	75	106
Ba	19.68	11.45	25.00	16.38	27.20	38.34	23.48	22.56	28.84	17.17	11.33	17.90	11.79	13.00	12.99	5.08	4.79	14.04
Zn	100	81	140	100	128	132	108	113	122	95	107	115	98	102	85	69	70	97
Cu	59	54	46	60	46	70	61	43	59	72	62	63	63	67	75	69	70	59
Ni	129	87	98	92	108	68	94	68	69	84	83	78	77	100	114	139	134	93
V	405	343	506	383	482	436	402	415	434	353	395	368	373	338	314	265	274	357
Sc	44.0	46.3	44.5	45.6	41.6	46.7	45.0	46.9	44.6	47.0	45.0	46.6	45.3	48.5	44.2	36.8	37.7	48.4
Cr	144	183	146	193	163	78	89	82	41	229	113	112	111	279	281	346	345	190
P	886	634	1524	798	1587	1212	1013	997	997	780	814	704	698	680	595	373	377	677
Y	46	34	75	42	68	59	46	51	55	41	45	41	40	37	33	25	26	40
Zr	122	97	220	121	231	214	145	157	159	131	125	119	112	118	89	66	63	119
Be	1.06	0.75	1.55	1.02	1.72	1.35	1.21	3.58	3.63	3.12	2.97	3.08	3.14	2.99	2.21	1.48	1.48	2.59
Co	52.2	42.3	47.8	42.0	44.5	49.0	46.6	42.7	46.9	42.5	43.7	43.8	43.9	44.0	47.8	45.1	43.7	43.3
Ga	14.6	12.4	16.9	14.4	16.7	16.6	14.8	15.3	15.6	14.5	13.9	14.1	13.1	13.2	13.2	11.6	11.4	13.7
Rb	2.81	0.72	1.76	2.61	3.27	2.93	2.37	3.20	2.38	1.95	1.21	0.76	2.33	2.27	1.41	0.89	0.55	1.16
Nb	3.88	3.10	7.02	4.13	7.28	5.47	5.43	5.72	4.97	4.28	3.83	3.97	3.86	3.61	2.72	1.82	1.78	3.34
Cs	0.092	0.009	0.028	0.029	0.051	0.072	0.039	0.169	0.034	0.025	0.018	0.015	0.022	0.024	0.019	0.029	0.022	0.058
La	3.99	3.12	7.53	4.22	7.52	6.06	5.27	5.74	5.26	4.40	4.14	3.98	3.95	3.76	2.85	1.90	1.91	3.45
Ce	12.59	9.82	22.95	12.98	23.38	18.87	16.26	16.22	16.55	13.28	12.66	11.98	11.91	11.13	8.82	5.75	5.99	10.71
Pr	2.19	1.69	4.07	2.25	4.05	3.21	2.61	2.75	2.82	2.31	2.20	2.08	2.08	1.93	1.54	1.02	1.06	1.89
Nd	12.14	9.27	22.00	12.24	21.64	17.11	14.06	14.86	15.44	12.85	12.52	11.22	11.28	10.56	8.66	5.67	5.91	10.45
Sm	4.29	3.22	7.47	4.16	7.31	5.89	4.90	4.80	5.28	4.21	4.27	3.88	3.84	3.69	3.04	2.21	2.27	3.74
Eu	1.38	1.13	2.21	1.41	2.16	1.86	1.53	1.66	1.71	1.41	1.45	1.29	1.29	1.23	1.10	0.79	0.85	1.24
Gd	6.21	4.84	10.59	6.00	10.16	8.62	6.61	7.12	7.68	5.99	6.38	5.68	5.63	5.18	4.46	3.32	3.42	5.36
Tb	1.13	0.91	1.94	1.10	1.88	1.57	1.24	1.26	1.37	1.09	1.14	1.00	1.03	0.91	0.82	0.62	0.63	0.99
Dy	7.07	5.63	12.17	6.97	11.39	9.80	7.50	7.96	8.72	6.63	7.07	6.40	6.44	5.68	5.25	4.01	4.06	6.26
Ho	1.48	1.19	2.57	1.48	2.45	2.08	1.57	1.74	1.92	1.50	1.55	1.34	1.38	1.30	1.14	0.87	0.92	1.39
Er	4.46	3.41	7.26	4.33	6.85	5.91	4.58	4.83	5.28	4.03	4.39	3.85	3.81	3.47	3.14	2.42	2.50	3.75
Yb	4.32	3.20	6.94	3.98	6.49	5.65	4.32	4.64	5.22	4.01	4.36	3.83	3.60	3.47	3.13	2.45	2.53	3.81
Lu	0.68	0.53	1.14	0.63	1.08	0.95	0.72	0.74	0.84	0.64	0.70	0.61	0.57	0.55	0.48	0.39	0.38	0.58
Hf	3.28	2.58	5.64	3.21	6.13	5.44	3.78	3.94	4.35	3.46	3.41	3.00	2.89	2.93	2.37	1.74	1.72	3.07
Ta	0.26	0.21	0.46	0.29	0.51	0.38	0.35	0.39	0.33	0.31	0.26	0.25	0.22	0.22	0.18	0.12	0.13	0.24
Pb	0.373	0.190	0.957	0.390	0.696	0.715	0.877	0.426	0.677	0.418	0.400	0.746	0.327	0.352	0.410	0.117	0.138	0.451
Th	0.220	0.168	0.413	0.238	0.436	0.364	0.316	0.337	0.263	0.243	0.213	0.224	0.228	0.197	0.157	0.100	0.195	0.189
U	2.474	0.072	1.850	0.108	0.212	0.268	3.079	0.838	6.446	0.481	0.554	0.078	0.074	0.229	0.926	0.440	0.521	0.197
Zr/Y	2.7	2.8	3.0	2.9	3.4	3.6	3.2	3.0	2.9	3.2	2.8	2.9	2.8	3.2	2.7	2.6	2.5	3.0
La/SmN	0.60	0.62	0.65	0.65	0.66	0.66	0.69	0.77	0.64	0.67	0.63	0.66	0.66	0.66	0.61	0.55	0.54	0.60

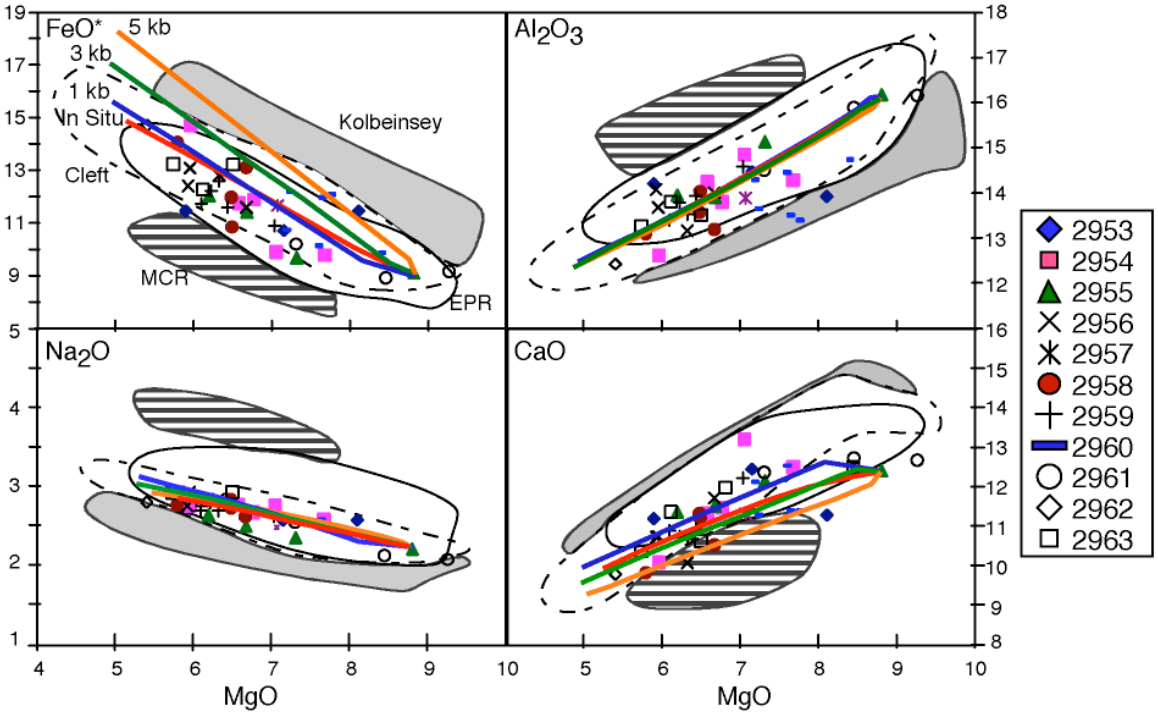

Figure 1.3: Major element variations for the Blanco Transform samples. Clockwise from top left: FeO*, Al_2O_3, CaO, and Na_2O versus MgO (wt%). The samples are identified by dive as in Figure 1.2. Symbols are larger than analytical error (± 1σ). Fields show global range in N-MORB compositions from the Kolbeinsey Ridge (gray), Mid-Cayman Rise (MCR; horizontal stripe), and northern East Pacific Rise (EPR; unshaded). MORB from the Cleft Segment (dashed line) overlap with the northern EPR field. Data for the Kolbeinsey Ridge, MCR, and EPR are from the Ridge Petrological Database of the Ocean Floor (petdb.ldeo.Columbia.edu/petdb/). Data from the Cleft Segment are from PetDB and M. Perfit (pers. comm.) and include both on and off-axis samples, which extend the Cleft Segment field to more evolved compositions. Liquid lines of descent (LLDs) are calculated using the program of Weaver and Langmuir (1990) for 1-kb (blue), 3-kb (green), and 5-kb (orange) fractional crystallization. The data are best described by up to 60% crystallization at ~1 kb with final proportions of plag:ol:cpx of approximately 50:14:36. The LLD produced by *in situ* crystallization (red) is also shown. The *in situ* curve is calculated using the methods of Reynolds and Langmuir (1997) and Stewart et al. (2002). All models are calculated under anhydrous conditions. The primitive BT sample 2955-8 is used as a parental composition. This composition is not considered primary, but may be a parental melt candidate as it is one of the most primitive compositions sampled in the BT suite. The more magnesian samples 2961-2 and 2961-3 were modeled but provided poor fits to the data because of low Na_2O concentrations.

representing relatively primitive to moderately evolved samples (Hess, 1989). Major element variations display typical low-pressure (1 kb) crystallization trends for a tholeiitic magma of increasing FeO*, TiO_2, and Na_2O and decreasing Al_2O_3 and CaO with decreasing MgO. Eleven of the samples, classified as FeTi basalts (FeO* >12%, TiO_2 >2%; Byerly, 1980), are among the most evolved in the suite with Mg#s less than 48.

Liquid lines of descent (LLDs) were calculated, using the program of Weaver and Langmuir (1990) and primitive BT sample 2955-8 as the parent composition (MgO ~9.0 wt%, Mg# 63; Figure 1.3). The successive crystallization and fractionation of olivine, followed by olivine + plagioclase, then olivine + plagioclase + clinopyroxene from the assumed parent magma produces a characteristic tholeiitic differentiation trend for the BT major element data, which are best described by up to 60% crystallization. To first-order, the 1-kb fractional crystallization LLD approximates most of the data; however, at a constant value of MgO, the samples show variability in other oxides that cannot be reproduced by variations in the pressure of crystallization, suggesting that fractional crystallization of a single parent is not the sole process affecting this suite of lavas. Lavas collected from the axis of the Cleft Segment exhibit similar trends in crystallization (Smith et al., 1994).

1.5.2 Trace Elements

Based on REE data, all of the lavas recovered along the north wall of the Blanco scarp are normal MORB (N-MORB; Sun and McDonough, 1989; Figure 1.4). The BT lavas are depleted in the highly incompatible elements and light rare earth elements (La/Sm_N of 0.65 ±0.06), but show relatively flat trends in the moderately incompatible elements (e.g., Zr/Y of 1.22 ±0.11), patterns similar to those of axial lavas from the

Cleft Segment (Smith et al., 1994). REE abundances normalized to chondritic values (Sun and McDonough, 1989) reveal patterns that are consistent with the effects of fractional crystallization (Figure 1.4). In general, more evolved lavas with low Mg# have higher abundances of REE and more negative Eu anomalies.

Incompatible trace elements abundances plotted vs. MgO also exhibit the effects of low-pressure (1 kb) fractional crystallization (Figure 1.5). However, the data show enrichments in incompatible elements with increasing fractionation that cannot be explained by simple crystal fractionation alone. Complex crystallization models, such as *in situ* crystallization, have been invoked to explain similar large enrichments in incompatible elements (Langmuir, 1989). In this process, crystallization occurs within a boundary layer, creating an evolved liquid that is incorporated into the remaining less evolved melt in the magma chamber. The net effect of *in situ* crystallization is to enrich incompatible elements in the magma chamber to a greater extent than predicted by simple Rayleigh fractionation.

The iterative methods of Reynolds and Langmuir (1997) and Stewart et al. (2002) were used to model the effects of *in situ* crystallization (Figure 1.5). The LLD produced by *in situ* crystallization results in enrichments in incompatible trace elements that are more consistent with the observed data. Based on this crystallization model, the compositions of the most evolved samples are best described by 70% crystallization in a system with a boundary layer that constitutes 5% of the melt lens in which 35% crystallization occurs. Sample compositions that vary between the LLDs may be the result of mixing of melts affected by the two different crystallization processes (Dixon et al., 1986; Smith et al., 1994).

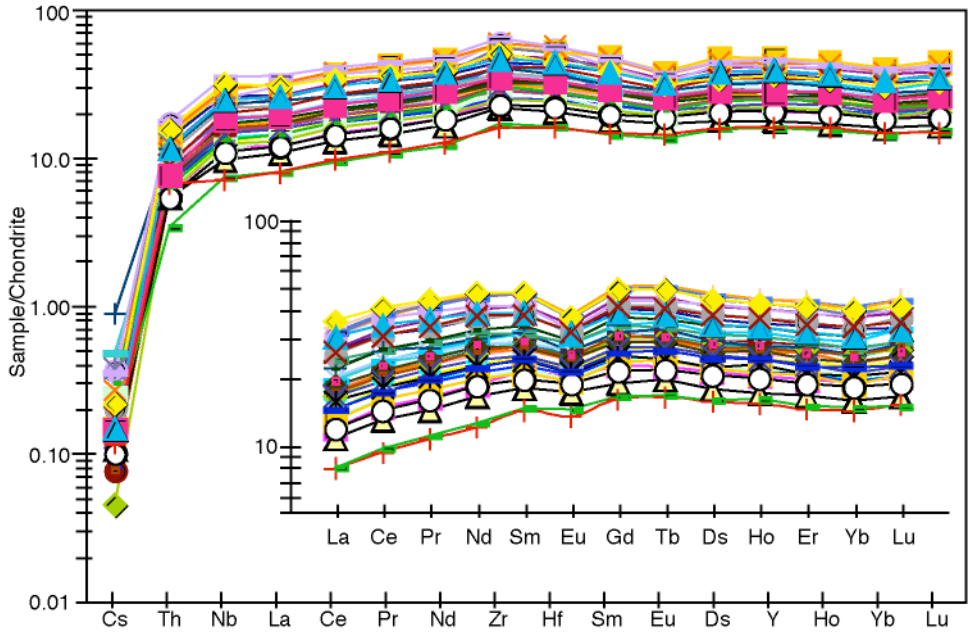

Figure 1.4: Chondrite-normalized trace element abundances (Sun and McDonough, 1989) in order of increasing compatibility for the BT lavas. Inset shows chondrite-normalized rare earth elements (REE). All of the BT lavas are incompatible-element depleted N-MORB (La/Sm_N<1). The REE trends are consistent with the effects of fractional crystallization, with increasing abundances of REE and more negative Eu anomalies in the more evolved samples.

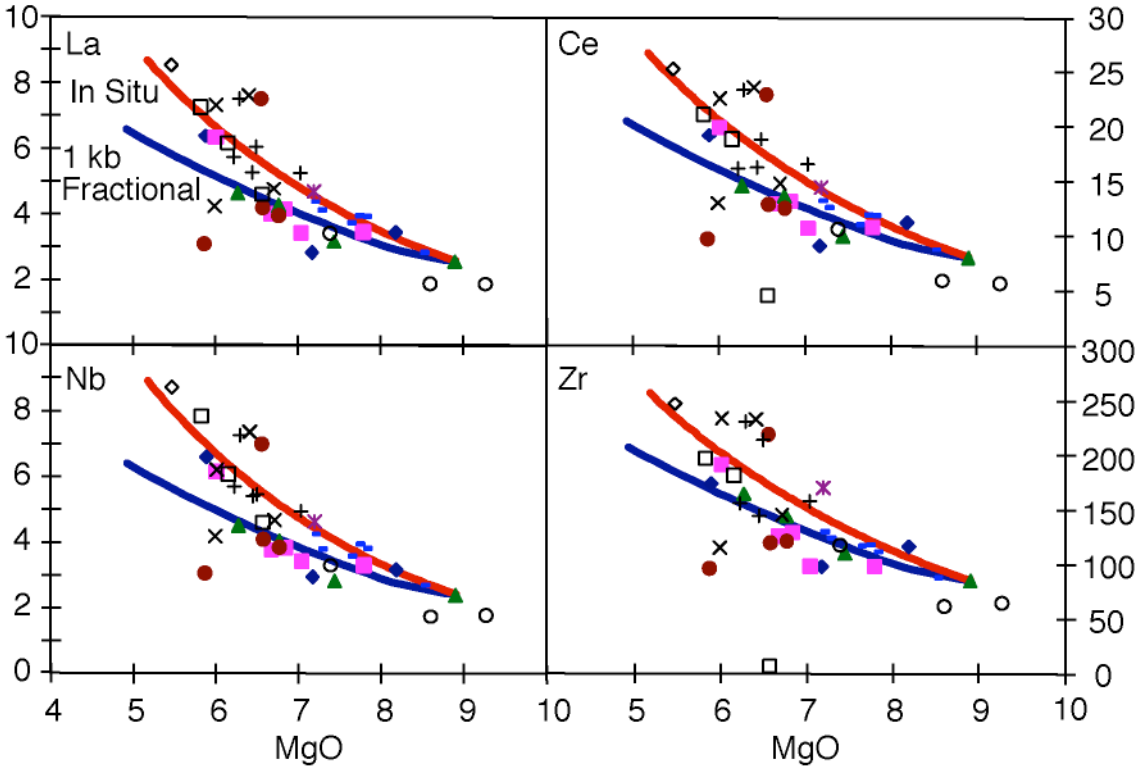

Figure 1.5: Selected trace element concentrations for the BT lavas. Clockwise from top left: La, Ce, Zr, and Nb (ppm) versus MgO (wt%). Symbols as in Figure 1.3. Symbols are larger than the analytical error (± 1 σ). The liquid line of descent produced by *in situ* crystallization is shown in red; the blue line indicates 1-kb fractional crystallization. Partition coefficients used in the calculation are from Bedard (1994). The data are best described by 70% crystallization in a system with a boundary layer that constitutes 5% of the melt body and in which 35% crystallization occurs.

While coupled fractional and *in situ* crystallization capture the bulk of the compositional diversity of the BT lavas, the samples also exhibit small but systematic variability in the ratios of various incompatible trace elements. Ratios of elements with similar incompatibilities (e.g., La/Sm_N, Zr/Y) are relatively insensitive to realistic amounts of crystallization (<70% crystallization; Gast, 1968) and are only slightly modified by melting (Shaw, 1970; Minster and Allegre, 1978). Thus, the correlated variability in these ratios (e.g., Zr/Y from 2.5 to 3.7; La/Sm_N from 0.54 to 0.79)) suggests that the BT lavas have likely experienced some mixing of melts derived from a heterogeneous mantle source. This finding is also consistent with data for axial lavas collected from the Cleft Segment (Smith et al., 1994).

1.5.3 Comparison of Blanco Transform Lavas to Lavas erupted along the Cleft Segment

The similarity in major and trace element compositions between the ~1Ma lavas exposed within the BT and near zero-age lavas sampled at the surface along the southern Cleft Segment suggests that petrogenetic conditions along the Cleft Segment have remained relatively stable over the past ~1 Ma (Figure 1.6). In particular, both suites are dominated by the effects of fractional crystallization and appear to have experienced a similar range of crystallization at shallow depths (~1 kb; Dixon et al., 1986; Smith et al., 1994; Tierney, 2003; Stakes et al., 2005).

Indeed, most of the previous geochemical work along the Cleft Segment has focused on the substantial and spatially systematic trend in the extent of low-pressure crystallization (Figure 1.6; Dixon et al., 1986; Smith et al., 1994; Tierney, 2003; Stakes et al., 2005). Lavas from the northern Cleft region (north of 44°41′N; >25 km from the RTI) are largely primitive and restricted to a relatively narrow range in extent of fractionation

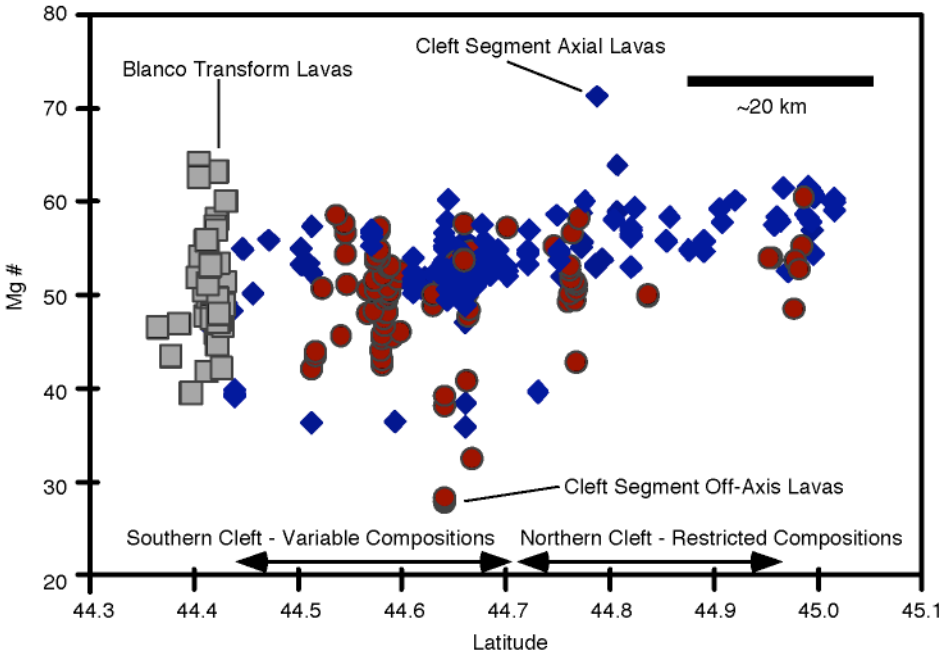

Figure 1.6: Basalt Mg# vs. latitude for axial and off-axis lavas collected along the Cleft Segment and lavas from the BT. Cleft Segment data (blue diamonds represent on-axis samples; red circles represent off-axis samples) are from Dixon et al. (1986), Smith et al. (1994), Tierney (2003), and M. Perfit (pers. comm.). BT lavas (gray squares) are data from this study. On average, the Cleft Segment samples show a southward decrease in Mg#; while relatively primitive lavas are erupted along the length of the segment, the maximum extent of fractionation increases southward. Lavas become more diverse ~23 km north of the RTI, extending to highly evolved compositions toward the RTI (Stakes et al., 2005). This break in lava diversity divides the Cleft Segment into two distinct magmatic sections, the northern and the southern Cleft segments. Data from the BT overlap much of the range defined by the southern Cleft Segment lavas.

(Mg# 50-62), suggesting a steady-state magmatic system with sufficient melt supply to prevent magmas from cooling to great extents (Smith et al., 1994). Lavas from the southern Cleft Segment, however, are more diverse (Mg# 35-60) and evolved, reaching maximum extents of fractionation in the RTI where dacitic lavas were recovered (Smith et al., 1994; Cotsonika et al., 2005; Stakes et al., 2005). The greater range in fractionation among the southern Cleft lavas suggests that low magma flux and/or greater cooling rates, possibly resulting from proximity to the RTI (Fornari et al., 1983; Perfit et al., 1983; Sinton et al., 1983), lead to the existence of discrete, temporally and spatially evolving sub-axial magma bodies (Smith et al., 1994; Canales et al., 2005). The overall similarity between the lava compositions from the BT and those from the southern Cleft Segment, including their wide ranges in fractionation (Mg#s of ~35-65), suggests that the BT lavas formed in a regime of low magma flux and/or high cooling rate similar to that beneath the present axis of the adjacent southern Cleft Segment.

1.6 Discussion

1.6.1 Construction of the Upper Crust: Temporal and Spatial Relationships along the BT Scarp

To explore the spatial and temporal relationships among the lavas exposed along the BT, it is important to understand how the upper crust is constructed. The complexity of this is illustrated by the fact that even the deepest lavas exposed along the scarp originally erupted on the seafloor and must have subsided during spreading. Thus, the upper crust is constructed by a combination of horizontal transport during seafloor spreading and vertical transport due to subsidence. Useful insights into these processes can be derived from geophysical and geological studies of the BT and other tectonic windows.

Magnetic structures and geologic observations along the BT scarp (and other tectonic windows) suggest a model for crustal evolution in which the crust generated at the southern JdFR experiences rapid subsidence near the axis (within ~1-3 km) shortly after formation (Figure 1.7; Tivey, 1996; Tivey et al., 1998; Karson et al., 2002b). As a result, the lava flows erupted on-axis tend to tilt toward the spreading center. As lateral spreading proceeds, axial lavas subside to greater depths, forming the base of the extrusive section, and flows dip toward the axis at increasingly steeper angles. Lavas can also be emplaced farther from the axis by voluminous flows that are channeled away from the axis or erupted beyond the axial valley (e.g., Hooft et al., 1996; Perfit and Chadwick, 1998; Soule et al., 2005). Such lavas, because they are removed from the region of greatest subsidence (i.e., the ridge axis), will experience less subsidence than axial lavas and will dip toward the axis at a shallower angle. The result is a vertical sequence of lavas in which the lava flows dip toward the spreading center and the dips increase with depth. In terms of time variability in the upper crust, isochrons delineating lava flows of near-equal age would be expected to follow similarly curved paths that dip toward the spreading center.

This model for construction of the extrusive unit of the ocean crust, which takes into account not only seafloor spreading (horizontal transport away from the axis) but also crustal subsidence (vertical transport downward), has important implications for both the spatial and temporal relationships among lavas exposed along the BT. With respect to spatial relationships, the model asserts that the base of the extrusive section is formed by lavas erupted on-axis and subsequently buried. In contrast, the upper lavas, which cap the extrusive unit, represent a combination of axially erupted lavas, voluminous off-axis flows, and lavas erupted off-axis through the crust. This suggests that flow-line studies, which of necessity sample the upper lava carapace, may

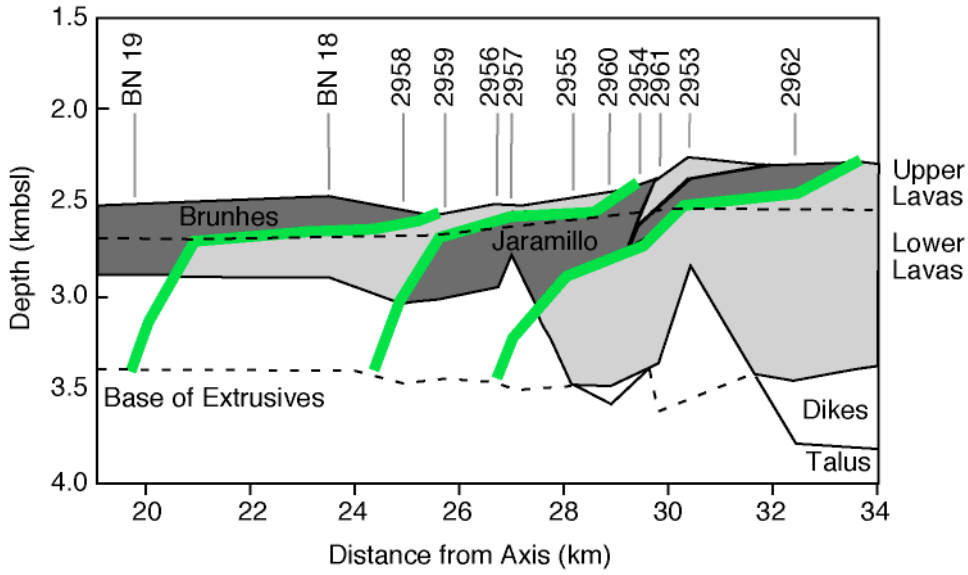

Figure 1.7: Schematic cross-section of the Blanco scarp (modified after Tivey et al., 1998). Green lines depict isochrons, which are determined from boundaries between lavas with opposite magnetization polarities (light field = normal polarity; dark field = reverse polarity). The dotted black lines show the boundaries between lithologic units (division between upper and lower lavas; and between lavas and dikes). *Alvin* dive locations are shown by vertical gray lines labeled with dive number.

represent a biased sampling of the true diversity of magma compositions because they preferentially sample flows that are emplaced farther from the axis, while axial lavas, which form the base of the extrusive section, are more likely to be buried. In this sense, the lavas exposed along the BT should provide a more representative sampling of the diversity of magmas that form the crust.

In regard to temporal relationships, as noted above, isochrons representing lavas of approximately equal age form curved trends that dip toward the spreading center. Thus, in order to examine chemical variations in lava composition through time, the most useful traverse to explore is one that trends perpendicular to the isochrons (because this represents both the most rapid changes in time with distance, and a succession of superimposed lavas). This time sequence trends diagonally through the crust, dipping away from the axis, with oldest lavas deepest and farthest from the axis and youngest lavas, of course, at the surface on-axis. While it is true that a vertical section through the upper ocean crust, such as a drill core, also represents increasing age with depth, according to the model described above, each overlying lava was emplaced further off-axis than the one below it, an effect that is minimized for traverses that are perpendicular to isochrons.

1.6.2 Comparison of Temporal and Spatial Variations in the Cleft Segment and BT Lavas

Samples recovered from the southern Cleft Segment are surface lavas, which are commonly assumed to reflect recent magmatic conditions. Similarly, surface lavas sampled along a flow-line extending away from the axis are assumed to reflect changing (or unchanging) conditions in the magma reservoir system beneath the ridge through time (e.g., Batiza et al., 1996; Regelous et al., 1999). Although this simple view of crustal

accretion may be complicated by off-axis volcanism or along-axis diking (e.g., Perfit et al., 1994; Stewart et al., 2003), studies of samples collected along flow-lines elsewhere have revealed systematic changes in the composition of lavas. These chemical patterns are often symmetrical about the axis, consistent with a temporally evolving magma reservoir system beneath a given axial location (e.g., Batiza et al., 1996).

Previous investigations along the Cleft Segment have produced an extensive suite of axial and off-axis lavas, including samples collected along approximate flow-lines extending both east and west of the axis (Smith et al., 1994; Tierney, 2003; Stakes et al., 2005). Spatial analysis of data for the entire Cleft Segment shows that the lavas sampled off-axis are generally more evolved than those recovered from the axis (Tierney, 2003; Stakes et al., 2005). This spatial distribution of evolved and primitive lavas can be interpreted as reflecting a change in sub-axial magmatic conditions over time (Reynolds et al., 1992; Batiza et al., 1996), in which the older, more evolved lavas were erupted under conditions of waning magmatic activity while the younger, primitive lavas were erupted during more robust magmatism.

An examination of the flow-line traverses for the southern Cleft Segment, however, reveal complex relationships that cannot be easily explained by temporal evolution (Stakes et al., 2005). For example, two flow-lines extending to the east show a general decrease in Mg# with distance from the spreading center, but one flow-line resets to higher values of Mg# within 2 km of the axis. In contrast, a flow-line extending to the west shows an increase in Mg# with distance from the axis. If indeed the flow-line data represent an age-sequence, where age increases with distance from the axis, they demonstrate that separate portions of the southern Cleft Segment experience differing evolutionary histories.

The BT scarp, which exposes the upper crust along an approximate flow-line,

allows us to explore evidence of the temporal evolution of the southern Cleft Segment ~1 Ma ago. Figure 1.8 shows the magnetic isochrons along the BT scarp as well as spatial variations in Mg# for the BT lavas. As a whole, the data are spatially variable and do not appear to form regular trends, apart from the finding that relatively primitive lavas tend to cluster shallower and toward the center, while more evolved lavas cluster deeper and toward the west and east.

Recall that the model for crustal construction predicts that lavas representing age progressions should lie along sections perpendicular to the isochrons. Based on our present sampling of the BT, no systematic temporal changes are observed. While this is disappointing, it is perhaps not surprising for a number of reasons. First, our sample coverage is quite sparse, averaging ~2 samples/km^2. In addition, the only significant form of chemical variability in this data set is one of fractionation, and individual lava flows in other areas are known to display significant chemical variations across small spatial scales, particularly with respect to fractionation (Perfit et al., 1994; Sinton et al., 2002). Lastly, in the absence of detailed age dating of the lavas, it is not known to what extent the lava carapace has been capped by off-axis eruptions, complicating the assumption of simple superposition of successive lavas.

Indeed, Stakes et al. (2005) argue that the evolved, off-axis lavas sampled along the Cleft Segment represent flank eruptions that tap the cooler, more fractionated edges of the magma chamber and periodically cap the more primitive axial lavas. Furthermore, they suggest that the upper lavas exposed in the BT scarp are analogous to the off-axis lavas sampled along the Cleft Segment. This idea can be explored in the context of the model for crustal construction developed above.

The model for crustal construction asserts that lavas erupted on-axis experience more subsidence than lavas emplaced farther from the axis. Thus, the total amount of

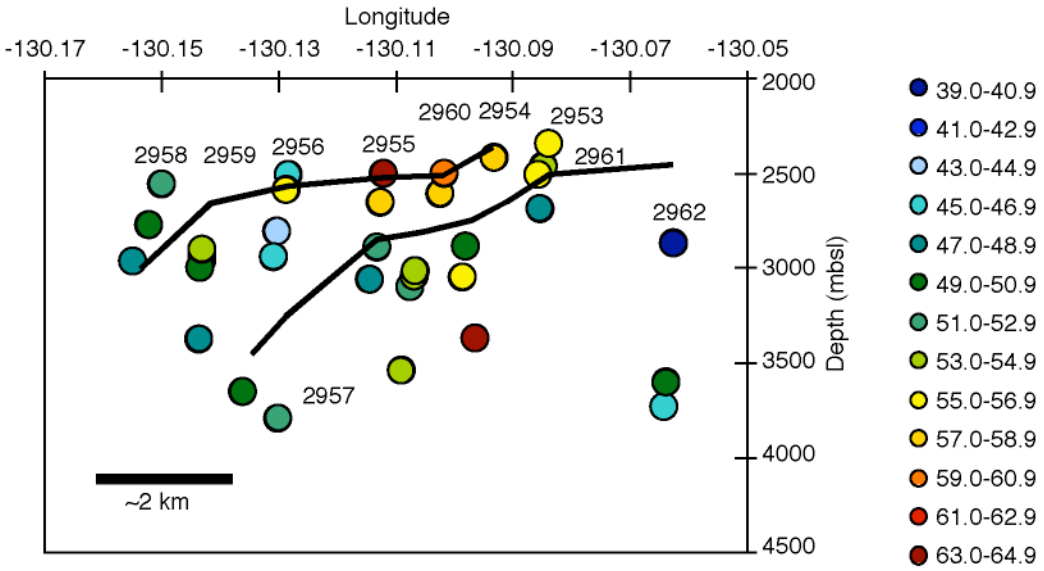

Figure 1.8: Longitude (ºW) versus depth (m) for Blancovin samples located within area shown in Figure 1.2. Samples are color-coded by Mg#; blue samples are the most evolved in the suite (Mg# 39.0-40.9); red samples are the most primitive (Mg# 53.0-54.9). Solid black lines indicate magnetic isochrons from Tivey et al. (1998) and Figure 1.7. Dive numbers are indicated near the end of each dive with the exception of dive 2957, which only includes 1 sample analyzed here, and dive 2963, which is located ~5 km outside of the area shown. Primitive samples tend to cluster at shallow depths in the central portion of the study area, while more evolved samples predominate at depth and toward the east and west.

subsidence determines the orientation of the isochrons while the 'width' of the isochrons (the distance that they extend off-axis) represents the approximate half-width of the zone of magmatic construction. If volcanic construction is confined to a narrow, 3 km-wide neovolcanic zone, the resultant isochrons are relatively short (extending ~1.5 km off-axis) and follow curvilinear paths that dip steeply toward the spreading center (Figure 1.9A). Assuming a significantly wider zone of lava emplacement (up to 4 km from the axis), the isochrons are elongated and dip toward the axis at shallow angles in the upper lavas, which are emplaced up to kilometers from the axis and have experienced little to no subsidence (Figure 1.9B).

Along the BT scarp, the magnetic isochrons in the lower lava unit dip steeply toward the axis (at angles between 30° and 45°; Tivey et al., 1998), approximately the same as the dip of the lower lava flows (Karson et al., 2002b), suggesting that these lavas are the product of axial eruptions (Figure 1.7). In the upper lavas, the isochrons dip at a much shallower angle, suggesting that these lavas were emplaced farther from the axis. Although the magnetic reversal boundary in the upper lavas dips at angles < 5°, much shallower than the observed average flow dip of 23.8°, such a discrepancy could result from a difference in scale: the magnetic reversal boundary is less complicated than the actual dips of lava flows, presumably due to the fact that the reversal boundaries are smoothed by the ~1 km transect spacing while individual lava orientations can vary over lateral distances of meters due to irregularities in surface topography or later faulting. While the shallow dip of the magnetic reversal boundary in the upper lavas along the BT appears to suggest a wider zone of accretion than that inferred from the lava orientations, the change in slope of the isochrons also corresponds with the lithologic boundary between the upper (undeformed, shallowly dipping) lavas and lower (deformed, steeply dipping) lavas. Thus, the geologic and geophysical

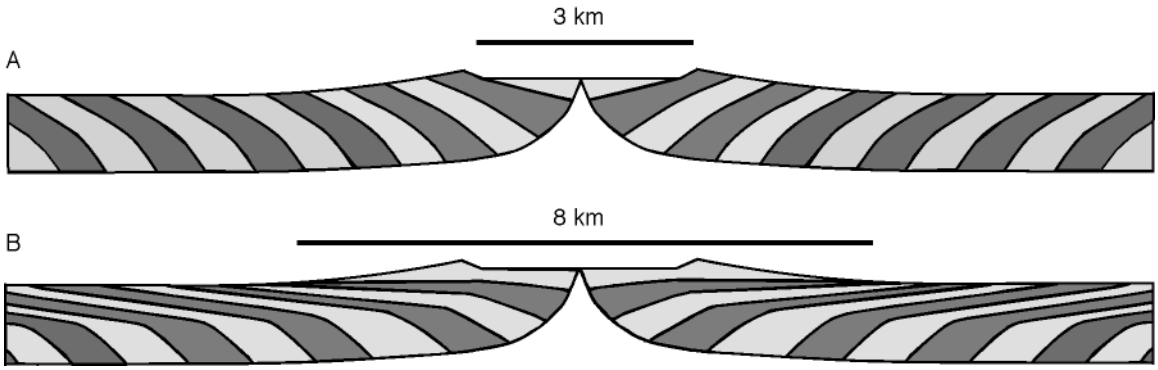

Figure 1.9: Schematic cross-sections of the extrusive section accreting at a mid-ocean ridge. Alternating dark gray and light gray bands indicate constructional packets of lavas, separated by isochrons (solid black lines). (A) Crustal modeling assuming volcanic construction occurs entirely within a 3 km-wide neovolcanic zone. Axial lavas subside to form the base of the extrusive section, rotating toward the axis. Lavas emplaced near the farther from the axis near the axial valley wall still experience subsidence, but are rotated to a lesser degree. The resultant isochron follows a curvilinear path that dips toward the spreading center, representing the half-width of the neovolcanic zone. (B) Crustal modeling assuming volcanic construction occurs within an 8 km-wide zone, up to 4 km from the axis. The eruption of lavas over large horizontal distances creates longer isochrons extending farther off-axis. As in (A), lavas erupted on- or near-axis subside to form the base of the lava pile, steeply rotating toward the spreading center. Lavas emplaced on the surface farther from the axis, as a result of either extensive flow from the axis or eruption off-axis, experience little subsidence, resulting in shallowly dipping isochrons in the upper lavas.

evidence support a fundamental distinction between the upper and lower lava units, and suggests that off-axis volcanism (in the form of off-axis eruptions and/or extensive flows emanating from the axis) plays an important role in the accretion of the upper crust on the Cleft Segment.

In this context, the observed difference in compositional between the upper and lower lavas along the BT scarp may provide insights into axial and off-axis magmatic construction along the Cleft Segment. In general, the data show a preponderance of relatively primitive compositions among the upper lavas, while the lower lavas tend to be more evolved. This offers further support for the idea that the upper lavas were emplaced by off-axis flows or eruptions that capped the lower lavas accreted on-axis. It should be noted, however, that the compositional difference observed (primitive lavas on top) is opposite to that predicted by Stakes et al. (2005), in which the upper lavas represent off-axis flows that tap the evolved edges of the magma chamber. Alternatively, the compositional distinction may be related to a robust phase of magmatism, during which primitive, voluminous lavas flow off-axis. Once again, our ability to observe robust spatial patterns in the BT lavas may be complicated by our sparse sample coverage and an incomplete understanding of age relations among the lavas. The difficulties we encounter in interpreting temporal evolution and spatial distribution in the BT lavas demonstrate the need for further studies of *in situ* ocean crust with depth to develop sampling strategies that address variations across both small and large spatial scales.

1.6.3 Constraints on the timing of upper crustal accretion

Few investigations have addressed the length of time required to build the various units of oceanic crust. One outgrowth of our examination of the geologic and

geophysical evidence for crustal construction is that it can be used to estimate the amount of time it takes to accrete the extrusive section of the crust. The simple calculation that follows is based on the geometry of the dip of the isochrons in the lower lavas, the thickness of the lower section of the extrusive unit, the width of the neovolcanic zone, and the average half-spreading rate. Since the upper lavas may unconformably overlie the lower lavas, and because the isochrons are not well constrained in the upper lavas, we focus our model specifically on the time required to construct the lower lava unit at the spreading axis. The full thickness of the extrusive section is attained some time later, after the addition of off-axis flows.

We used the average dip of lava flows at a given depth in the lower lava unit, which correlates with the dip of the magnetic isochron, to determine the orientation of a model isochron for the BT scarp, shown in Figure 1.10. The width of the current neovolcanic zone (~3 km, Kappel and Ryan, 1986) and the thickness of the lower lava unit (average ~700 m, Karson et al., 2002b) were used to constrain the width and height of the model isochron. Immediately following the phase of axial magmatic construction, this model isochron intersects the bottom of the ~0.7 km thick axial (lower) lava unit and would be expressed at the surface over a horizontal distance of 1.5 km, providing that off-axis lavas have not yet been emplaced. Assuming an average half-spreading-rate of 30 mm/yr, simple spreading calculations imply that a horizontal distance of 1.5 km represents 50 ka. Following the path of the model isochron, a lava flow located at the bottom of the lava pile will be 50 ka older than a lava flow located vertically above it at the surface. Thus, a vertical section through this extrusive unit represents ~50 ka of accretion, and the thickness of the lava unit accreted at the axis is achieved in this amount of time. The full thickness of the extrusive oceanic crust is achieved sometime later, as a capping veneer of lava is added by off-axis flows and eruptions.

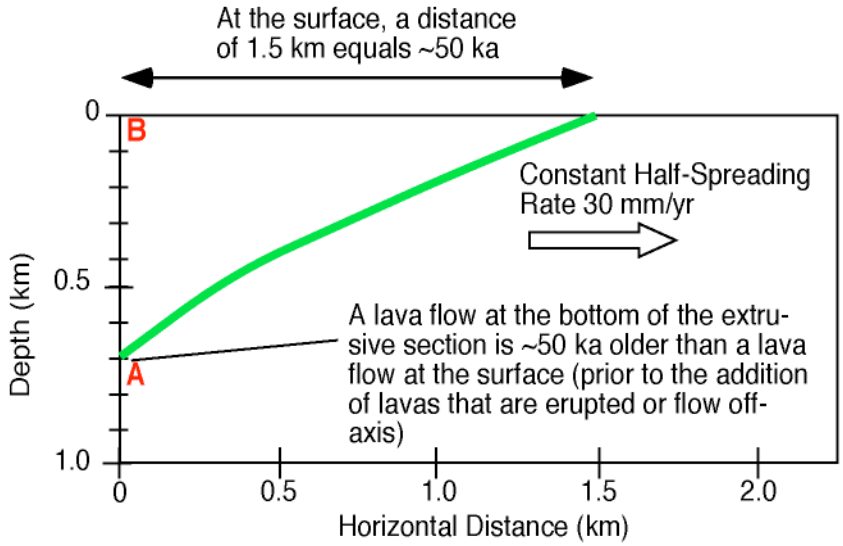

Figure 1.10: Model isochron (green) for the BT lower lava section based on the thickness of the lower lava unit, the width of the neovolcanic zone, and the dips of lava flows and magnetic isochrons. Prior to the addition of off-axis (upper) lavas, an isochron that intersects the bottom of the lava section (~0.7 km depth) will intersect the surface at a horizontal distance of 1.5 km from the axis (the half-width of the neovolcanic zone; Kappel and Ryan, 1986). At a constant half-spreading rate of 30 km/my, 1.5 km represents ~50 ka. This means that a basalt at the bottom of the extrusive unit along the same isochron (A) is ~50 ka older than a basalt at the surface (B). The full thickness of the extrusive section is achieved after the capping veneer of upper lavas is erupted or emplaced off-axis later.

Independent estimates of the length of time required to accrete the extrusive unit are few and, at present, conflicting. One approach, used in a number of seismic studies, is based on the assumption that seismic Layer 2A represents the contact between the extrusive section and the sheeted dike complex; the time it takes to build the extrusive section to its full thickness is then estimated based on the distance off-axis over which Layer 2A thickens (Christeson et al., 1994; Kent et al., 1994; Vera and Diebold, 1994). Studies conducted along the super-fast spreading southern EPR (~75 mm/yr half rate) suggest that the extrusive section achieves full thickness (500-600 m) by ~2 km off-axis, or by ~26 ka (Kent et al., 1994). For the fast-spreading northern EPR (~55 mm/yr half rate), full extrusive thickness (~300 m) is achieved by ~3 km off-axis, or by ~55 ka (Vera and Diebold, 1994). Adjusting for the difference in spreading rate between the northern and southern EPR and the intermediate spreading Cleft Segment (~30 mm/yr half rate), these studies predict that accretion occurs over ~65 ka to ~100 ka on intermediate-spreading ridges. This time period is longer than our estimate based on the isochron model, but may be reasonable when we consider that the full thickness of upper oceanic crust is attained at some distance away from the spreading ridge due to off-axis accretion.

It should be noted that the assumption that Layer 2A represents the base of the extrusive section is controversial, and particularly so with respect to the seismic and geologic data for the Cleft Segment. Canales et al. (2005), for example, showed that Layer 2A thickens to only ~600 m at the Cleft Segment within a few kilometers of the axis, while observations within the BT reveal an extrusive section that is almost double that thickness. In addition, a recent seismic survey on the crust adjacent to the BT suggests that Layer 2A is located within the lava unit, above the intrusive-extrusive boundary (G. Christeson, pers. comm.). These complications make it difficult to use the

Cleft Segment seismic data to independently evaluate our estimate for the timing of accretion.

1.7 Conclusions

The tectonic window exposed along the BT scarp provides an invaluable opportunity to explore crustal accretion and evolution. Our study reveals that off-axis magmatic construction likely plays an important role in accreting the upper layer of lavas that cap the axial extrusive sequence, supporting a mechanism of crustal thickening based on geological and geophysical investigations. The wide range in lava compositions exposed along the BT scarp also suggests that sampling surface lavas along flow lines may not truly represent changing sub-axial magmatic conditions over time. It is apparent, however, that compelling questions about crustal accretion still remain and will require more detailed sampling and analysis of exposures at the BT and other tectonic windows. Do tectonic windows permit accurate estimates of the time required to build the full thickness of extrusive oceanic crust and how does the timing and architecture of accretion vary with spreading rate? What can be learned about the evolution of axial magmatic processes from samples collected at various depths in the crust both along and perpendicular to isochrons? Clearly there is a need for more detailed sampling within tectonic windows to explore both small- and large-scale variability. This, combined with both radiometric age dating of lavas collected at various depths, and geological and geophysical data should ultimately lead to a comprehensive understanding of the processes of crustal accretion and evolution at mid-ocean ridges.

2. Compositions of Dikes and Lavas from the Pito Deep Rift: Implications for Crustal Accretion at Super-fast Spreading Centers

2.1 Introduction

Much of our understanding of the processes that lead to the accretion of the ocean crust depends on seafloor observations, remote geophysical surveys, drill cores and comparisons to ophiolite complexes. While each of these approaches has provided valuable insights into the processes of crustal accretion, none is without limitation. Direct observations of the seafloor, by submersible, remotely operated vehicle or other photographic or sonar imaging, lack the third-dimension, providing information only on the carapace of lavas. Geophysical investigations, such as seismic or gravity surveys of the neovolcanic zone, can place important constraints on the internal structure of a ridge system, but often yield boundaries that cannot be directly related to crustal geology (e.g. Christeson et al., 2007). Drill cores offer an opportunity to ground truth geophysical investigations as well as sample *in situ* oceanic crust with depth, but are limited by their one-dimensional nature.

Significant contributions to our understanding of crustal accretion have been made recently through studies of "tectonic windows," faulted escarpments that expose extensive sections of the oceanic lithosphere. As a complement to drilling and ophiolites, tectonic windows provide direct access to *in situ* ocean crust without the questions of provenance that plague ophiolite studies. In contrast to seafloor investigations, tectonic windows offer the opportunity to sample the ocean crust with depth at spatial scales that rival terrestrial sampling. Observations from tectonic windows in the northeast Pacific (Blanco Transform) and equatorial Pacific (Hess Deep

Rift) reveal that the architecture and composition of the upper crust at intermediate- to fast-rate spreading centers are more complicated than predicted by current models for crustal accretion (Tivey et al., 1998; Karson et al., 2002a; Karson et al., 2002b; Stewart et al., 2002; Stewart et al., 2002; Stewart et al., 2003; Pollock et al., 2005).

This study presents chemical analyses of dikes and lavas from the Pito Deep Rift, a tectonic window in the southeast Pacific that exposes ocean crust generated at a super-fast spreading center. The steep walls of Pito Deep expose continuous (~5 km wide) and intact sections of ocean crust, from the uppermost extrusives down into the dikes and the underlying gabbroic unit. Prior to this investigation, information on crust formed at super-fast spreading rates was primarily derived from marine studies along the southern East Pacific Rise (13° - 23°S), a region currently spreading at a rate greater than 140 mm/yr (Sempéré et al., 1987; Sinton et al., 1991; Bach et al., 1994; Mahoney et al., 1994; Cormier and Macdonald, 1994; Sinton et al., 2002). Recently, ODP Hole 1256D penetrated over 1500 meters deep into crust formed at super-fast spreading rates up to 200 mm/yr (Expedition 309 and 312 Scientists, 2006). Our work at the Pito Deep complements these studies, providing a unique perspective on super-fast spread crust that is unattainable by other approaches. An examination of the compositions of dikes and lavas from Pito Deep reveals systematic patterns that lead to a better understand of the processes of crustal accretion at super-fast rate spreading centers.

2.2 Geologic Setting and Investigation of the Pito Deep Rift

The Pito Deep Rift, located at the northeast corner of the Easter Microplate in the southeast Pacific Ocean (23ºS, 112ºW; Figure 2.1) is characterized by a wide zone of deformation produced by the northwesterly propagation of the East Rift of the

microplate into old Nazca plate lithosphere (Francheteau et al., 1988; Martinez et al., 1991; Naar and Hey, 1991; Naar et al., 1991; Hekinian et al., 1996). Extension ahead of the propagating rift tip causes faulting of preexisting crust, creating a deep region within the rift valley known as the Pito Deep (PD), with >4000 m of relief along its walls and a maximum depth to the valley floor of ~6000 m below sea level. The southwest-facing scarps, which bound the northern side of the PD and delineate the southern edge of the Nazca plate, cut across the local abyssal hill fabric, forming a natural cross-section of Nazca plate crust.

Previous geophysical studies of the PD region include bathymetric (SeaBeam), side-scan sonar (SeaMarc II and GLORIA), magnetic, and gravity surveys (Francheteau et al., 1988; Searle et al., 1989; Martinez et al., 1991; Naar and Hey, 1991). These data show that the north wall of the PD consists of northwest-southeast-trending, structurally unified blocks of crust that extend for tens of km along-strike and <20 km across-strike (Francheteau et al., 1988; Naar and Hey, 1991; Naar et al., 1991; Martinez et al., 1991). The southwest-faces of these blocks form the northern confining walls of the PD, which are steep (>20°) with good exposures of outcrop. The east-facing slopes are shallower and sedimented, with abyssal hill fabric similar to the Nazca plate (Francheteau et al., 1988; Martinez et al., 1991; Naar et al., 1991). Plate reconstructions based on abyssal hill lineament patterns and magnetic anomalies suggest that the northwest-southeast-trending walls of the PD are down-dropped and back-tilted blocks of Nazca plate crust that were faulted <1 m.y. ago by the slow (~10 mm/yr), northwesterly propagation (~10 mm/yr) of the East Rift (Francheteau et al., 1988; Naar and Hey, 1991; Naar et al., 1991). Side-scan sonar and magnetic data show that the local northeast-southwest abyssal hill fabric has been rotated about a vertical axis in the clockwise direction, but otherwise has been little disturbed by the opening of the PD

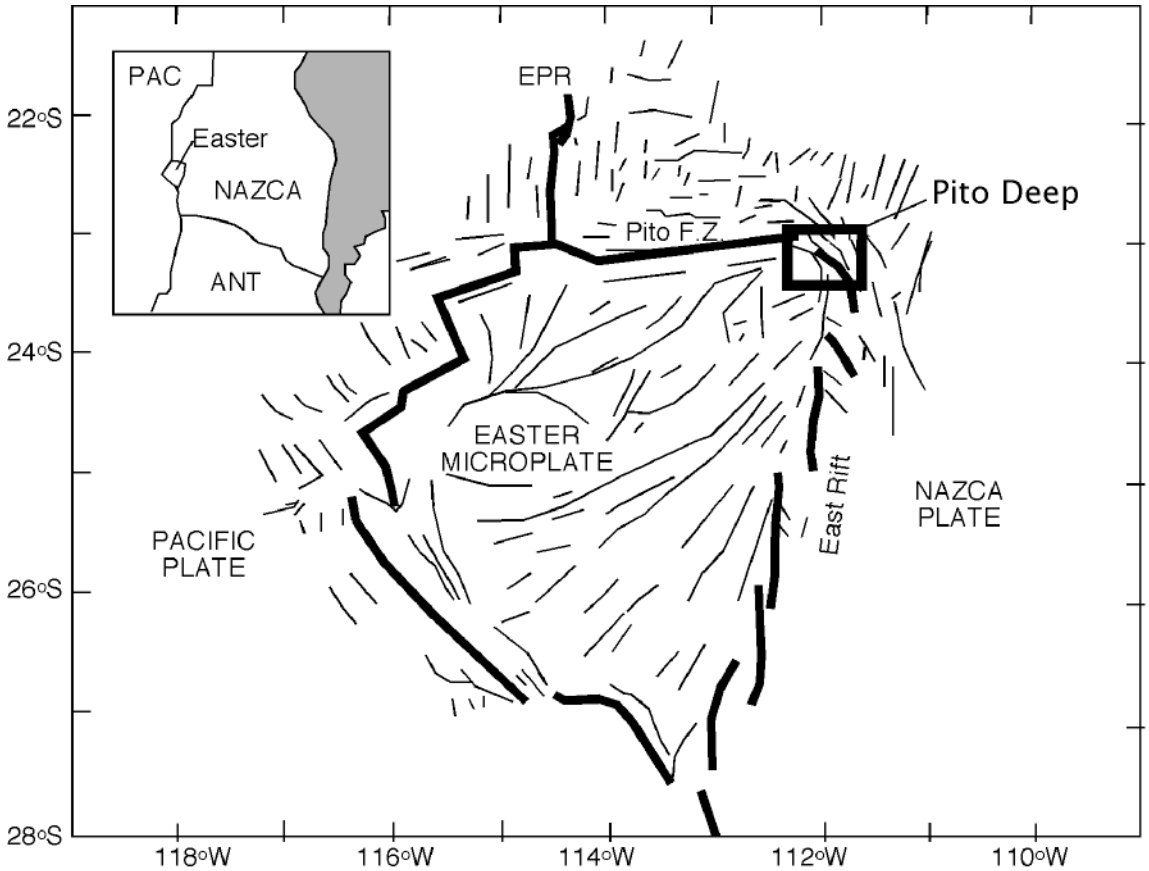

Figure 2.1: Structural interpretation of the Easter Microplate region (modified after Naar and Hey, 1991). The Pito Deep Rift, located on the northeast corner of the Easter microplate, cuts across Nazca Plate crust originally created near 23°S on the East Pacific Rise (EPR). Box encompasses study areas A and B.

(Francheteau et al., 1988; Hey et al, 1985; Naar et al., 1991; Cogne et al., 1995, etc.). Magnetic anomaly 2A, which can be extrapolated across the Pito Rift from the Nazca plate to the north, suggests that the exposed Nazca crust was generated ~3 m.y. ago at the "superfast" spreading East Pacific Rise (EPR; >140 mm/yr full rate; Handschumacher et al., 1981; Martinez et al., 1991, Naar and Hey, 1991; Hey et al., 1995). Thus, while the current configuration of the Pito Rift is a product of extension ahead of a slowly propagating spreading center, the northern walls of PD expose a natural cross-section of ~3 Ma old oceanic lithosphere that was accreted along the EPR, providing a rare "tectonic window" into superfast-spread oceanic crust.

Three reconnaissance dives were conducted along two major escarpments on the northern wall of the PD in 1993 using the manned submersible *Nautile* (Figure 2.2; Francheteau et al., 1994). Observations from these dives describe discontinuous exposures of lithologies similar to those identified in ophiolite complexes, which can be assembled into a nearly complete section of oceanic crust (Moores and Vine, 1971). A northeast transect upslope on a scarp known as the "Jalapeno Ridge" (*Nautile 09*) reveals an upper basaltic volcanic unit exposed in the top ~350 m of the wall, consisting primarily of variably fractured pillow lavas. The volcanic unit is sparsely intruded by dolerite dikes and quickly transitions downward into a sheeted dike complex that is ~500 m thick before the bottom contact is obscured by talus. The dikes are locally sinuous, with orientations ranging from near-vertical to moderately steeply dipping to the southeast, and are separated in some places by screens of brecciated material. Hydrothermal stockwork is observed over a thickness of ~40 m within the sheeted dike unit (Francheteau et al., 1994). Observations during two deeper dives southeast of Jalapeno Ridge (*Nautile 06 and 03*) found similar exposures of basaltic lavas and sheeted

Figure 2.2: (Next Page) *Nautile* (1993), *Jason II* (2005), and *Alvin* (2005) dive tracks in study areas A (top) and B (bottom) showing observed lithologic units (Pito Deep Scientific Party, 2005; Morgan et al., 2005). *In situ* dikes (closed circles) and lavas (open circles) analyzed in this study are colored-coded by Mg#.

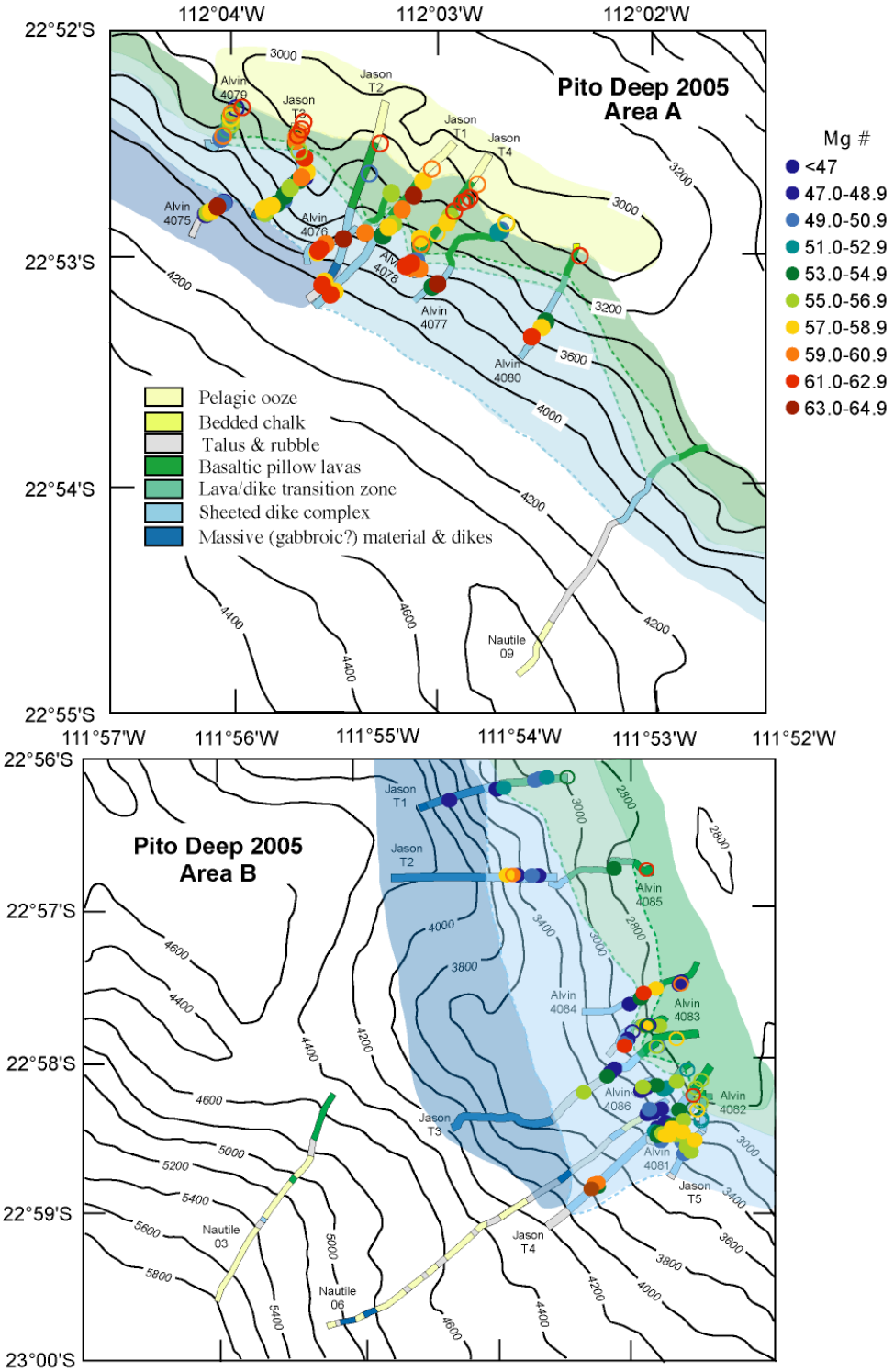
Pito Deep 2005
Area A
Mg #
<47
47.0-48.9
49.0-50.9
51.0-52.9
53.0-54.9
55.0-56.9
57.0-58.9
59.0-60.9
61.0-62.9
63.0-64.9
Pelagic ooze
Bedded chalk
Talus & rubble
Basaltic pillow lavas
Lava/dike transition zone
Sheeted dike complex
Massive (gabbroic?) material & dikes
Pito Deep 2005
Area B

dikes. The volcanic unit outcrops irregularly over ~400 m and contains a greater fraction of sheet and lobate lavas compared to the Jalapeno Ridge. A somewhat fractured sheeted dike complex, which is similar in thickness and appearance to the unit exposed on the Jalapeno Ridge, overlies outcrops consisting of both dolerite dikes and gabbro. Olivine gabbro was recovered from the deepest depths along the scarp (~5000 to 3800 m) and occurs in intermittent outcrops over ~250 m (Francheteau et al., 1994; Hekinian et al., 1996; Constantin et al., 1996).

We revisited the northern PD escarpments in 2005 during a nested-scale study that used the DSL-120 side-scan sonar, the *Jason II* ROV, and the *Alvin* manned submersible for low- to high-resolution mapping and sampling. The investigation focused on areas previously examined by the 1993 *Nautile* dive program, which revealed excellent exposures of shallow-level crust along the Jalapeno Ridge, herein referred to as Area A, and deeper-level crustal units to the southeast, known as Area B. The study areas are each ~5 km wide and are separated by ~14 km. Assuming a constant half-spreading rate of 72 mm/yr, each study area represents ~58 kyr of spreading. Long transects by *Jason II* (9) and shorter transects by *Alvin* (12) covered depths from ~4000 m to ~2500 m upslope across both study areas. Dive spacing was commonly less than a km, although some dive tracks intersected one another (Figure 2.2), allowing samples to be collected over small (meter) and large (hundreds of meters) spatial scales.

Detailed observations from the multiple 2005 *Jason II* and *Alvin* dives to the northern PD scarp reveal in greater detail the architecture of the ocean crust (Figure 2.3). Lithologies observed in the PD were anticipated from the few 1993 *Nautile* dives: an upper unit of basaltic lavas, an underlying sheeted dike complex, and a lower unit of gabbroic rocks (Figure 2.3). The volcanic unit of the crust is dominated by pillow lavas with only sparse occurrences of sheet flows and lobate lavas, and varies in thickness from ~100-500 m. The

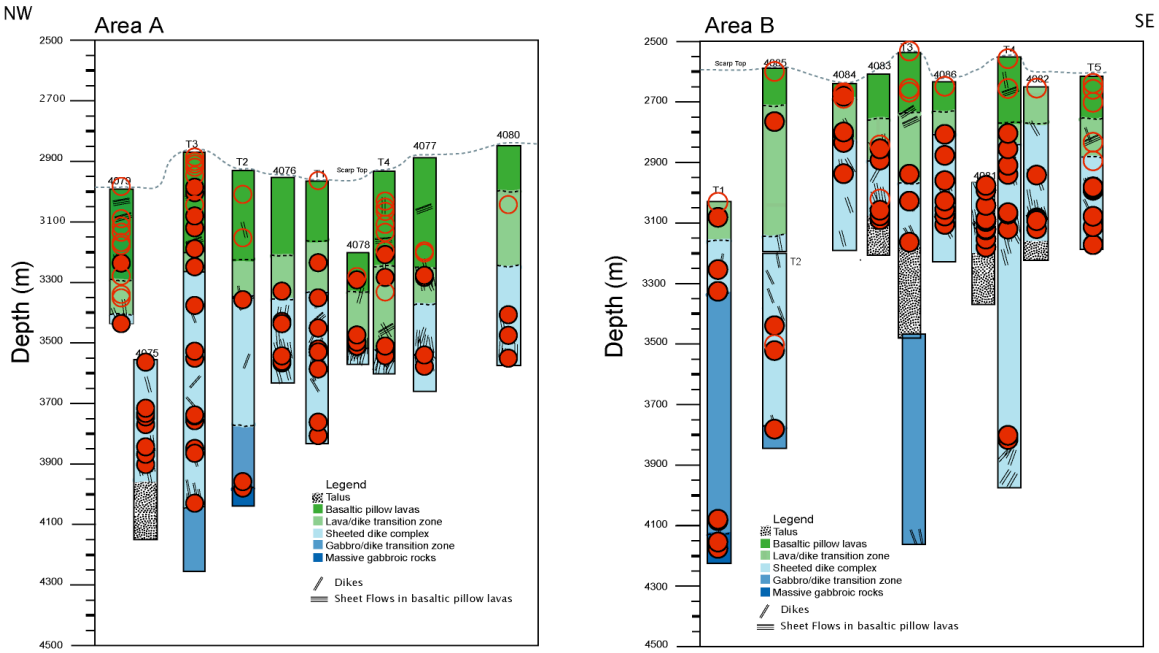

Figure 2.3: Lithologic columns for study areas A and B (Morgan et al., 2005) showing locations of *in situ* dikes (closed circles) and lavas (open circles) analyzed in this study. Lithologic units are based on observations from each dive transect.

underlying sheeted dike complex consists of dikes that are nearly vertical to steeply dipping (65°-80°) to the southeast, and ranges in thickness from 700 m to 1000 m. Outcrops of massive gabbroic rocks are exposed at the deepest depths (>4000 m), where the maximum thickness of the unit is ~700 m before its bottom contact is obscured by talus. Contacts between these units are transitional; dikes intrude lavas near the top of the sheeted dike complex and intrude gabbros near its base. On average, the transition zones are ~200 m thick. Overall, deformation is low and mostly confined to local areas of brecciation, fault gouge, and hydrothermal veining.

2.3 Sampling and Sample Description

Our 2005 *Alvin* and *Jason II* expedition to the northern wall of the PD recovered an extensive suite of rock samples from two ~5 km-wide study areas (Areas A and B) approximately 14 km apart. More than 400 samples were collected *in situ* from outcrops of basaltic lavas (134), sheeted dikes (219), and massive gabbros (26), as well as fault breccias (32) and hydrothermally altered materials (10). Imaging and observations from the *Alvin* and *Jason* dives provide excellent control on sample locations and field relationships, resulting in the fine-scale sampling of 11 pairs of dikes spaced <1m apart. An additional 28 pairs of dikes and five pairs of lavas were collected within 25 meters of each other. In the context of oceanic studies, the PD sample suite is unmatched in sampling detail and geologic control.

This study focuses on samples recovered from the PD extrusive unit and sheeted dike complex. Samples of gabbro and hydrothermally altered or brecciated material are analyzed and reported elsewhere (Hayman and Karson, 2006; Heft et al., 2005; Perk et al., *in press*). Overall, dikes and lavas are similar in texture and are aphanitic to sparsely phyric. All lavas and most of the dikes have a fine-grained (<1mm) texture,

with only 30% of dikes exhibiting a medium (1-5mm) grained doleritic texture. A few samples of lavas are weakly porphyritic, containing fewer than 3% phenocrysts. In hand sample, visible phenocrysts are dominated by plagioclase laths of up to <1-2 mm in length.

2.3.1 Alteration

Most samples show various degrees of alteration, as indicated by veins of altered minerals (chlorite and clay) and greenish-brown alteration halos that line fractures and sample exteriors. The altered material, easily distinguished from the fresh, gray interiors, was avoided in the sample preparation procedure. Of the nearly 350 samples that were collected from the sheeted dike complex and extrusive section, 205 were found to be suitably fresh for chemical analyses. All of the fresh dikes and lavas have <2.5 wt% loss on ignition (LOI), a measure well-correlated with alteration (Alt, 1993). Limiting the "fresh" analyses to samples with LOI <1.5 wt% reduces the number of suitable samples to 141. Examination of the variability of elements known to be susceptible to transport during low-temperature seawater interaction (e.g., K, Rb, Ba, Sr and Cs; Andrews, 1977; Humphris et al., 1980; Alt, 1993) suggests that these elements may have been variably mobilized without visible signs of alteration; these elements are therefore excluded from further interpretation below.

2.4 Analytical Methods

Major and trace element analyses were performed at Duke University on whole rock powders, which were prepared from the fresh crystalline interiors of dikes and lavas and crushed by hand using an agate mortar and pestle. Major element

concentrations were measured by direct current plasma emission spectrometry (DCP; Fisons SpecterSpan 7) following methods modified after Klein et al. (1991). Si, Al, Ca, Fe, Mg, Na, Mn, and Ti were analyzed in a 1:4750 dilution while K, Ba, and P were analyzed in a 1:250 dilution. Concentrations of low-abundance trace elements (in a 1:10,000 dilution) were measured by inductively coupled plasma mass spectroscopy (ICP-MS; VG PlasmaQuad 3) using a procedure modified after Cheatham et al. (1993). Various standards, a blank, and a solution to monitor machine drift were also analyzed with each batch of samples run by DCP and ICP-MS. The standards used for calibration in both DCP and ICP-MS runs included the following: NBS-688, AII92-29-1 (a Mid-Atlantic Ridge standard), K1919 (a sample from the same lava flow as USGS BHVO-1), and U.S. Geological Survey standards BHVO-1, W2-1, BIR-1, and DNC. Samples solutions were run in duplicate and sometimes triplicate. In addition, multiple solutions were prepared for some samples and analyzed in separate runs. Reported uncertainty was determined by repeat analyses (~30) of standards as unknowns. Reproducibility for DCP analyses is 1-2% for all elements with the exception of <5% for K. For ICP-MS analyses, reproducibility is 1-3% for REE and 1-4% for all other elements except Cs (<5%) and U (<5%).

Lead isotope analyses were performed on 300-500 mg of whole-rock powder. Samples were dissolved in HF and HNO_3, converted to chlorides, then bromides. Isolation of Pb was accomplished using HBr anion exchange chemistry following the method of Parrish (1987). Isotope analyses were performed on a VG-SECTOR 54 mass spectrometer at the University of North Carolina at Chapel Hill in static multicollector mode with ^{208}Pb = 1-2 e^{-11} amps.

2.5 Results

2.5.1 Comparison to Range in EPR Basalt Compositions

Representative major and trace element compositions of dikes and lavas from the PD are presented in Table 2.1. All PD data are presented in Appendix A and compared, in Figure. 2.4, to N-MORB representing the global range in major element compositions. As a whole, PD lavas range from relatively primitive to more evolved (Mg#s = 66 to 42; MgO = 9.2-5.7 wt%). Data from Areas A and B generally overlap with glass and whole-rock compositions of lavas collected from 21°-23° S on the southern EPR, the approximate latitude of the EPR where the PD dikes and lavas were generated, with some clustering toward the upper and lower limits of FeO* and Al_2O_3, respectively. Like the EPR lavas, PD lavas are intermediate in major element composition compared to data from the Kolbeinsey Ridge and the mid-Cayman rise, which respectively represent lavas generated by large and small extents (and pressures) of melting (e.g., Klein and Langmuir, 1987).

2.5.2 Crystallization

Overall, the PD major element data show variations with MgO that are consistent with the effects of crystallization of a tholeiitic magma, specifically, increasing abundances of incompatible elements (e.g., FeO*, TiO_2, REE, and Y) and decreasing abundances of compatible elements (e.g., Al_2O_3, CaO, and Ni) with decreasing MgO concentrations (Figures 2.4 and 2.5). Data from Area A extend to more primitive compositions compared to Area B (Figure 2.4). Most of the more evolved (Mg#<51) samples were recovered from Area B and can be classified as FeTi basalts

Table 2.1: (Next Page) Major and trace element data for representative whole rock samples from Pito Deep. [1]Morphology refers to dike (d), pillow (p), massive (m), sheet flow (s), or talus (t). [2]Lithologic zone refers to dike unit (D), volcanic unit (V), dike-lava transition zone (T), and gabbro-dike transition zone (GDT). [3]Samples that fall into the Low FeO* Group are marked. Major element oxides are reported in weight%; trace elements in ppm. FeO* is total Fe recalculated as FeO. Mg# is calculated as cation mole % [Mg/[Mg+Fe)]. Major elements and Sr, Sc, Zn, and V were analyzed by DCP. Reproducibility for DCP analyses is 1-2% for all major and minor elements with the exception of the following: <5% for K. The remaining trace elements were analyzed by ICP-MS, for which the reproducibility is 1-3% for REE and 1-4% for all other elements except Cs (<5%) and U (<5%). Replicate analyses of standards are in agreement with previously published values (see electronic database of Stewart et al., 2002).

Table 2.1 Major and Trace Element Compositions of Pito Deep Dikes and Lavas

Sample ID	020705-1408	020805-0108	020905-1404	022305-0636	4077-1718	4079-1920	4084-1830	4085-1935	4086-2006
Study Area	A	A	A	B	A	A	B	B	B
Jason Transect	1	1	3	5					
Morphology[1]	d	p	d	p	d	p	d	p	p
Lithologic Zone[2]	D	V	D	T	D	V	T	V	V
Depth (mbsl)	3657	3042	3676	2829	3538	3114	2768	2589	2664
Latitude (ºS)	22.884	22.878	22.882	22.973	22.886	22.873	22.959	22.946	22.967
Longitude (ºW)	112.056	112.051	112.063	111.875	112.051	112.067	111.882	111.882	111.877
SiO_2 (wt%)	51.78	50.60	50.89	50.81	49.19	51.66	52.42	52.07	50.89
TiO_2	1.44	1.53	1.51	1.83	1.16	1.70	1.43	1.42	1.93
Al_2O_3	13.90	14.94	13.86	13.81	15.21	14.31	14.37	14.59	13.53
Fe_2O_3	11.89	10.88	12.92	13.51	10.04	9.69	9.35	9.26	12.03
FeO*	10.70	9.79	11.63	12.15	9.04	8.72	8.42	8.33	10.83
MnO	0.22	0.18	0.20	0.22	0.17	0.20	0.20	0.20	0.21
MgO	7.27	8.21	7.65	7.25	9.16	7.31	7.87	7.52	6.78
CaO	10.46	11.75	10.87	10.48	11.13	11.66	12.38	12.31	10.87
Na_2O	2.75	2.60	3.12	2.86	2.49	2.70	2.57	2.55	2.71
K_2O	0.04	0.23	0.06	0.09	0.06	0.22	0.21	0.22	0.13
Total	99.75	100.92	101.10	100.85	98.62	99.43	100.80	100.15	99.07
Low FeO* Grp[3]						X	X	X	X
Mg#	54.8	59.9	54.0	51.5	64.4	59.9	62.5	61.7	52.8
LOI	0.9	0.5	0.9	0.9	1.8	0.3	0.4	0.5	0.3
Sr (ppm)	78	147	99	95	89	135	126	112	113
Ba	2.59	16.95	128.58	1.66	1.72	21.29	14.27	11.33	10.22
Zn	75	87	47	104	48	91	90	83	110
Cu	74	64	142	67	12	78	67	73	62
Ni	61	117	113	47	98	60	80	93	51
V	250	314	352	382	283	373	318	346	407
Sc	39.3	39.2	43.7	42.6	39.4	44.1	42.3	45.3	43.4
Cr	205	325	283	54	378	204	164	252	90
P	439	1756	2934		1190	1700	1154		1842
Y	29	34	27	41	28	45	36	38	48
Zr	48	114	102	116	58	121	88	84	128
Be	0.34	0.66	1.09	0.50	0.73	0.28	0.44	0.45	0.61
Co	44.1	41.4	43.4	42.6	41.6	46.2	48.3	49.3	43.0
Rb		1.74	10.12		0.15	1.12	0.56	0.36	1.03
Nb	0.60	4.29	19.52	1.32	0.91	2.31	1.39	1.33	2.07
Cs	0.003	0.021	0.096		0.006	0.023	0.013	0.014	0.016
La	1.29	4.51	14.53	2.71	1.93	3.65	2.45	2.42	3.43
Ce	4.99	13.54	37.15	10.05	7.34	12.45	8.42	8.71	11.96
Pr	1.00	2.20	5.38	1.90	1.39	2.24	1.56	1.56	2.23
Nd	6.08	11.19	24.35	10.53	7.69	11.67	8.78	9.04	12.36
Sm	2.68	3.65	6.01	3.93	2.81	4.12	3.21	3.19	4.66
Eu	1.03	1.26	2.02	1.19	1.02	1.42	1.17	1.12	1.52
Gd	4.23	4.76	6.26	5.42	3.84	5.61	4.79	4.08	6.49
Tb	0.78	0.87	0.98	0.85	0.73	1.08	0.87	0.74	1.14
Dy	5.26	5.76	5.29	6.99	4.83	7.30	5.90	5.91	7.98
Ho	1.08	1.23	0.99	1.56	1.03	1.57	1.28	1.29	1.77
Er	2.89	3.42	2.49	3.97	2.76	4.38	3.60	3.16	4.82
Yb	2.74	3.43	1.99	4.05	2.67	4.40	3.58	3.70	4.75
Lu	0.42	0.53	0.29	0.64	0.41	0.71	0.57	0.61	0.76
Hf	1.77	2.90	4.66	2.97	1.34	3.20	2.30	2.48	3.55
Ta	0.06	0.29	1.26	0.12	0.07	0.17	0.11	0.12	0.17
Pb	0.195	0.592	2.150	0.518	0.211	0.718	0.352	0.421	0.855
Th	0.045	0.272	1.196	0.078	0.043	0.142	0.079	0.097	0.114
U	0.019	0.110	0.403	0.034	0.014	0.084	0.150	0.042	1.622
Y/Nb	48	8	1	31	31	20	26	29	23
Nb/Ta	10	15	16	11	13	14	13	11	12
Ce/Yb_N	0.51	1.10	5.18	0.69	0.76	0.79	0.65	0.65	0.70
La/Sm_N	0.31	0.80	1.56	0.44	0.44	0.57	0.49	0.49	0.48

(FeO* >12% and TiO2 >2%; Byerly, 1980).

The MELTS program (version 5.0.0 [Ghiorso and Sack, 1995; Asimow and Ghiorso, 1998]) was used to model liquid lines of descent (LLDs) at 0.5-, 1-, and 3-kbar pressure (Figure 2.4) Trace element LLDs (Figure 2.5) were calculated assuming perfect fractional crystallization using mineral assemblages from the MELTS model and partition coefficients (K_d) from Bedard (1994). The anhydrous composition of a relatively primitive (Mg# 64; MgO 9.2 wt%) PD sample (4077-1718) was used as the parental magma composition. The models produce typical tholeiitic differentiation trends through the successive fractional crystallization of olivine, plagioclase, clinopyroxene, and spinel. Since small amounts of water have been shown to suppress the onset of plagioclase crystallization (e.g. Green and Ringwood, 1968; Sinton and Fryer, 1987; Sisson and Grove, 1993; Danyushevsky, 2001), an LLD was modeled for a parent magma composition (4977-1718) containing 0.3 wt% H_2O. The PD major and trace element data are best described by up to 63% crystallization along calculated anhydrous LLDs up to 1 kbar of pressure. Olivine appears first in the crystallizing assemblage and is quickly joined by plagioclase at 8.7 wt% MgO after only ~5% total crystallization. CaO concentrations initially increase during crystallization but start to decrease with the appearance of clinopyroxene on the liquidus at 8.3 wt% MgO (after 17% crystallization), which then fractionates with olivine and plagioclase until spinel joins the liquidus at 7.4 wt% MgO (38% total crystallization). The evolved FeTi basalts are formed after ~40% crystallization when the fractionating assemblage consists of a minor portion of spinel and approximately equal fractions of clinopyroxene and plagioclase. For both major and trace elements, data from Area B generally follow the LLD while Area A compositions are more widely scattered (Figures 2.4 and 2.5). Some samples are offset from the anhydrous 1-kbar LLD toward lower and higher

Figure 2.4: (Next Page) Major element variations for Pito Deep Samples from Area A (black) and Area B (green) dikes (open squares) and lavas (filled circles). Symbols are larger than analytical error (+/- 1 sigma). Fields show range in N-MORB compositions from 21-23°S on the EPR (gray), Kolbeinsey Ridge (blue), and Mid-Cayman Rise (pink). Data for the fields are from the Ridge Petrological Database of the Ocean Floor (http://www.petdb.org). Liquid lines of descent are calculated using the MELTS program for 0.5-kb (dashed), 1-kb (solid), and 3-kb (dotted) anhydrous fractional crystallization. The blue line represents the LLD calculated from a parent magma with 0.3 wt% H_2O. Primary sample 4077-1718 (MgO 9.4 wt%) is used as a parental melt

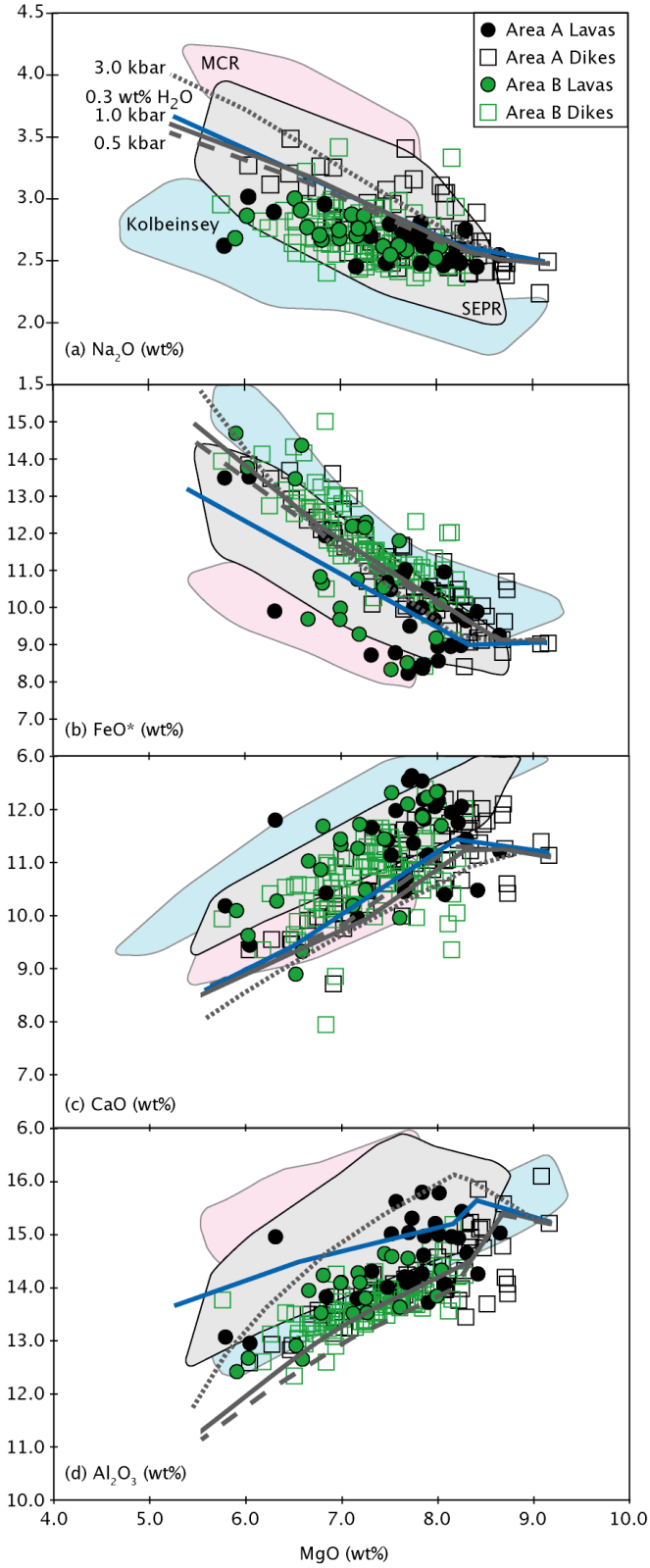
Area A Lavas
Area A Dikes
Area B Lavas
Area B Dikes
3.0 kbar
0.3 wt% H2O
1.0 kbar
0.5 kbar
MCR
Kolbeinsey
SEPR
(a) Na2O (wt%)
(b) FeO* (wt%)
(c) CaO (wt%)
(d) Al2O3 (wt%)
MgO (wt%)

Figure 2.5: (Next Page) Variations in (a) Nb, (b) La, (c) Ce, (d) Zr (ppm) with MgO (wt%) for Area A (black) and B (green) dikes (open squares) and lavas (filled circles). 1-kbar LLD (gray line) calculated assuming fractional crystallization using partition coefficients from Bedard (1994).

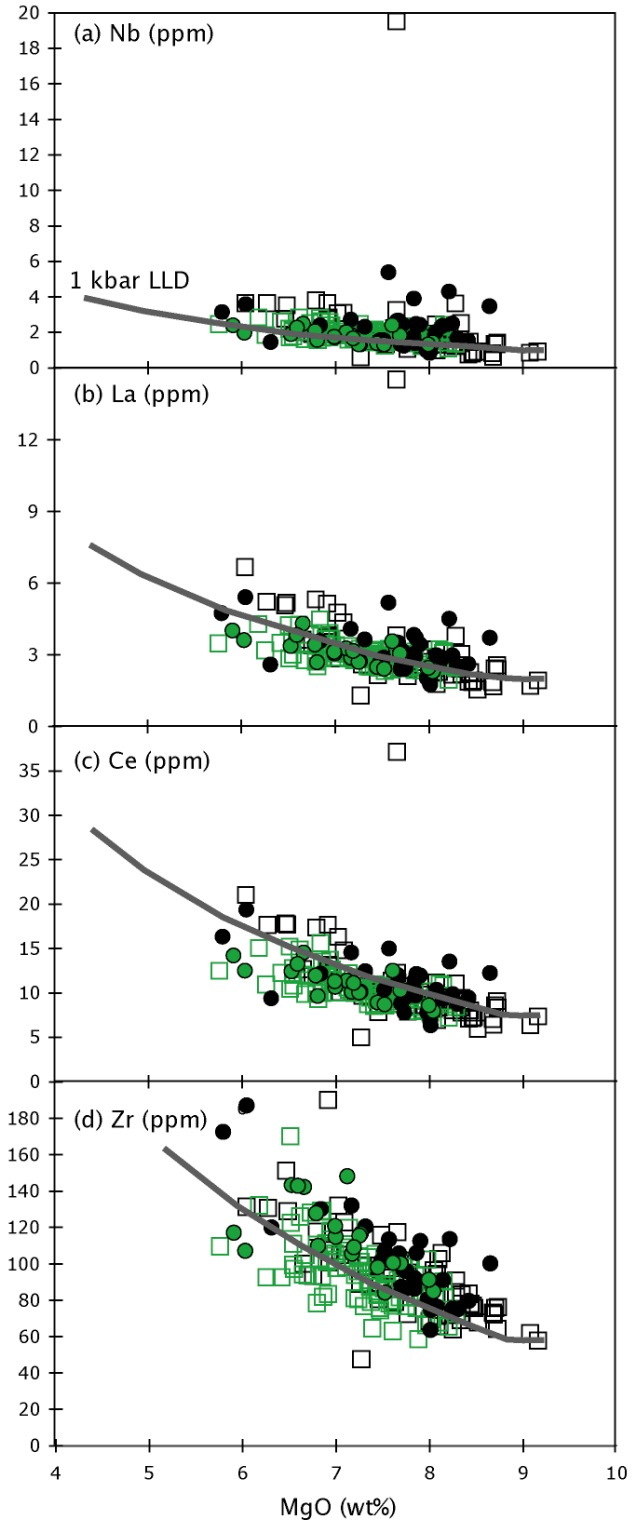
(a) Nb (ppm)
1 kbar LLD
(b) La (ppm)
(c) Ce (ppm)
(d) Zr (ppm)
MgO (wt%)

abundances of FeO* and CaO, respectively, which is consistent with the effects of later crystallization of plagioclase, but cannot be described by adding a reasonable amount of water to the parent magma.

Trends observed in chondrite-normalized REE data (Sun and McDonough, 1989) are also consistent with the effects of fractional crystallization (Figure 2.6). Evolved samples, with lower Mg#s, generally show higher REE abundances and more negative Eu anomalies compared to less evolved, higher Mg# samples. Thus, to first-order, low-pressure fractional crystallization accounts for much of the variation observed in the major and trace element data. There is diversity among the PD samples, however, that cannot be accounted for by crystallization, such as variations at constant values of MgO. Dispersion in the data, particularly within incompatible trace elements and their ratios, suggest that processes related to source composition, mantle melting, and/or mixing conditions may affect the PD suite.

2.5.3 Mantle Melting and Source Characteristics

Based on chondrite normalized trace element and REE patterns, most of the PD samples can be classified as normal MORB (N-MORB) (Figure 2.6; Sun and McDonough, 1989). The majority of samples are depleted in highly incompatible elements (La/Sm_N of 0.50 +/- 0.05) with ratios of moderately incompatible elements near unity (Sm/Yb_N of 1.13 +/- 0.09). Exceptions are six samples from Area A: one enriched MORB (E-MORB, 020905-1404, La/Sm_N of 1.56 four transitional MORB (T-MORB, La/Sm_N of 0.83 +/- 0.04); and one highly depleted MORB (D-MORB, 020705-1408, La/Sm_N of 0.31).

Ratios of strongly and moderately incompatible trace elements (e.g., La/Sm_N,

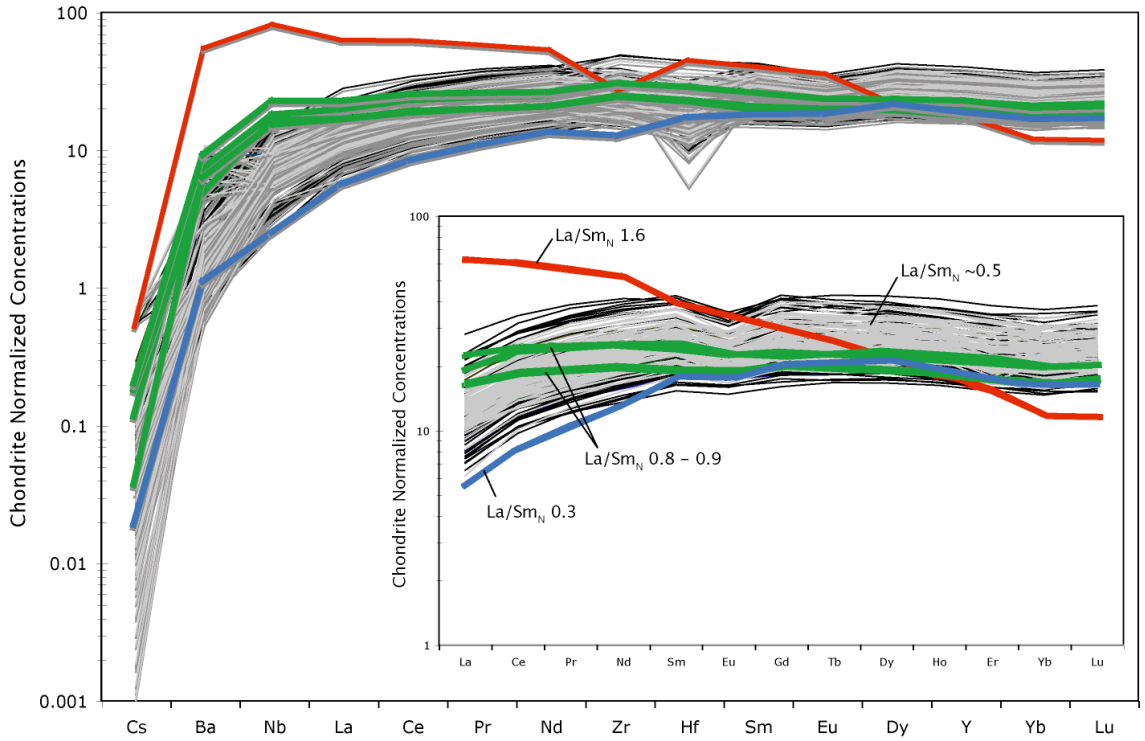

Figure 2.6: Chondrite-normalized trace elements abundances (Sun and McDonough, 1989) in order of increasing compatibility. Inset shows chondrite-normalized rare earth elements (REE). Most of the PD sample are incompatible-element depleted N-MORB (Area A shown in black; Area B in gray; La/Sm$_N$ ~0.5). Four samples can be classified as T-MORB (green; La/Sm$_N$ 0.8-0.9), one as E-MORB (red; La/Sm$_N$ 1.6), and one as D-MORB (blue; La/Sm$_N$ 0.3). All enriched, transitional, and depleted samples are from Area A.

Figure 2.7: (Next Page) Variations in trace element ratios (a) Ce/Yb_N, (b) Y/Nb, and (c) Nb/Ta vs. La/Sm_N for dikes (open squares) and lavas (filled circles) from areas A (black) and B (green). Ratios of Ce/Yb and La/Sm are normalized to chrondrite values (Sun and McDonough, 1989). Extent of variability caused by fractional crystallization (up to 65%) shown in red. Black line indicates up to 30% batch melting of depleted peridotite, marked at 5, 10, and 15% melt intervals. Mixing between enriched (020905-1404) and depleted (020705-1408) MORB composition shown in blue, marked at 10% mixing intervals.

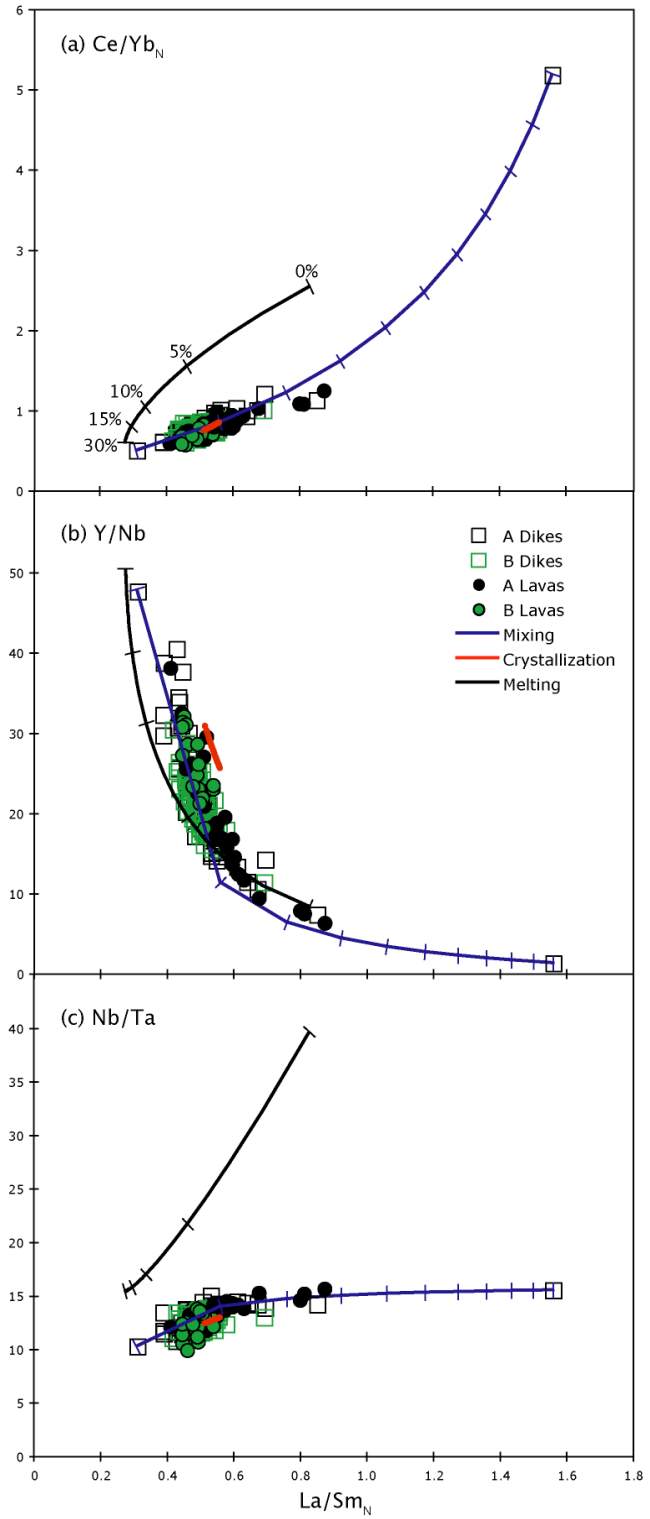
(a) Ce/Yb$_N$
0%
5%
10%
15%
30%
(b) Y/Nb
A Dikes
B Dikes
A Lavas
B Lavas
Mixing
Crystallization
Melting
(c) Nb/Ta
La/Sm$_N$

Ce/Yb_N, Nb/Ta), which remain relatively constant over a reasonable extent of crystallization (<70%, [Gast, 1968]), can be used to distinguish variations in the composition of the mantle source or melting conditions. The variability in La/Sm_N and other incompatible trace element ratios is displayed in Figure 2.7. The PD suite encompasses an expansive field that extends beyond the range of ratios that can be generated through fractionation. Overall, trace element ratios from Area B are relatively constant (e.g., La/Sm_N 0.42-0.69) with MgO, but Area A shows a considerably wider range of compositions (e.g., La/Sm_N 0.31-1.56; Figure 2.7). Such diversity in the PD trace element compositions suggests that either variations in melting a homogeneous mantle generated melts with a wide range of trace element ratios or that the PD magmas were produced by mixing of melts from a heterogeneous mantle source.

To distinguish between the effects of mixing and melting, ratios of strongly and moderately incompatible elements (Figure 2.7) were used to calculate curves for magma mixing and variable extents of melting of a homogenous mantle. Trace element compositions from the E-MORB (020905-1404) and D-MORB (020705-1408) were used to represent the enriched and depleted components of the mixing curve while MORB mantle was represented by depleted peridotite (Sun and McDonough, 1989; Stolper and Newman, 1994; Stewart et al., 2002; Workman and Hart, 2005).

Overall, the PD data form curved trends that are best approximated by mixing between the enriched and depleted samples (Figure 2.7). For some ratios, the mantle melting trend overlaps a portion of the mixing curve, an effect of the initial mantle composition and relative incompatibilities of the elements (e.g., La/Sm_N vs. Nb/Ti). While the effects of melting and mixing may be indistinguishable for these ratios, melting of a homogeneous mantle is an unlikely explanation for the PD data, particularly the

highly variable data from Area A, because an unreasonable extent of melting (over 30%; Klein and Langmuir, 1987) is required to generate the range in trace element ratios between the T- and D-MORB and no extent of melting is sufficient to generate the E-MORB. Area B samples, which show more limited variability in trace element ratios, could possibly be generated through various degrees of mantle melting if the mantle source is more depleted in the highly incompatible elements (e.g., Nb, La, Ce) than the depleted MORB mantle (DMM) used in this study (Sun and McDonough, 1989; Stolper and Newman, 1994; Stewart et al., 2002; Workman and Hart, 2005). Compositional variations in gabbros recovered from the deeper sections of Area B, however, suggest the presence of an LREE enriched magma (Perk et al., *in press*). Thus, the lack of E-MORB sampled from dikes and lavas in Area B does not preclude magma mixing as a realistic explanation for the PD data set.

2.5.4 Pb Isotopes: A 3-Component SEPR Mantle

Figure 2.8 and Table 2.2 present lead isotope compositions for PD samples that were previously determined by REE patterns to be depleted (D-MORB; 1 sample), normal (N-MORB; 13 samples), transitional MORB (T-MORB; 4 samples), and enriched MORB (E-MORB, 1 sample). Overall, the variability in PD lead isotope ratios (ranging 18.308 – 18.764 in $^{206}Pb/^{204}Pb$; 15.481-15.777 in $^{207}Pb/^{204}Pb$; and 37.722 – 38.158 in $^{208}Pb/^{204}Pb$) is similar to isotopic compositions of seamount and axial lavas from the SEPR (Figure 2.8; Sinton et al., 1991; Bach et al., 1994; Mahoney et al., 1994; Niu et al., 1996). The correlation between isotopic ratios is nearly perfect for the $^{208}Pb/^{204}Pb$ vs. $^{206}Pb/^{204}Pb$ data while the PD data show more variability in $^{207}Pb/^{204}Pb$ vs. $^{206}Pb/^{204}Pb$ space, weakly correlated with REE patterns. PD T-MORB fall along the linear trend

defined by the SEPR data while E-, D-, and most N-MORB are offset toward lower and higher values of $^{206}Pb/^{204}Pb$ and $^{207}Pb/^{204}Pb$, respectively. The only exceptions to this pattern are three N-MORB, including sample 022205-0333, which is an N-MORB from Area B that is isotopically similar to the T-MORB from Area A.

Linear trends in Sr-Nd-Pb isotope data from the SEPR have been interpreted as mixing lines between an enriched and depleted mantle source (Niu et al., 1996). The PD data generally fall along these linear mixing trends (Figure 2.8), consistent with patterns in PD trace element ratios that suggest mixing of melts from a heterogeneous mantle. In particular, the PD and SEPR $^{208}Pb/^{204}Pb$ vs. $^{206}Pb/^{204}Pb$ data appear to form a bimodal population consisting of less radiogenic samples, characterized by SEPR N-MORB, and an enriched field defined by seamount E-MORB (Figure 2.8). While N-MORB from PD are distributed between both isotopic groups, T-MORB are only found within the enriched field, suggesting that these samples were derived from an enriched mantle similar to the one that generated the seamount E-MORB.

Axial lavas collected along the SEPR south of the overlapping spreading center (OSC at 20.7°S), a significant axial offset associated with a southward-propagating rift (Macdonald et al., 1988), show elevated $^{207}Pb/^{204}Pb$ ratios at a given value of $^{206}Pb/^{204}Pb$ compared to axial lavas collected from more northerly locations (Mahoney et al., 1994). Similarly, N-MORB from PD are offset to more radiogenic values of $^{207}Pb/^{204}Pb$ compared to the EPR field (Figure 2.8). In $^{207}Pb/^{204}Pb$ vs. $^{206}Pb/^{204}Pb$ space, the axial lavas collected along the SEPR south of the OSC appear to form a linear trend with E- and most N-MORB from PD, with the PD E-MORB representing the most enriched $^{207}Pb/^{204}Pb$ composition. The linear relationship suggests mixing of melts from an enriched component, represented by PD E-MORB, and a depleted component similar to

Table 2.2 Lead Isotope Analyses for Selected PD Samples			
Sample ID	$^{206}Pb/^{204}Pb$	$^{207}Pb/^{204}Pb$	$^{208}Pb/^{204}Pb$
020705-1408	18.462	15.552	38.034
020805-0108	18.764	15.543	38.158
020905-1404	18.396	15.577	38.143
021105-0627	18.577	15.505	37.984
021105-0639	18.645	15.529	38.124
021905-0148	18.308	15.524	37.764
022205-0333	18.612	15.549	38.052
022205-0335	18.409	15.545	38.000
022305-0320	18.481	15.547	38.049
022305-0323	18.393	15.538	37.920
4075-1912	18.548	15.525	38.013
4076-1854	18.488	15.546	38.149
4079-1811	18.309	15.481	37.722
4079-1815	18.444	15.560	37.989
4082-1651	18.343	15.484	37.748
4082-1702	18.469	15.554	38.100
4082-2002	18.345	15.507	37.809
4082-2008	18.396	15.553	38.012
4085-1935	18.483	15.554	38.083
$\pm 2\sigma$	± 0.023	± 0.028	± 0.093

Table 2.2: Lead isotope analyses for selected PD samples. Pb data are referenced to the following values for NBS-981: 16.937, 15.491 and 36.721 for $^{206}Pb/^{204}Pb$, $^{207}Pb/^{204}Pb$, and $^{208}Pb/^{204}Pb$, respectively (replicate standard analyses yield a mean mass fractionation correction factor of 0.12 ± 0.06%/amu). Error in Pb analyses is dominated by error in the fractionation correction. Maximum blank values for Pb run during the time of these analyses was 20 pg.

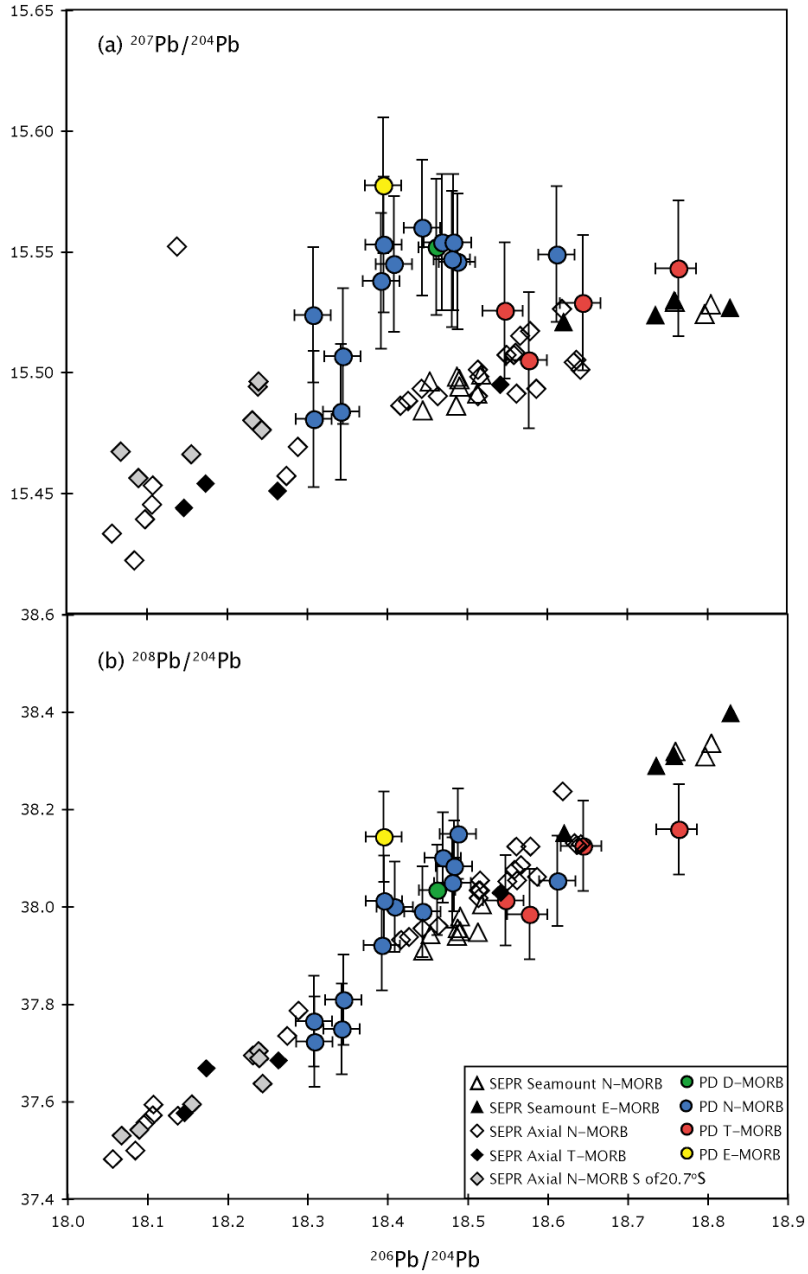

Figure 2.8: Lead isotope compositions for selected PD samples (filled circles), including D-MORB (green), N-MORB (blue), T-MORB (red), and E-MORB (yellow). Data for seamount (triangles) and axial (diamonds) lavas from 13°-23°S the SEPR from Hamelin et al. (1984), Sinton et al. (1991), Mahoney et al. (1994), Bach et al. (1994), and Niu et al. (1996). Black symbols indicate seamount E-MORB and axial T-MORB. Lavas collected between 20.7°-23°S are shaded in gray.

N-MORB from the SEPR. Thus, like the $^{208}Pb/^{204}Pb$ vs. $^{206}Pb/^{204}Pb$ data, the $^{207}Pb/^{204}Pb$ vs. $^{206}Pb/^{204}Pb$ data suggest that the mantle underlying the SEPR, which presumably generated the PD crust, is heterogeneous, however, the nature of the inferred enriched component is somewhat different.

The combined PD and SEPR lead isotope data can be explained by mixing of melts from a heterogeneous 3-component mantle. The bimodal $^{208}Pb/^{204}Pb$ data suggest the presence of at least 2 compositional endmembers: a depleted mantle source, represented by SEPR N-MORB, and an enriched mantle source, represented by seamount E-MORB and PD T-MORB. A third mantle component can be observed in the $^{207}Pb/^{204}Pb$ data, in which the enriched component can be subdivided into a more HIMU-like mantle, with more radiogenic $^{206}Pb/^{204}Pb$ ratio (i.e., PD T-MORB), and a more EMII-like mantle, with a more radiogenic $^{207}Pb/^{204}Pb$ ratio (i.e., PD E-MORB). Mixing of melts between these dual enriched components and the depleted end member produces mixing trends that are consistent with patterns in isotope and incompatible element ratios. While PD T-MORB generally fall along the mixing line between E- and D-MORB in incompatible element space, the Pb isotope data suggest that the T-MORB are derived from a separate, third component of the mantle.

The observation of a 3-component mantle underlying the SEPR is interesting in the context of the development of the OSC at 20.7ºS. The SEPR just north of the OSC is well-known as the Hump Region (Cormier and Macdonald, 1994), characterized by a wide cross-axis area and a broad dome in Sr-Nd-Pb isotope ratios (Sinton et al., 1991; Niu et al., 1996). Lead isotopic compositions from the Hump Region are similar to those displayed by PD T-MORB, suggesting that the PD T-MORB were derived from a mantle source similar to that currently underlying the Hump Region. Mahoney et al. (1994)

reported that the mantle heterogeneity responsible for generating the elevated isotopic patterns in the Hump Region did not extend along the SEPR axis south of the OSC, which was thought to have developed ~3 Ma (Macdonald et al., 1988). They propose a model in which a plume-like heterogeneity is injected into the depleted mantle beneath the Hump Region and is migrating southward (Mahoney et al., 1994). The similarity in isotopic compositions of PD T-MORB and Hump Region samples suggests, however, that this enriched mantle component was already present under the SEPR at the time the OSC is thought to have developed.

Interestingly, the second enriched mantle component is clearly observed within the PD suite as E-MORB and associated N-MORB, but is nearly absent in zero-age lavas from the SEPR data except for the suggestion of $^{207}Pb/^{204}Pb$ ratios that are somewhat elevated above the EPR trend. The presence of the EMII-like isotopic signature in the PD data, and the absence of that signature in the current SEPR data, suggests that this enriched mantle component was depleted over ~3 Ma. The timing of the changes in mantle composition indicated by the PD and SEPR data sets coincides with the development of the OSC, which may relate to the development of axial discontinuities, an interesting and significant topic for future research but beyond the scope of this study. Overall, isotope and incompatible trace element data suggest that the PD crust was generated from a variably enriched mantle.

2.6 Discussion

2.6.1 Spatial Variability

Perhaps the greatest strength of the PD sample suite lies in its range of sampling

resolution; compositional variations can be interpreted at spatial scales ranging from adjacent dikes to 10s of km. The coarsest resolution is observed in geochemical variations between Areas A and B, which are separated by ~14 km (Figure 2.2). Plate reconstructions (Figure 2.1) suggest that the crust exposed in Areas A and B was generated at a single location, or in close proximity, along the EPR at approximately 3 Ma (Naar et al., 1991). Magnetic reversal boundaries at the older extents of the Kaena and Mammoth events intersect Areas A and B (Martinez et al., 1991), respectively, implying an age difference between the study areas of ~180 kyr, consistent with age calculations based on spreading rate. Indeed, major and trace element variations suggest that both crustal exposures were supplied with magma from a similarly heterogeneous mantle, placing these study areas within the same higher-order ridge segment (length scales ≤100 km) based on the segmentation hierarchy of Macdonald et al. (1991). Thus, compositional variability in samples from both study areas does not reflect along-axis variations in crustal accretion, but rather the evolution of magmatism at a single, or proximal, location on the EPR over 100s of kyr.

Overall, the principal compositional difference between the two study areas is that Area A is more primitive (Figure 2.2; average Mg# 57 ± 5) than Area B (average Mg# 53 ± 5). While Area B sampled relatively more dikes (79% of the samples analyzed from Area B are dikes) compared to Area A (69% of Area A samples are dikes), the difference in degree of evolution observed between the two study areas is not the result of biased sampling, as both dikes and lavas from Area A extend to more primitive compositions compared to those from Area B (Figure 2.4). Variations in MgO have been shown to correlate with axial depth, ridge cross-sectional area, and other indicators of variations in magma supply (Sinton and Detrick, 1992; Hooft et al., 1997). Thus, the

distribution of more primitive, lower Mg# samples in the older Area B and more evolved, higher Mg# samples in the younger Area A reflects the evolution of the axial magmatic regime from a lower magma budget to a higher magma budget over ~180 kyr. This is consistent with studies along the SEPR, suggesting that magma supply varies on time scales of ~100 kyr (Hooft et al., 1997; Reynolds et al., 1992).

Spatial variability within each study area (~5 km wide each) represents temporal variations over ~58 kyr of spreading. While each area displays a significant range in Mg# (±5), the distribution of primitive (higher Mg#) and evolved (lower Mg#) samples within each area is arbitrary (Figure 2.2). Evolved compositions are scattered throughout the exposure and bear no apparent systematic relation to samples that are more primitive. In the context of the long-period (~100 kyr) evolution of the axial magmatic regime from a lower to higher magma budget, variation in composition may have been expected to change systematically across the scarps, from lower Mg#s in the relatively older crust (i.e., in the east) to higher Mg#s in the younger crust (i.e., in the west). No such pattern is observed. Thus, the long-term transition in axial magmatic conditions is obscured within the short-term (10s of kyr) period represented by each study area

Yet a finer-scale (~1km) perspective of compositional variability can be observed within individual dive transects, which recovered between 2 and 26 samples per dive. Some transects are relatively homogenous. For example, all samples (9) from *Jason* transect T1 in Area B display Mg#s <53 while closely spaced samples from *Alvin* dives 4081, 4082, 4086 and *Jason* transect T4 are, in general, moderately evolved (Figure 2.2). Similar observations can be made in Area A, where *Jason* transect T4 shows relatively primitive samples. Chemical similarity within the same dive may suggest that superfast-

spread oceanic crust is homogeneous on scales ≤1 km, equating to temporal scales of <2 kyr. Some dive transects, however, display compositions that span the full range of chemical variability shown by the entire dataset. For example, *Alvin* dives 4075 and 4079 from Area A and 4084 from Area B exhibit Mg#s ranging from 43-63 (Figure 2.2). No systematic variation in Mg# was observed within transects apart from 1 dive from Area A (*Jason* transect T3), where deeper dikes are relatively evolved (Mg# ~55) and transition upward into more primitive (Mg# ~62) lavas. While the most distinct change in Mg# occurs where there is an abrupt change in the path of the transect (Figure 2.2), a similar chemical variability with depth has been observed in other crustal exposures along intermediate to fast-spreading centers (Pollock et al., 2005; Stewart et al., 2002). Overall, the observations show that the composition of the upper crust exposed at Pito Deep is highly variable on spatial scales of <1 km, and inferred temporal scales of <2 kyr. In a strictly temporal interpretation, the lack of a predictable lateral or vertical distribution in crustal composition may indicate a rapidly evolving melt reservoir. It is likely that some of the compositional variability reflects along-axis spatial variations that are preserved in the dikes and lavas through along-axis magma transport and eruption.

2.6.2 Adjacent Samples and Implications for Horizontal Magma Transport

To further examine the dynamic nature of the axial magmatic system, observations can be made of adjacent and closely spaced samples. An unprecedented 10 lavas and 42 dikes were collected within 25 m of each other while an additional 19 adjacent dikes (4 from Area A and 15 from Area B) were also recovered. Some closely

spaced samples are chemically similar or only differ in extent of crystallization (e.g., adjacent dikes 4079-1811 and 1815; Figure 2.9). Compositional homogeneity of closely-spaced samples of lavas is not surprising, since individual lava flows along the Southern EPR were shown to be largely invariable compared to the chemical heterogeneity of lava flows on slower spreading ridges (Sinton et al., 2002). This may suggest that some of the closely spaced lava samples were recovered from the same lava flow or were erupted contemporaneously from the same melt reservoir. The same inference may be made, then, for chemically similar dikes. Not only may they have been intruded nearly simultaneously, but adjacent dikes showing compositional homogeneity suggest an origin from the same melt reservoir.

Many of the closely spaced samples, however, are separated by vectors that intersect the crystallization trend (e.g., adjacent dikes 4082-1814 and 1820; Figure 2.9). On plots of major element variations with MgO, tie-lines connecting adjacent dikes that cross the modeled liquid lines of descent suggest that the samples cannot be related by crystallization. Similar discordant relationships can also be observed in incompatible trace element ratios (Figure 2.9), which indicate that spatially proximate samples can show significant differences in source composition. Considering along-axis chemical variability in the melt lens, the wide range in spatial scales for individual lava flows (<1 to > 19 km^2; Sinton et al., 2002), and the periodicity of axial eruptions, it is logical that chemically distinct lava flows may often be emplaced within the same segment (Sinton et al., 2002).

The high degree of compositional variability displayed by PD dikes over short spatial (and inferred temporal) scales is comparable to the extent of variability observed in adjacent dike pairs from Hess Deep (Stewart et al., 2002). Several Hess Deep dike

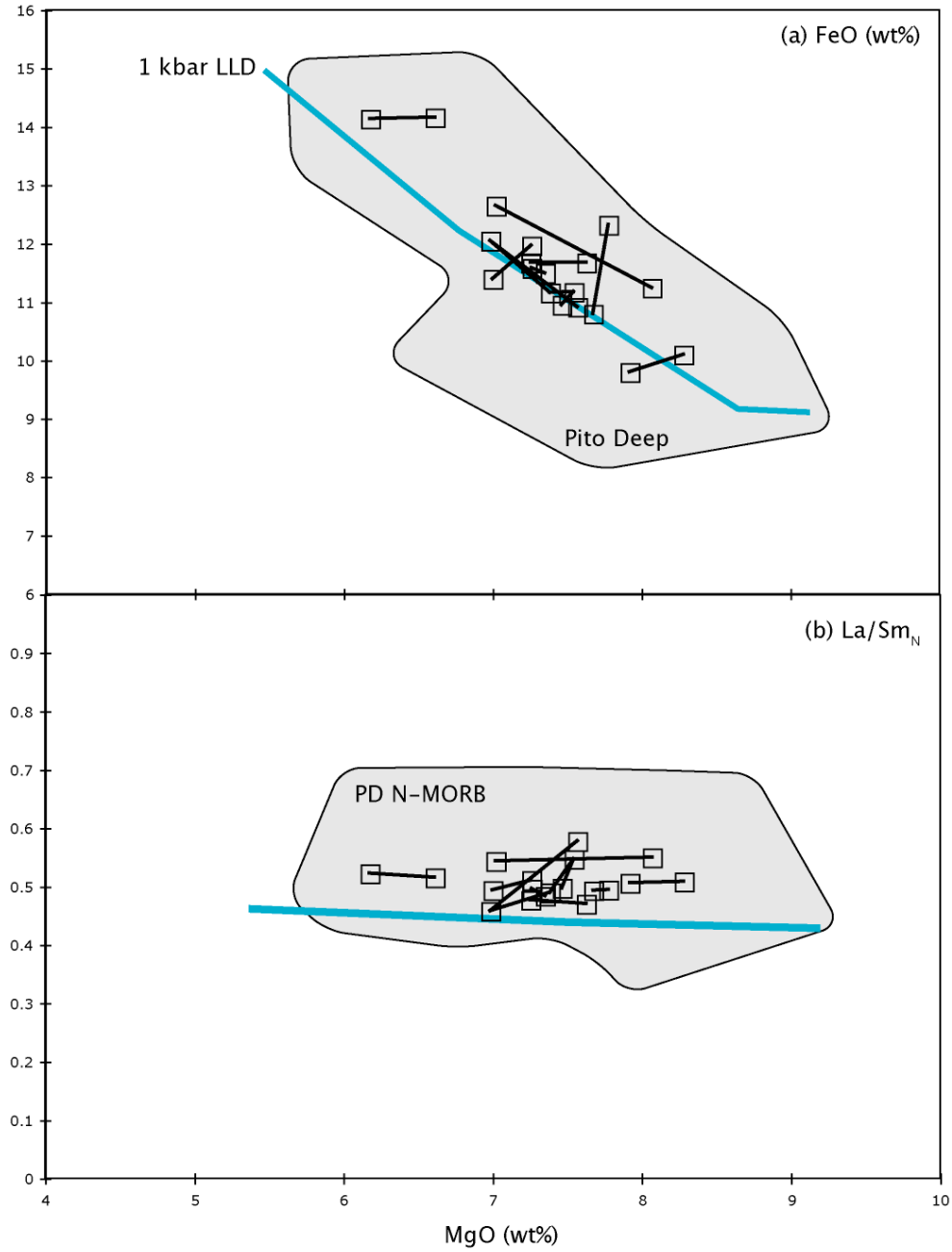

Figure 2.9: Variations in (a) FeO* (wt%) and (b) La/Sm$_N$ vs. MgO (wt%) for adjacent dikes, joined by tie lines. Effects of low-pressure crystallization shown by the 1 kbar LLD (blue line). Gray field indicates the range of all Pito Deep samples in (a) and Pito Deep N-MORB in (b).

pairs show patterns in major and trace elements that indicate different parental sources (Stewart et al., 2002). This observation led to a model for crustal accretion in which magma from chemically distinct melt reservoirs intrudes into dikes and is transported laterally along-axis over short time scales, resulting in the juxtaposition of chemically distinct magmas in adjacent dikes (Figure 2.10; Stewart et al., 2002). This is consistent with multiple studies of magmatic flow textures (e.g., Staudigel et al., 1992; Varga et al., 1998) and seismic activity (Dziak et al., 1995; Embley et al., 2000), which cite evidence for lateral propagation of dikes. The findings at Hess Deep and Pito Deep suggest that horizontal magma transport plays an important role in the construction of the upper oceanic crust at fast- to super-fast spreading centers.

It may be significant to consider whether the role of lateral dike propagation changes depending on location along the ridge segment. This can be examined by comparing dike pairs from Hess and Pito Deeps. Hess Deep is thought to have formed at a segment end where magma supply is restricted, whereas the crust exposed in Pito Deep may have formed at a segment center, based on plate reconstructions (Naar and Hey, 1991). Indeed, the overall primitive nature of the Pito Deep samples implies higher magmatic temperatures and a more robust magma supply compared to Hess Deep. The high degree of variability between adjacent dike pairs from both Hess and Pito Deeps suggests that lateral magma transport in dikes occurs beneath fast- to superfast-spreading centers, regardless of segment location (Figure 2.10). This adds an important three-dimensional perspective to the conceptual model for the formation of the upper crust, in which mantle melts are focused toward the segment center where dikes originate and laterally transport magma along-axis toward the segment ends. Dikes at segment ends occur primarily through lateral intrusion while dikes at segment centers may be

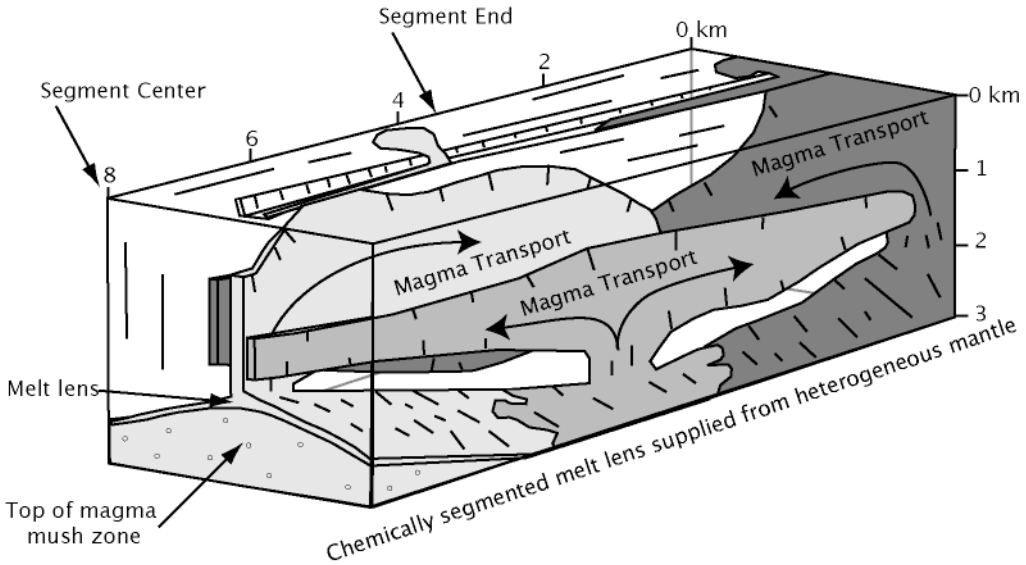

Figure 2.10: Model for lateral propagation of dikes, modified after Stewart et al. (2002). Magma from a chemically segmented melt lens is transported along axis as dikes propagate laterally toward and away from the segment center, resulting in adjacent dikes that are compositionally distinct.

emplaced through lateral and vertical propagation. The implications of this model are that adjacent dikes from segment ends should be relatively more variable in composition compared to adjacent dikes from segment centers, which can be intruded vertically from the same melt lens. While there are adjacent dike pairs from Pito Deep that are chemically similar, the high degree of variability in most of the adjacent and closely spaced dikes suggests that along-axis transport of magma occurs to a significant degree at segment centers as well. These observations imply that the melt lens is physically and/or chemically segmented in the along-axis direction at length scales shorter than or on the order of lengths of dike injection (10s of km; Dziak et al., 1995). Furthermore, the observations imply that dikes intrude horizontally both away from and toward segment centers, which has significant implications for models of dike propagation.

2.7 Conclusions

Chemical analyses of dikes and lavas from the Pito Deep Rift reveal information on the processes of crustal accretion and how they evolve at super-fast rate spreading centers. The longest-term changes (~3 Ma) are observed in comparisons of lead isotopes and trace element ratios between Pito Deep and zero-age lavas from the southern East Pacific Rise, which indicate a variably enriched mantle composition that has evolved over time to become more depleted in one of the enriched components. Over time scales of ~100 ka, the magmatic regime can be observed evolving from a lower to higher magma budget system, as shown by lower average Mg#s in older Area B compared to higher average Mg#s in younger Area A. At time scales <10 ka, the ocean crust is heterogeneous, reflecting along-axis transport of dikes from chemically heterogeneous portions of the melt lens along-strike. This finding contrasts with models for crustal

accretion that suggest that at segment centers, such as the setting thought to characterize the ridge axis where PD formed, dike transport is likely to occur vertically and/or travel laterally away from the segment center. Clearly, observations from tectonic windows provide significant contributions to advancing our understanding of oceanic crustal accretion.

3. Role of Buoyancy in Dike Intrusion and Eruption: Insights from Compositional Variations between Dikes and Lavas

3.1 Introduction

Dike intrusion is a key process in the accretion of oceanic crust during seafloor spreading (Delaney et al., 1998). Individual dikes accommodate increments of spreading by transporting magma through the shallow crust and, when they propagate to the surface, erupting lavas. Thus, the process of dike injection partitions magma between the intrusive dike complex and the overlying extrusive unit, ultimately controlling the architecture of the upper oceanic crust.

Observational data on the structure and composition of the upper ocean crust derives from three main sources: ophiolites complexes, drill cores, and rare crustal exposures on the sea floor. Decades ago, ophiolites provided our best analog for the ocean crust (e.g., Moores and Vine, 1971; Dewey and Bird, 1971), and data derived from ophiolites continue to be of enormous value. Nevertheless, because questions remain regarding the extent to which most ophiolites represent typical sections of ocean crust, extrapolation of information from them to the ocean crust must be approached with caution (e.g., Miyashiro, 1973; Moores, 1982; Karson, 1998; Shervais, 2001). Similarly, much as been learned from drill cores (e.g., Hole 504B; Pariso and Johnson, 1989; Alt et al., 1993), but the perspective a drill core can provide, by its nature, is one-dimensional. Fortunately, in recent years, a small number of areas of the ocean floor have been identified where deeper portions of the ocean crust are exposed *in situ* through so-called "tectonic windows." Some occur along fracture zones (e.g., Blanco Fracture Zone, Vema Fracture Zone), which expose crust generated near the ridge-

transform intersection (Auzende et al., 1993; Juteau et al., 1995; Karson et al., 2002). Potentially more valuable are those where unusual tectonic processes have exposed cross-sections through non-transform-influenced ocean crust, apparently with minimal deformation. The three best explored of these occur along bounding walls of the fast- to superfast-spreading Hess Deep (Lonsdale, 1988; Francheteau et al., 1990; Karson et al., 2002a), Endeavor Deep (Pockalny et al., 2004; Natland and Pockalny, 2006) and Pito Deep Rifts (Francheteau et al., 1994; Constantin et al., 1996; Hekinian et al., 1996; this study).

Although the oceanic crust exposed in these locations is highly variable over short spatial scales (< 1 km), their geology is broadly similar. An upper lava unit, dominated by pillow basalts, grades downward into more fractured lavas, reaching thicknesses up to ~1 km (Karson, 2002). Exposures of the dike units are often obscured by debris slides and talus, but observations reveal sheeted dike complexes largely similar to those described in ophiolite complexes, with swarms of approximately meter-wide dikes that extend vertically for ~1 km or more (Karson et al., 2002b). At Hess Deep and Pito Deep, portions of the underlying gabbro unit are also exposed (Constantin et al., 1996; Hekinian et al., 1996; Coogan et al., 2002).

Chemical analyses of dikes and lavas from the Hess Deep (HD) rift, a tectonic window in the equatorial Pacific that exposes ~1 Ma crust formed at the fast-spreading (~135 mm/yr) East Pacific Rise (EPR; Stewart et al., 2003), reveal an unexpected but significant geochemical characteristic. The majority of HD lavas are offset toward lower abundances of FeO* compared to the dikes, which have compositions that define a typical low-pressure crystallization trend (Figure 3.1; Stewart et al., 2003). In addition

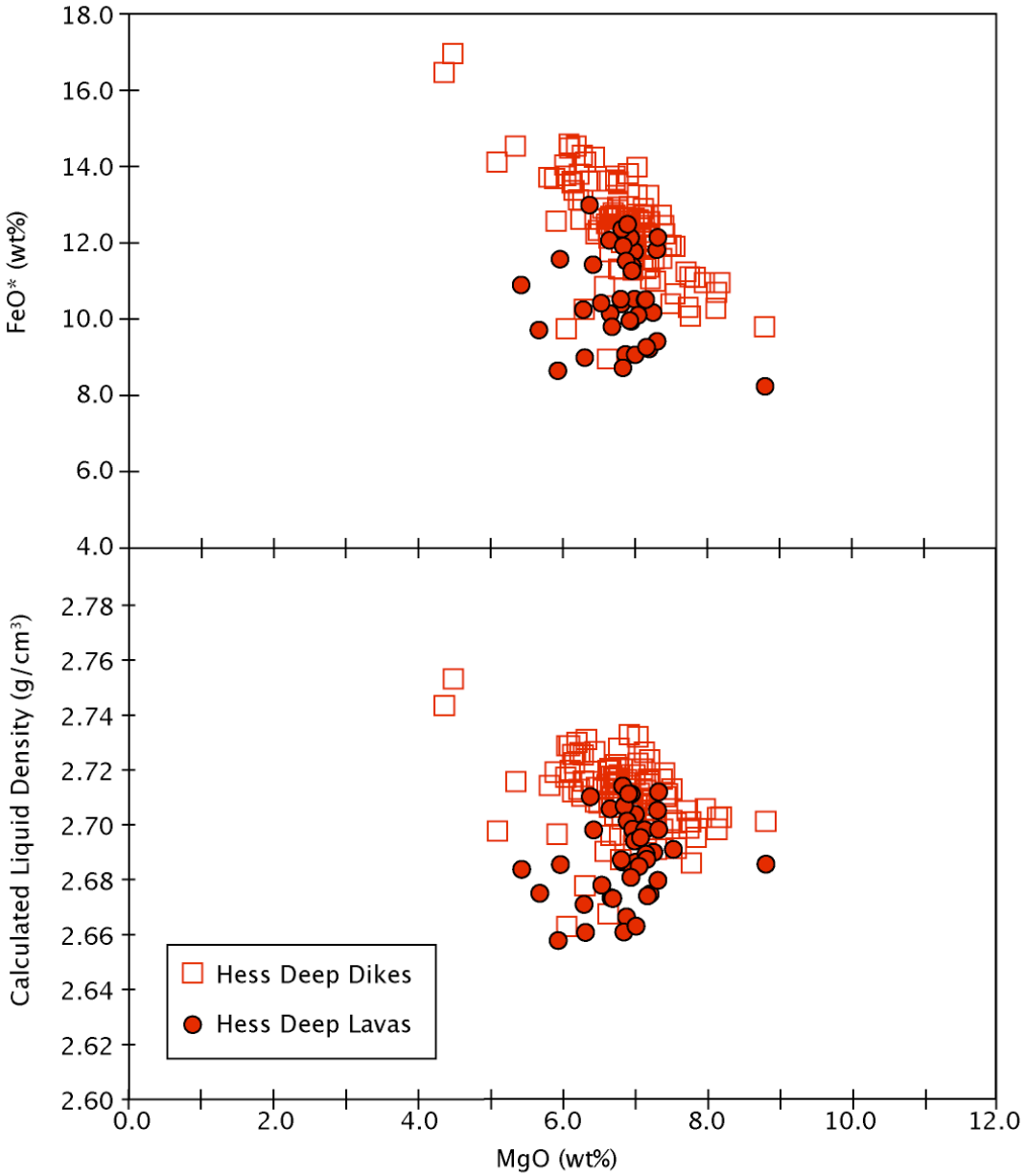

Figure 3.1: Variations in FeO* (top) and calculated liquid density (bottom) with MgO (wt%) for dikes (open squares) and lavas (filled circles) from the northern wall of the Hess Deep Rift (Stewart et al., 2002; Stewart et al., 2003).

to melt temperature and crystallinity, chemical composition determines magma density; thus, the chemical differences between dikes and lavas have important implications for density-filtering of magma during crustal accretion, with bearing on the upper crustal architecture.

Until recently, it was unclear if this chemical distinction was a characteristic unique to HD or a more universal phenomenon. This study presents chemical analyses from the Pito Deep (PD) Rift, a tectonic window in the southeast Pacific that exposes super-fast (>140 mm/yr) crust, which, remarkably, reveal a similar geochemical distinction between dikes and lavas, suggesting that density-filtering plays an important role in the construction of the upper oceanic crust in various settings.

3.2 Chemical Variability of Dikes and Lavas from Pito Deep

The PD Rift is a tectonic window located at the northeast corner of the Easter Microplate (Figure 2.1) that exposes ~3 Ma Nazca plate crust that was generated at the superfast-spreading (>140 mm/yr) southern East Pacific Rise (SEPR; Francheteau et al., 1988; Martinez et al., 1991; Naar and Hey, 1991; Naar et al., 1991; Hekinian et al., 1996). A nested-scale survey was performed on two major scarps along the north wall of the Pito Rift, known as study areas A and B, which are ~5 km wide and separated by ~14 km. The upper crust exposed in each area shows a layered stratigraphy consisting of an upper lava unit (100-500 m thick) dominated by pillow basalts that transitions downward into a sheeted dike complex (700-1000 m thick; Figures 2.2 and 2.3). Over 400 *in situ* samples of lavas, dikes, gabbros, and breccias were collected from both study areas during *Jason II* (12) and *Alvin* (9) transects, which covered ~1500 m of relief and were spaced <1 km apart (Figure 2.2).

Whole-rock geochemical analyses of 206 fresh Pito Deep (PD) dikes and lavas are presented in Chapter 2 (Table 2.1; Appendix A). To first order, much of the compositional variability in major and trace elements can be explained by low-pressure (1 kbar) fractional crystallization. Overall, the crust exposed in Area A, located to the west of Area B (closer to the paleo-spreading center), is more primitive, suggesting that the axial magmatic system may have become more robust over a period of ~180 kyr, a time period estimated on the basis of spreading rate and paleomagnetic data (Naar et al., 1991, Martinez et al., 1991). Patterns in incompatible trace element ratios and Pb isotopes suggest that the PD dikes and lavas were generated from a heterogeneous mantle.

Figure 3.2 displays major element variations in the Pito Rift dikes and lavas. Both dikes and lavas span the entire range of variability, with Area A samples extending to slightly more primitive (higher MgO wt%) compositions. There is a group of samples, however, that falls off the main trend toward lower FeO* (Figure 3.2; Table 2.1), herein referred to as the Low FeO* group following the naming protocol established by Stewart et al. (2002). The remaining samples that lie along the low-pressure LLD are referred to as the Main Composition group. Compared to most PD samples at a given concentration of MgO (wt%), samples in the Low FeO* group have ~2 wt% less FeO*, forming a trend that is offset from but roughly parallel to the 1-kbar LLD. Low FeO* samples also show subtle variations in CaO and Al_2O_3 concentrations, which are somewhat elevated above the LLD (Figure 3.2).

Overall, the Low FeO* group is dominated by lavas (81% of the low FeO* group are lavas, 19% are dikes). Based on present sampling, Low FeO* lavas and dikes appear to be randomly dispersed across each of the ~5 km wide study areas (Figure 3.3), with

Figure 3.2: (Next Page) Major element variations of (a) FeO*, (b) CaO, and (c) Al_2O_3 for PD dikes (open squares) and lavas (filled circles) from areas A (black) and B (green). Most PD samples fall within the Main Composition group, along the trend defined by low-pressure crystallization (1 kbar LLD). A group of samples, dominated by lavas, is offset from the Main Composition group field toward lower FeO* (Low FeO* samples; red diamonds).

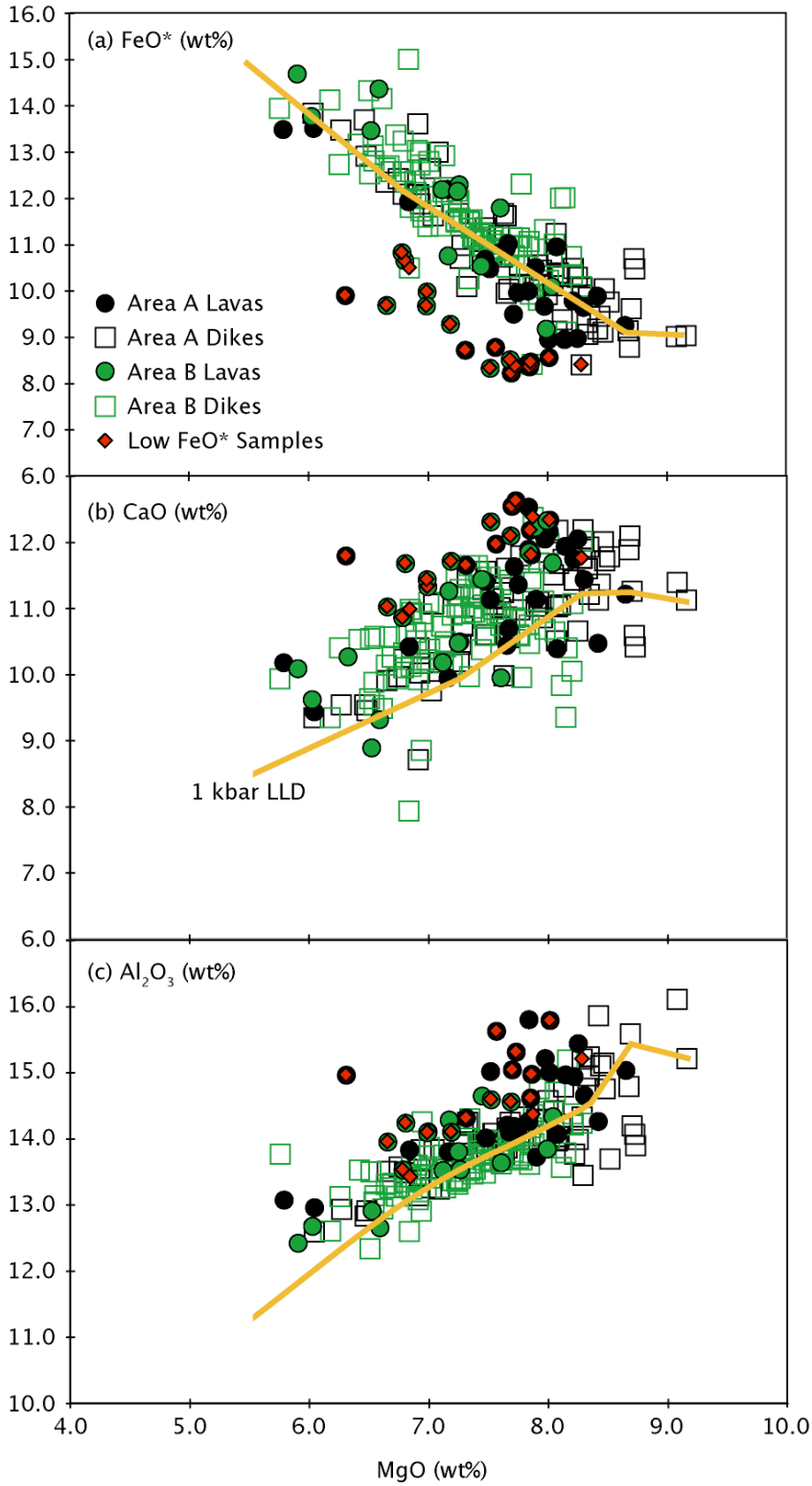
(a) FeO* (wt%)
Area A Lavas
Area A Dikes
Area B Lavas
Area B Dikes
Low FeO* Samples
(b) CaO (wt%)
1 kbar LLD
(c) Al_2O_3 (wt%)
MgO (wt%)

Figure 3.3: (Next Page) Geologic maps of study Areas A and B showing locations of *Alvin* and *Jason II* dive transects (Francheteau et al., 1994; Pito Deep Scientific Party, 2005; Morgan et al., 2005). Symbols indicate PD dikes (open squares) and lavas (filled circles) analyzed in this study, with Low FeO* samples highlighted (red diamonds).

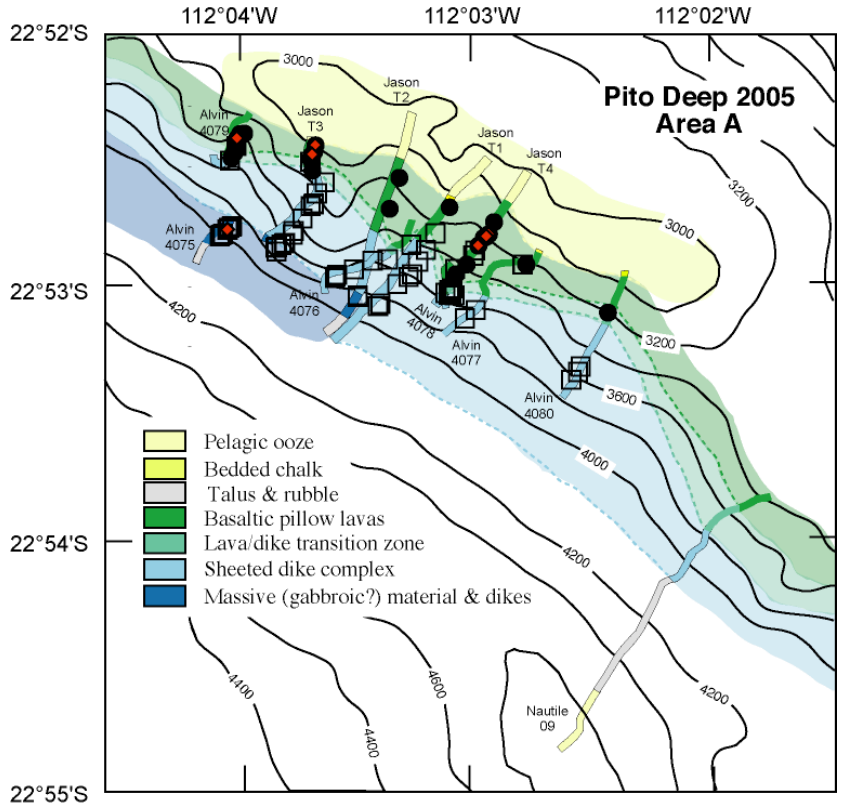
Pito Deep 2005
Area A
112°04'W
112°03'W
112°02'W
22°52'S
22°53'S
22°54'S
22°55'S
Jason T1
Jason T2
Jason T3
Jason T4
Alvin 4075
Alvin 4076
Alvin 4077
Alvin 4078
Alvin 4079
Alvin 4080
Nautile 09
Pelagic ooze
Bedded chalk
Talus & rubble
Basaltic pillow lavas
Lava/dike transition zone
Sheeted dike complex
Massive (gabbroic?) material & dikes

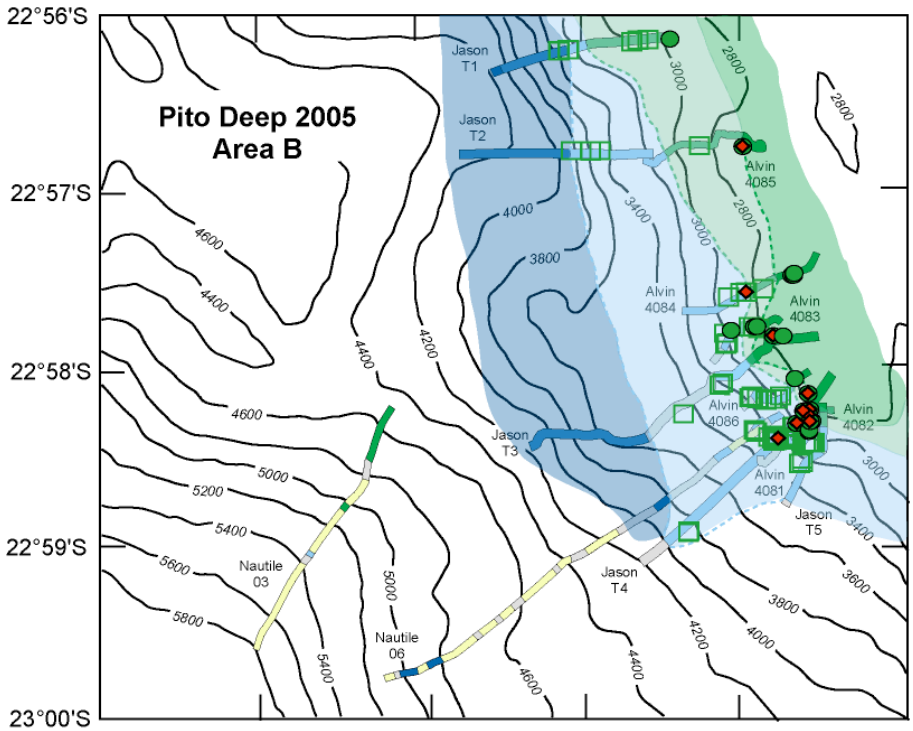
Pito Deep 2005
Area B
111°57'W
111°56'W
111°55'W
111°54'W
111°53'W
111°52'W
22°56'S
22°57'S
22°58'S
22°59'S
23°00'S
Jason T1
Jason T2
Jason T3
Jason T4
Jason T5
Alvin 4081
Alvin 4082
Alvin 4083
Alvin 4084
Alvin 4085
Alvin 4086
Nautile 03
Nautile 06

some suggestion of local clustering (see, e.g., the large number of low FeO* lavas to the east in Area B). Only in one case is a low FeO* dike found in close proximity to low FeO* lavas (see *Jason* transect T4 in Area B). Nearly all of the Low FeO* lavas are confined to the volcanic unit; only 2 Low FeO* lavas were sampled within the lava-dike transition zone. Within the extrusive section, the distribution of Low FeO* lavas is highly variable on short (10s of m) spatial scales (see *Jason* transect T3 in Area A).

The offset of PD lavas to lower FeO* compared to dikes is similar to the chemical distinction observed in HD. Based on strong petrographic evidence showing high proportions (3-13%) of plagioclase phenocrysts in the HD lavas, and the simultaneous offset of the Low FeO* lavas to elevated abundances of CaO and Al_2O_3, Stewart et al. (2003) demonstrated that lava compositions are modified by the accumulation of plagioclase. A similar analysis reveals that the PD Low FeO* samples were likely influenced by plagioclase accumulation as well. Figure 3.4 shows variations in Sr (ppm) and Eu/Eu*, trace element indicators of the behavior of plagioclase during crystallization. The negative Eu anomaly (Eu/Eu* < 1) observed in nearly all PD samples and the overall positive correlation between Eu/Eu* and MgO (wt%) indicate that the fractionating assemblage includes plagioclase, yet some Low FeO* lavas show less pronounced negative Eu anomalies at a given value of MgO (wt%), suggesting that plagioclase was accumulated (or not effectively fractionated) in these samples. Many Low FeO* samples cluster toward higher values of Sr, a possible effect of excess plagioclase, although the high degree of variability suggests that Sr may have been mobilized during low-temperature alteration. Major element variations are also consistent with the effects of accumulated plagioclase, where many of the PD Low FeO* samples show correlated increases in CaO, and, to a lesser degree, in Al_2O_3 (Figure 3.2).

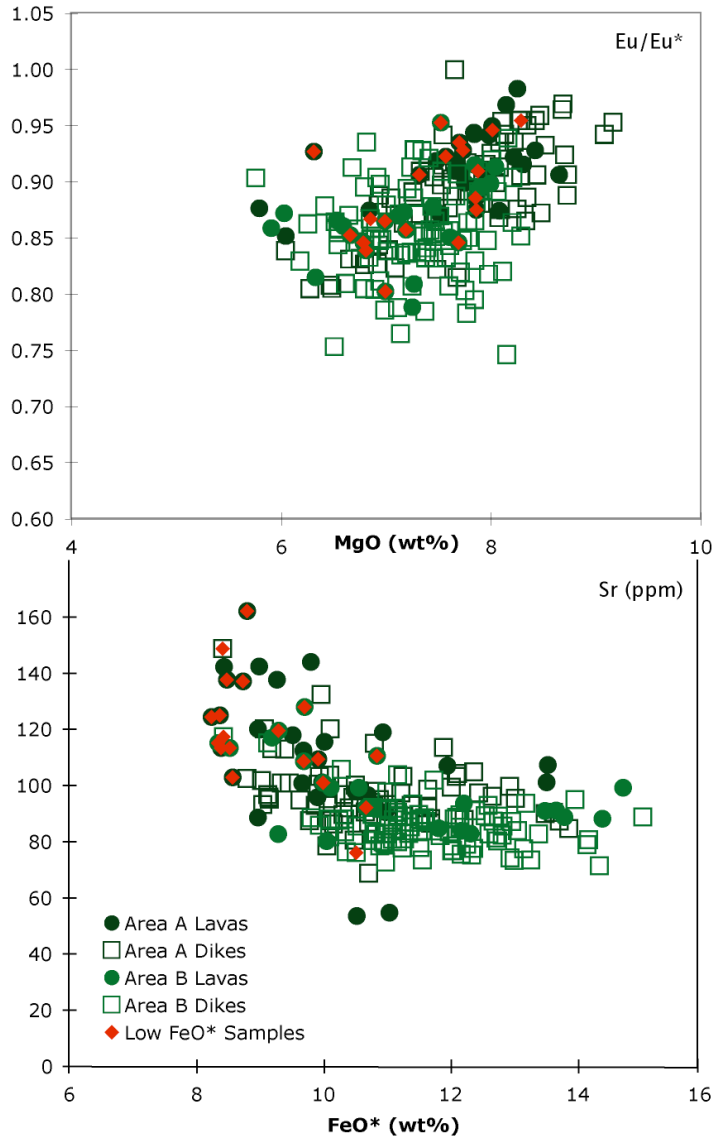

Figure 3.4: Variations in Eu/Eu* vs. MgO (wt%) (top) and Sr (ppm) vs. FeO* (wt%) (bottom) for PD dikes and lavas. Symbols indicate PD dikes (open squares) and lavas (filled circles) analyzed in this study, with Low FeO* samples highlighted (red diamonds).

The effects of plagioclase accumulation can also be observed in PD petrographic analyses, which reveal textural variations similar to those observed in HD. Most of the PD dikes and lavas are aphyric or sparsely porphyritic, containing fewer than 3% phenocrysts, which are predominantly plagioclase laths (<1-2 mm). Visual estimates show that Main Composition group samples typically have a lower abundance of plagioclase phenocrysts (<3%) compared to Low FeO* group samples (3-10%; Figure 3.5). Quantitative analysis of photomicrographs using ImageJ (see Appendix B) shows that, while Main Composition group dikes contain varying amounts of plagioclase (25±6% to 38±5% by area), plagioclase phenocrysts are more abundant in Low FeO* lavas (37±3% by area) compared to Main Composition group lavas (21±9% by area). Although calculations using ImageJ yield higher estimates of plagioclase abundance compared to visual observations of hand samples and thin sections, the first-order correlation of major and trace element chemistry to petrographic observations is consistent with similar observations from HD that are interpreted to indicate plagioclase accumulation.

Although chemical variations in dikes and lavas from PD and HD are largely similar, the exposures vary in the intensity of the compositional distinction. A majority (~65%) of lavas from HD fall into the low FeO* field, while only a quarter of the lavas sampled in PD show Low FeO* compositions. Naturally, the unexpected observation of chemically distinct dikes and lavas from two separate tectonic windows introduces a question of commonality: Does a similar chemical offset occur in other dike-lava populations and what governs the intensity of this effect?

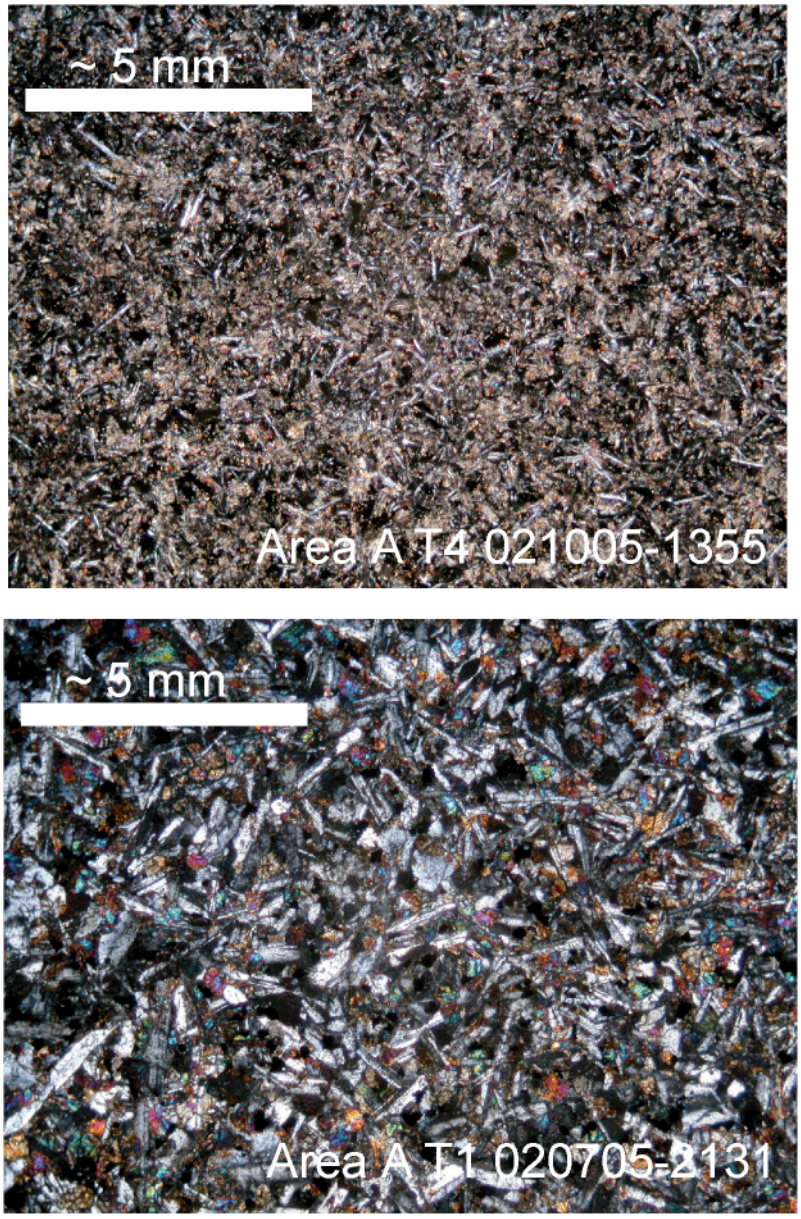

Figure 3.5: Photomicrographs of sample 021005-1355 (top), a lava from Area A representative of Low FeO* Group samples, and sample 020705-2131 (bottom), a dike from Area A representative of Main Composition Group samples. Both images are magnified 20x under crossed-polars. Dikes contain a wide range of plagioclase phenocrysts, but Low FeO* lavas generally show a higher abundance of plagioclase compared to Main Composition Group lavas.

3.3 Comparison of PD Dikes and Lavas to Other Dike-Lava Populations

Until recently, geochemical analyses of spatially associated *in situ* dikes and lavas from oceanic crust have been largely unavailable. The growing number of dike-lava studies in intermediate- to super-fast spread crust is still limited (Figure 3.6), yet an examination of the available data reveals geochemical variations similar to those observed in dikes and lavas from PD and HD. DSDP/ODP Hole 504B, located in 5.9 Ma crust, sampled *in situ* dikes and lavas formed at the intermediate (~72 mm/yr) spreading Costa Rica Rift (Alt et al., 1993; Anderson et al., 1985; Becker et al., 1988; Cann et al., 1983; Dick et al., 1992). While dikes and lavas from Hole 504B are known to be remarkably similar (Natland et al., 1983; Autio et al., 1989; Bach et al., 1996; Pedersen and Furnes, 2001), a comparison to lavas from nearby Hole 896A, located ~1 km to the southeast (Alt et al., 1996; Brewer et al., 1996), reveals that lavas are generally offset in the direction of lower iron.

A more prominent difference in dike and lava composition occurs in samples from the northern Oman ophiolite, which consists of blocks of crust thought to represent fast-spread oceanic lithosphere (Tilton et al., 1981; Nicolas, 1989; MacLeod and Rothery, 1992; Nicolas et al., 1994). Since subduction zone and post accretion volcanism have also been recognized in the Oman ophiolite, our examination of dikes and lavas is limited to those than have been related to spreading center processes in previous studies (Alabaster et al., 1982; Umino et al., 1990; Ishikawa, 2002). Examination is also restricted to the freshest samples (LOI <2.5 wt%), as all of the dikes and lavas have been altered to various degrees. Like the HD and PD data, lavas from northern Oman define a Low FeO* field

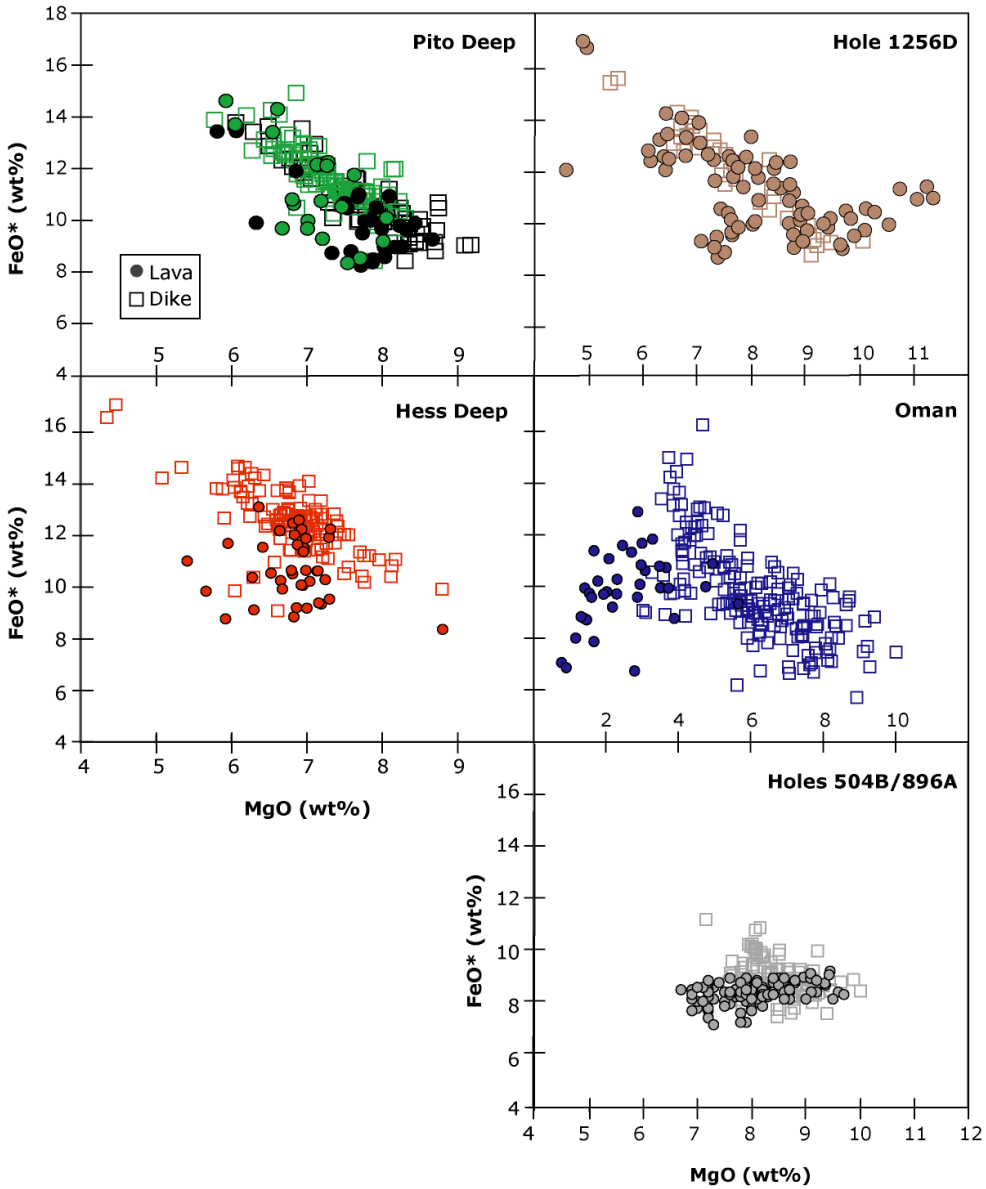

Figure 3.6: Comparison of compositions of dikes (open squares) and lavas (filled circles) from intermediate- to super-fast spread crust. Note the change in scale for MgO: Pito Deep and Hess Deep (4-10 wt%); Holes 1256D, 504B/896A (4-12 wt%); Oman (0-12 wt%). Data for Hole 504B/896A from Natland et al., 1983; Autio et al., 1989; Bach et al., 1996; Brewer et al., 1996; Pedersen and Furnes, 2001; Hess Deep from Stewart et al., 2003; Oman from Rochette et al., 1991; Einaudi et al., 2000; Einaudi et al., 2003; Godard et al., 2003; Miyashita, et al., 2003; Umino et al., 2003; 1256D from Wilson et al., 2006; Pito Deep, this study.

that is clearly distinct from the Fe enrichment trend defined by the dikes (Rochette et al., 1991; Einaudi et al., 2000; Einaudi et al., 2003; Godard et al., 2003; Miyashita, et al., 2003; Umino et al., 2003).

The examples above suggest that that the geochemical offset between dikes and lavas is common, yet not all dike-lava populations show this distinction. For example, samples from IODP Hole 1256D, which penetrates into ancient (12-19 Ma) Cocos Plate crust interpreted to have formed at super-fast spreading rates (up to 220 mm/yr; Wilson et al., 2006), show no systematic geochemical offset of lavas from dikes. Most 1256D dikes form a general trend of increasing FeO* with decreasing MgO, but lava compositions are highly variable, offset to higher and lower abundances of FeO* compared to dikes at the same value of MgO (Wilson et al., 2006).

Unfortunately, the number of studies from ophiolites or *in situ* ocean crust where one can compare the compositions of associated dikes and lavas is quite limited. At Endeavor Deep, for example, lavas and dikes were collected, but only lava analyses are available at this time (Natland and Pockalny, 2006; J. Natland pers. comm.). Similarly, for the Blanco Transform, a large suite of lavas was collected and analyzed (Pollock et al., 2005) but there are uncertainties as to whether the few analyses reported as massive diabase represent dikes (Juteau et al., 1995; Naidoo, 1998). Nevertheless, among the data sets examined to date (HD, PD, Hole 504B/896A, Hole 1256D, and the northern Oman ophiolite), the chemical distinction between dikes and lavas is observed in four of the five areas. Based on these five studies, there appears to be a rough correlation between spreading rate and the magnitude of the chemical distinction. Ocean crust formed at intermediate- to fast-spreading rates, such as Hole 504B/896A, HD, and the Oman ophiolite shows a greater proportion of lavas offset in composition from dikes. In

contrast, PD and Hole 1256D, crust produced by super-fast spreading, show, respectively, a weak geochemical offset and no offset. Additional data at a variety of spreading rates will be required to confirm this observation, but for the present, the existing data suggest some mechanism acts to partition different magma types between the lava and dike units.

3.4 Influence of Magma Composition on Density

The systematic offset of lavas to lower FeO* compositions compared to dikes from the same location is interesting in the context of melt density. The relationship between magma density and composition has been examined previously (Bottinga and Weill, 1970; Stolper and Walker, 1980; Lange and Carmichael, 1990). Bottinga and Weill (1970) developed an empirical approach for calculating liquid density from the major element composition of volcanic glass based on the partial molar volume of the oxide in a liquid. Subsequently, Lange and Carmichael (1990) developed a method that also includes the effect of compressibility. This widely used method for calculating melt density, however, assumes that all mineral phases are dissolved. Thus, the density calculated for a magma that includes both melt and crystals will differ from that calculated for a melt, depending on the densities of the minerals present and their abundances. Because plagioclase tends to dominate phenocryst populations of most phyric basalts erupted at ocean ridges, a magma density calculated using the approach of Lange and Carmichael (1990) is therefore likely to be a maximum density.

With this caveat in mind, we followed the approach of Lange and Carmichael (1990) and Stewart et al. (2003) to calculate liquid densities for the PD dikes and lavas (Figure 3.7). Overall, the PD liquid densities range from 2.67 gcm^{-3} to 2.75 gcm^{-3}. On

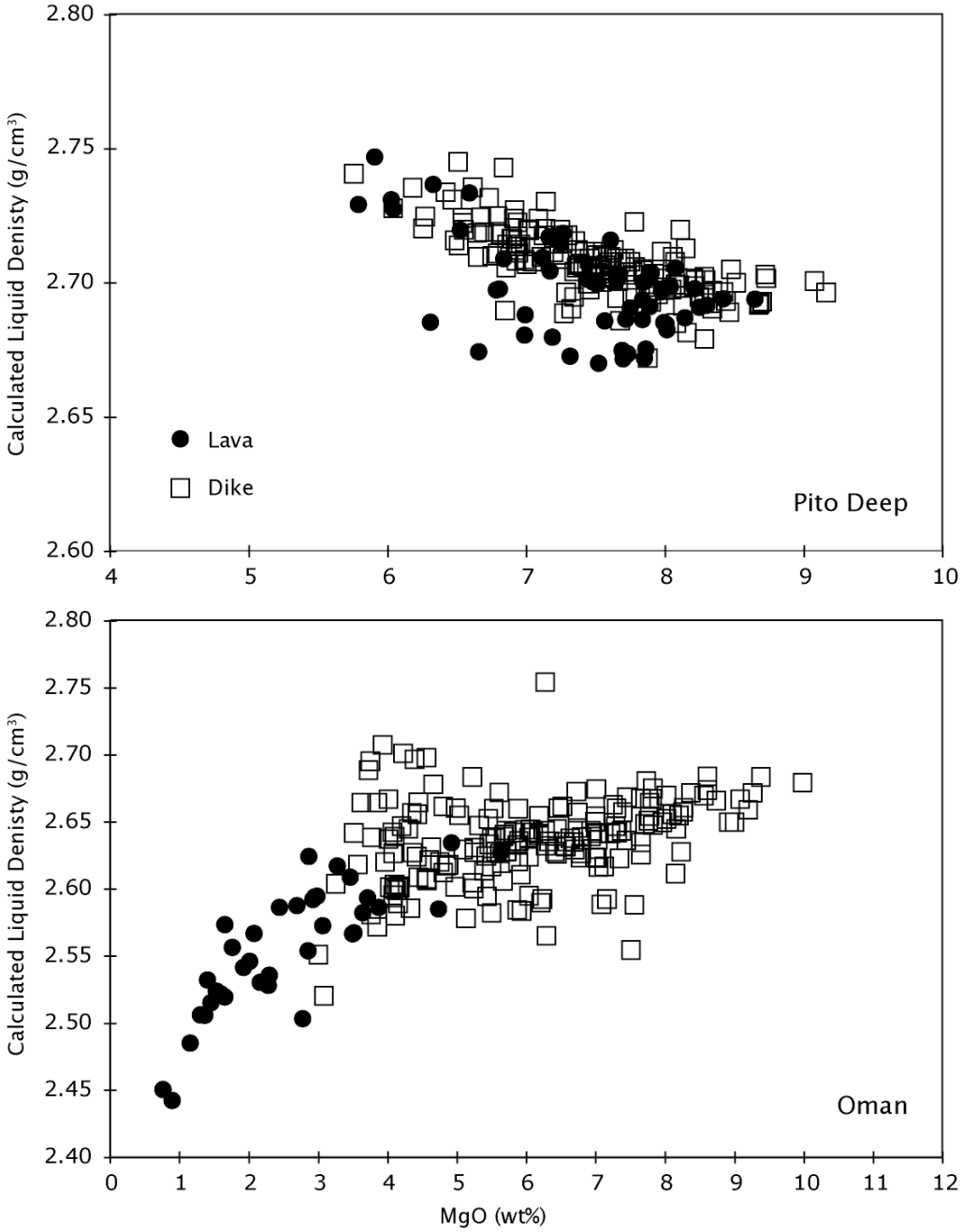

Figure 3.7: Calculated liquid density (gcm^{-3}) vs. MgO (wt%) for PD (top) and Oman ophiolite (bottom) dikes (open squares) and lavas (filled circles) following the approach of Stewart et al. (2003) and Lange and Carmichael (1990).

average, PD dikes (2.71 gcm^{-3}) and lavas (2.70 gcm^{-3}) have similar liquid densities, consistent with previous work that shows ~73% of MORB glasses have densities of 2.70 ± 0.02 gcm^{-3} (Hooft and Detrick, 1993). The similarity in dike and lava densities reflects the observation that both span the entire range in compositional variability. When plotted versus MgO (wt%), however, the calculated liquid densities generally mirror patterns in FeO* (Figure 3.6). Separately, PD samples within the Low FeO* group have an average density of 2.68 ± 0.01 gcm^{-3}, 0.02 gcm^{-3} lower than the average density for Main Composition group samples (2.71 ± 0.01 gcm^{-3}).

The contrast in density between the PD Low FeO* and Main Composition groups is similar to density differences calculated for the HD dikes and lavas. Most HD lavas fall within the Low FeO* group, which has an average density of 2.68 ± 0.02 gcm^{-3} while HD dikes average 2.72 ± 0.02 gcm^{-3}(a 0.04 gcm^{-3} difference in density; Stewart et al., 2003). Calculated melt densities for dikes (2.64 ± 0.03 gcm^{-3}) and lavas (2.56 ± 0.04 gcm^{-3}) from the northern Oman ophiolite are generally lower than *in situ* samples from tectonic windows, yet show a comparable density contrast (0.08 gcm^{-3}). Presumably, a similar density contrast between dikes and lavas occurs to some degree in IODP Hole 1256D and DSDP/ODP Holes 896A and 504B (Figure 3.6), based on the correlated relationship between calculated liquid density and FeO*. Thus, while the data sets available to compare compositions and densities of dikes and lavas are limited, there is a common, though not ubiquitous, offset of lavas toward lower FeO* and lower density compositions compared to dikes.

3.5. Factors that Govern Magma Eruptability

A great deal of theoretical work has focused on the factors that govern dike

propagation (Delaney, 1987; Pollard, 1987; Lister and Kerr, 1991; Hooft and Detrick, 1993; Rubin, 1995; Ida, 1999; Buck et al., 2006), which determines the conditions required for a dike to pierce the surface and erupt lavas. In general, an eruption occurs when a dike propagates to the surface with excess pressure (Buck et al., 1997). Driving forces for dike growth are dominated by gradients in crustal stress along the length of the dike, initial magma pressure at the source of the dike, and magma buoyancy (Lister and Kerr, 1991; Rubin, 1995).

Within a gravity field, magma with a lower density relative to the surrounding crust is driven upward by buoyancy forces. Therefore, low density magmas, which should ascend to higher crustal levels than high density magmas, should be more eruptable. Stolper and Walker (1980) calculated a theoretical curve that predicts the evolution of the liquid density during the fractional crystallization of a basaltic melt. The majority of MORB lie within the minimum of this density curve (~2.7 gcm^{-3}; Stolper and Walker, 1980; Sparks et al., 1980; Hooft and Detrick, 1993), suggesting that low-density melts are preferentially erupted as lavas.

Buoyancy as a primary driving force for dikes is complicated by the intrusion of magma through crust that has a stratified density structure, which introduces the notion that magma will come to rest at its level of neutral buoyancy (LNB; Ryan, 1987). The LNB is defined as the position where the magma density is equal to the density of the surrounding host rock (Ryan, 1987; Ryan, 1993). For the fast-spreading northern EPR, the LNB was determined to lie between 100 m and 400 m below the surface (Hooft and Detrick, 1993), suggesting that dikes driven by buoyancy alone should not be able to ascend to the surface and erupt lavas. The response of a vertically propagating dike that encounters the LNB is complex, yet dikes ascend beyond the LNB when excess

magma pressure or local stress gradients continue to drive the dike vertically (Rubin, 1995). An examination of the effects of magma pressure and crustal stress on dike intrusion is essential to fully explore the role of buoyancy in the partitioning of magma in the upper crust.

3.6 Model for the Intrusion and Eruption of a Single Dike

The approach of Ida (1999) was chosen to test the role of buoyancy in dike intrusion because it examines variations in dike height and width in response to changes in crustal stress and magma pressure. Unlike most models for dike intrusion, Ida does not make the simplification that rock and magma density are equal. The model assumes a 2-dimensional dike with a uniform width that varies over time (Figure 3.8). Normal stress is evenly distributed along the length of the dike. Crustal density is taken to be the bulk average of the upper crust, neglecting the stratified density structure. These and other simplifications (e.g., crack-tip resistance integrated over dike length) imperfectly approximate the complicated dike system, but allow an individual dike intrusion event to be reduced to four simple equations: three ordinary differential equations that describe dike width, height, and magma pressure during dike growth, and one equation that describes changes in mean normal stress (refer to Appendix C).

The equations of Ida (1999) were solved simultaneously using the 4th-order Runge Kutta Solution in Matlab (version 7.2). Dike heights were modeled under varying conditions of tectonic stress, magma pressure, and crustal density for magmas with densities of 2.68 gcm^{-3}, representing Low FeO* lavas, and 2.72 gcm^{-3}, representing Main Composition group dikes. Model results suggest that increased buoyancy of magma, caused by the 0.04 gcm^{-3} difference in density (the average density difference observed

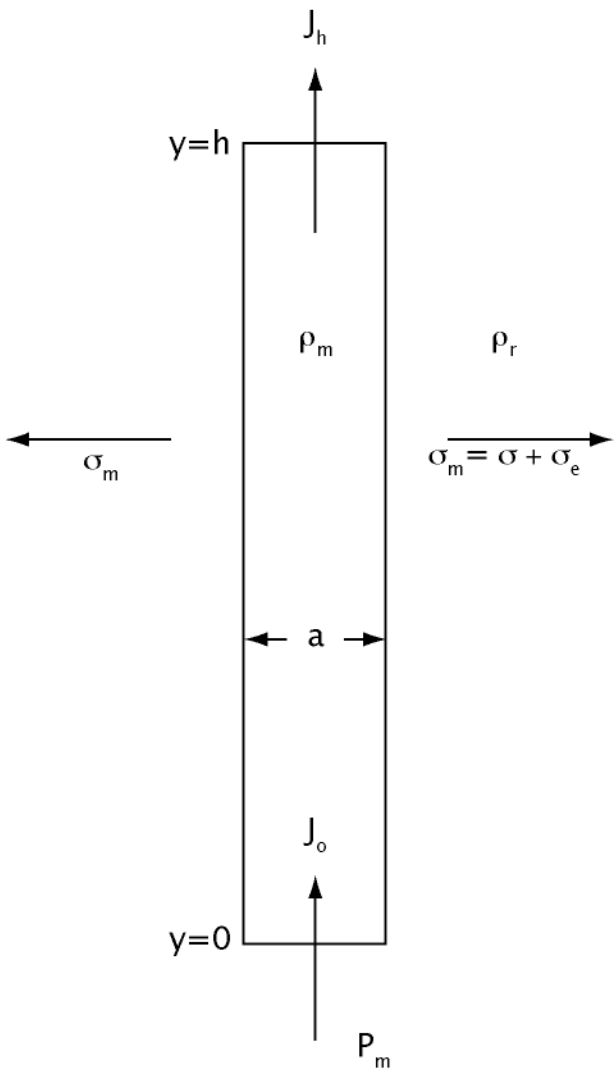

Figure 3.8: Model for intrusion of a single dike, modified after Ida (1999). Magma of a given density (ρ_m) intrudes into upper crust of a given density (ρ_r) through a dike of uniform width (a), which initiates at y=0 and extends at the dike front (y=h) so that flux of magma at the front of the dike (J_h) is balanced with the magma flux into the dike (J_o). Magma pressure (P_m) and mean normal stress (σ_m) are the driving forces for dike growth. Mean normal stress is distributed evenly distributed along the length of the dike and is considered to originate from tectonic stress sustained in the crust (σ) and the resistance of the upper crust to fracturing (σ_e), the latter of which is found by integrating the mean normal stress in a small tip region (not shown) over the length of the dike. Refer to Appendix B for values of variables, model equations, and Matlab code.

between dikes and lavas for HD and PD), drives dikes up to 500 m higher in the crust (Figure 3.9).

To examine the influence of crustal density on magma eruptability, dike intrusion was modeled under conditions of strong deviatoric tension (σ ~12 MPa) and initial magma pressure equal to the buoyancy force ($p_o / p_u = 1$). Crustal density was adjusted to represent ocean crust with differing internal architecture, characterized by varying proportions of low density (extrusive; 2.5 gcm^{-3}) and high density (dike; 3.0 gcm^{-3}) units. As the fraction of lavas in the upper crust decreases, the bulk crustal density increases. Overall, greater overburden density raises the height to which magma can ascend in the crust and increases the probability that a dike will pierce the surface, erupting lava. Thus, within ocean crust with a relatively thin extrusive section (high crustal density), enhanced magma buoyancy should drive a high proportion of dikes to erupt, which ultimately thickens the lava pile, resulting in fewer eruptions and a self-regulated cycle of extrusion (see Buck et al., 1997).

In contrast, the *relative* eruptability of magma, based on density differences, is most emphasized in low density crust (Figure 3.9). As overburden density decreases, the density-dependent difference in dike height becomes greater, enhancing the likelihood that a dike piercing the surface will be transporting low density (Low FeO*) magma. Thus, while fewer intrusions may lead to eruption in ocean crust with low bulk density (relatively thick extrusive section), low density magmas should be strongly favored for eruption. This is opposite for magma intruding into crust with a high bulk density (thinner extrusive unit), where a greater percentage of intrusions may lead to eruption, but buoyancy plays a more minor role in magma partitioning, allowing a wide range of magma densities (and compositions) to erupt as lavas.

Figure 3.9: (Next Page) Difference in dike height (km) between low (2.68 gcm^{-3} dotted line) and high (2.72 gcm^{-3}; solid line) density magmas for changes in crustal density (top), initial magma pressure (middle), and crustal stress (bottom). For variations in dike height with crustal density, a magma pressure equivalent to the driving force of buoyancy ($p_o/p_u = 1$) was used under conditions of relatively strong deviatoric tension (sigma ~12 MPa). While dike heights increase with increasing crustal density, the difference in height between low and high density magmas decreases. For changes in dike height with initial magma pressure, a bulk crustal density of 2.8 gcm^{-3} was used. Both dike height and the density-dependent difference in dike height increase with increasing initial magma pressure. In contrast, dike heights respond in an exact opposite manner for increasing crustal stress. Following the convention of Ida (1999), positive crustal stress indicates deviatoric tension. Increasing deviatoric tension causes the dike heights and the difference in height between low and high density magmas to decrease.

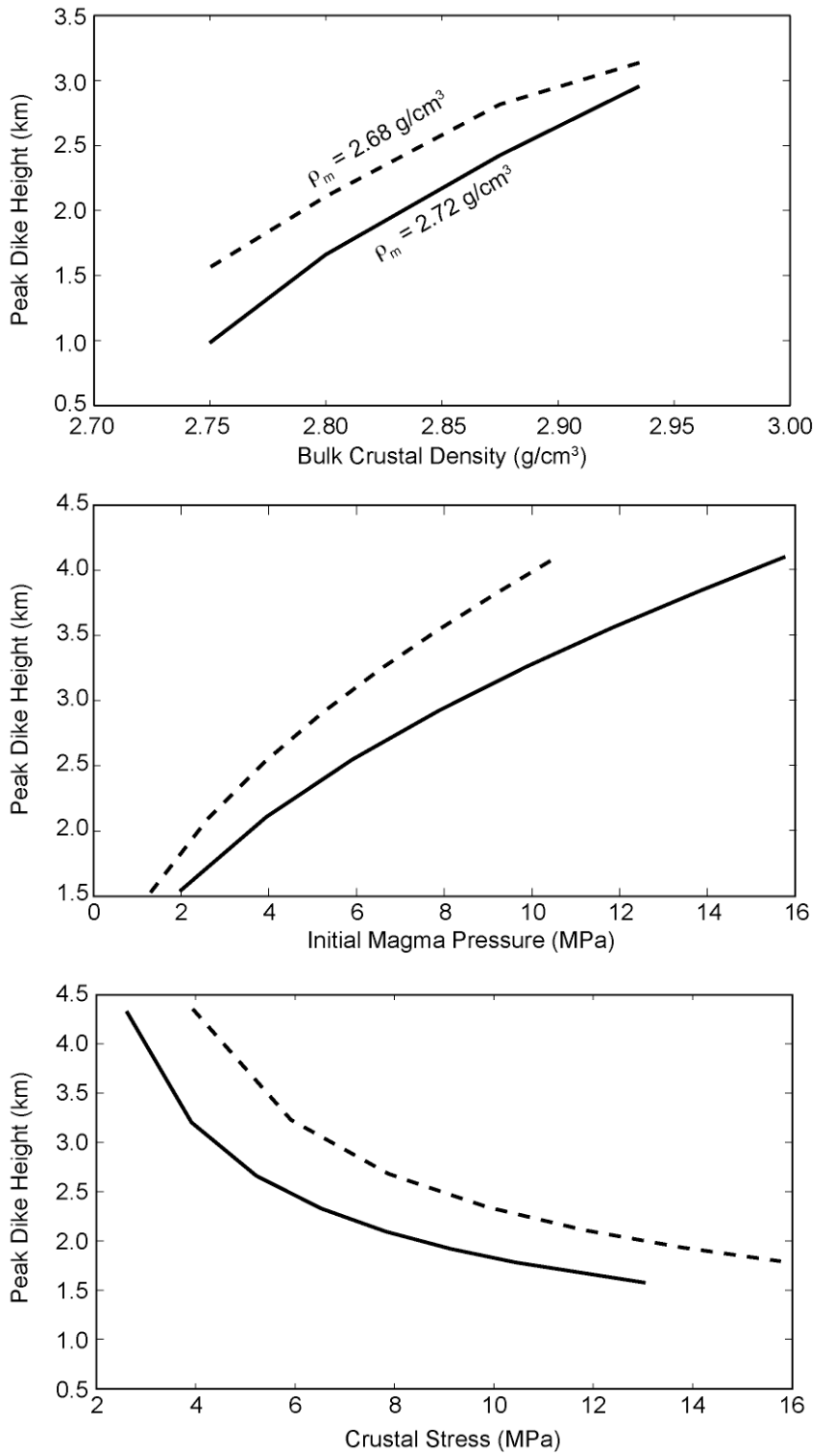
Peak Dike Height (km)
Bulk Crustal Density (g/cm³)
ρm = 2.68 g/cm³
ρm = 2.72 g/cm³
Initial Magma Pressure (MPa)
Crustal Stress (MPa)

Density-dependent differences in dike height are also enhanced by increases in initial magma pressure (p_o), which is thought to be on the order of a few MPa (Rubin, 1995; Gudmundsson, 2002; Acocella et al., 2006; Figure 3.9). In ocean crust consisting of 40% extrusives (bulk ρ = 2.8 gcm^{-3}) and an initial magma pressure ~5 MPa, lower density dikes consistently ascend to greater heights, indicating that buoyancy alone drives magma higher in the crust. As initial magma pressure rises, the difference in height between low and high density magmas increases, suggesting that additional magma pressure beyond the force of buoyancy raises the likelihood that low density magmas will be selected for eruption over high density magmas. Thus, at higher magma pressures, buoyancy plays a greater role in partitioning magma based on density.

Dike height responds to crustal stress (σ) in a more complex manner. In the convention of Ida (1999), positive crustal stress indicates deviatoric tension. Under conditions of weak deviatoric tension and compression, Ida (1999) found that unlimited dike growth occurs. As deviatoric tension increases, dikes widen to accommodate the crustal stress, which reduces the upward driving force for dike growth and stops dikes at a finite height. For the given magma densities and an initial magma pressure equal to the buoyancy force ($p_o / p_u = 1$), finite dike growth occurs for crustal stresses >2.6 MPa.

Peak dike height and density-dependent differences in dike height are inversely related to deviatoric tension. This relationship of dike height to crustal stress complicates the role of buoyancy in the partitioning of magma in the upper crust. If eruptions are more likely to occur when dike height increases, then weak deviatoric tension should favor eruptions in general. However, since weak deviatoric tension also enhances the difference in height between low and high density magmas, low density (Low FeO*) magmas should be strongly favored for eruption. The difference in dike

height between low and high density magmas is on the order of 1 km at a crustal tension of ~5 MPa, the average tensile strength of basaltic rocks (Gudmundsson, 2002), but dike reach heights >2.5 km. Hence, density should play a major role in the partitioning of magma between dikes and lavas under conditions of weak deviatoric tension, but the "signature" of buoyancy controlled magma partitioning may not be observed if the height to which magma (of any density) can ascend is sufficient to pierce the surface. Likewise, magma intruding into ocean crust experiencing strong deviatoric tension (> 5 MPa) should show little preference for low density lavas, based on the small difference in dike height, and should result in fewer eruptions, due to overall shorter dike heights. The short dike heights must be sufficient to reach the surface, however, because eruptions are known to be more frequent at faster spreading rates. Thus, while density based magma partitioning should be more significant as deviatoric tension weakens, the ultimate effects of magma buoyancy depend on the relationship of peak dike height to the height required to pierce the surface.

The Ida formulation remains the current model best suited to test the role of magma buoyancy in dike intrusion, yet the accuracy of the output must be examined within the uncertainty of the model simplifications. In Ida's formulation, dike heights are insensitive to the size of the tip region and magma viscosity. The constants used to describe the crust in this model (e.g., Young's Modulus (μ), Poisson's ratio (ν)) are similar to published values for basaltic crust (Rubin, 1995; Gudmundsson, 2002; Buck et al., 2006), and variations in ν have little effect on dike height (<3% difference), but variations of 10 MPa in μ cause dike heights to change by 100s of meters. Dike heights, however, are most sensitive to changes in propagation length (L) and the elastic response of the magma chamber (k), in which reasonable variations (L = 1 to 8 km; k =

1.2×10^{-4} to 7.8×10^{-3} MPa) create differences in dike height up to ~1 km. Thus, while the model results reveal that changes in crustal density, initial magma pressure, and crustal stress cause variations in dike heights over a range of <1 km, other input parameters, such as dike length and nature of the magma chamber, also influence the magnitude of dike height.

The true significance of the model results, however, lies in the demonstration that magma buoyancy plays a role in determining dike height and the role of buoyancy changes with varying conditions of spreading. Under all conditions, lower density magma rises to greater heights in the crust compared to higher density magma. Overall, the model for intrusion of a single dike, summarized in Figure 3.10, predicts that buoyancy plays the greatest role in magma partitioning along spreading centers with lower bulk crustal density, greater initial magma pressure, and weaker crustal deviatoric tension. Thus, the distinction in chemistry (and density) between dikes and lavas should be most prominent in ocean crust with relatively thick extrusive units (low bulk density), formed at relatively slower spreading rates, assuming that the magnitude of crustal deviatoric tension and initial magma pressure for intrusion can be directly related to spreading rate. In contrast, ocean lithosphere formed at faster spreading rates, in which lavas compose a smaller portion of the upper crust, should exhibit little to no geochemical distinction between dikes and lavas. These model predictions can be examined in the chemistry of available dike-lava populations, which are quite limited, but demonstrate a rough correlation between spreading rate and intensity of chemical offset between dikes and lavas.

3.7 Implications for Magma Partitioning at Intermediate- to Super-fast Rate Spreading Centers

An examination of dike-lava populations from ocean crust confirms model results that predict that the effect of buoyancy on magma partitioning is greatest in ocean crust with low bulk density, low crustal deviatoric tension, and high initial magma pressure (Figure 3.10). Indeed, the greatest contrast in the density (and chemistry) of dikes and lavas occurs at intermediate- to fast-rate spreading centers (HD, Hole 504B/896A, Oman), while negligible or minor density distinctions are observed in super-fast rate crust (PD, Hole 1256D; Figure 3.6). Considering the effects of bulk crustal density on magma partitioning, low density magma should be strongly favored for eruption in low density ocean crust similar to HD and Hole 504B/896A, which consists of relatively thick (up to ~800 m depth) extrusive units underlain by a dike complexes >1000 m thick (Cann et al., 1983; Anderson et al., 1985; Becker et al., 1988; Dick et al., 1992; Francheteau et al., 1992; Alt et al., 1993; Karson et al., 2002a). Lower bulk crustal density at intermediate- to fast-rate spreading centers results in stronger chemical partitioning between dikes and lavas compared to magma intruding into higher density crust formed at super-fast spreading rates (PD, Hole 1256D), in which lavas <500 m thick lie above >1000 m thick dikes (Francheteau et al., 1994; Morgan et al., 2005).

Likewise, the effect of crustal deviatoric tension on density-dependent magma partitioning is also observed in the dike-lava populations. Assuming that the magnitude of crustal deviatoric tension is greater at faster spreading rates, buoyancy should play a less pronounced role in magma partitioning as spreading rate increases. As predicted,

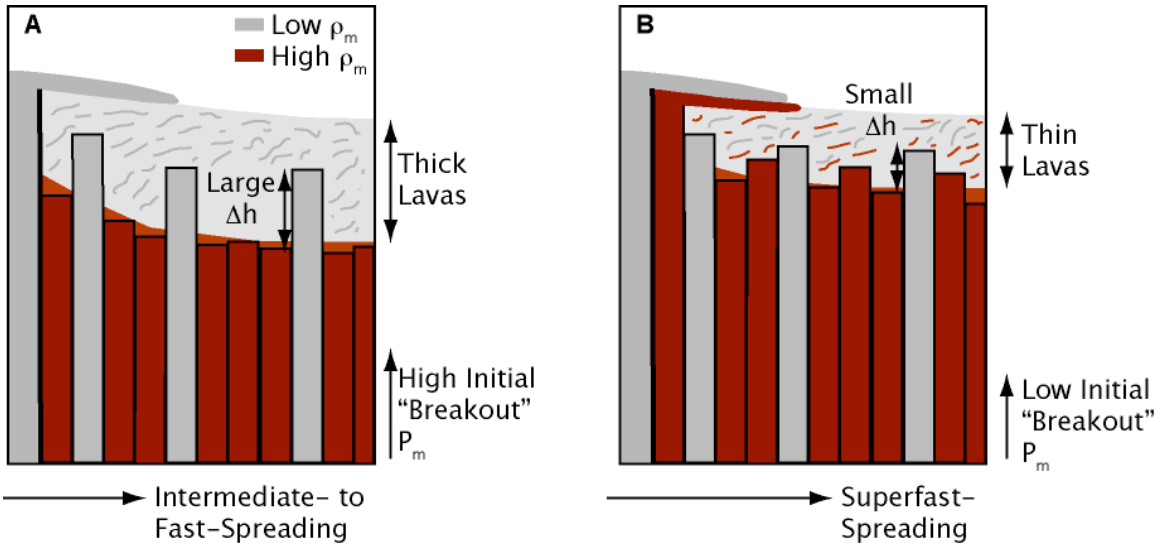

Figure 3.10: Summary of buoyancy-controlled magma partitioning between dikes and lavas. At intermediate- and fast-rate spreading centers (a), the relatively thick extrusive section, high initial breakout magma pressure, and weak deviatoric tension result in a large difference in dike height between low and high density magmas, leading to the enhanced eruptability of low density magma. The resulting upper crust consists of lavas that show a prominent offset in composition from the underlying dike complex. At super-fast spreading centers (b), relatively thinner extrusives, lower initial breakout pressures, and stronger deviatoric tension lead to a small difference in dike height between low and high density magmas. Buoyancy plays less of a role in determining the composition of magma that gets erupted, resulting in an extrusive section with little to no compositional offset from the underlying dikes.

lavas erupted along super-fast spreading centers show little or no preference for low density compositions compared to dikes (e.g., PD, Hole 1256D). This is in contrast to lavas erupted at intermediate- to fast-rate spreading centers, where weaker crustal deviatoric tension results in stronger density-controlled partitioning of magma between dikes and lavas (HD, Hole 504B/896A).

The effect of initial magma pressure on buoyancy controlled magma partitioning can be observed in the dike-lava populations when initial "breakout" pressures are considered. Breakout pressure is the magma pressure required for dike initiation, which depends on the resistance of the overlying crust to fracture and the magnitude of the tectonic stress (Buck et al., 2006). If we assume that the response of ocean crust to fracturing is largely similar, then breakout pressure is primarily determined by the magnitude of crustal deviatoric tension. Dikes intruding into crust under strong deviatoric tension require lower initial magma pressures to initiate whereas growth of dikes intruding under weaker crustal deviatoric tension demand higher initial magma pressures. While it seems logical to relate initial magma pressure to magma supply, assuming that robust magmatism at faster spreading centers creates greater initial magma pressures, the concept of breakout pressure suggests that the opposite may occur: compared to intermediate- and fast-rate spreading centers, magma intruding along super-fast spreading centers may experience lower initial magma pressures due to the stronger tectonic deviatoric tension. Thus, the prominent geochemical (and density) distinction between dikes and lavas in crust formed at intermediate- to fast-spreading rates may reflect high initial magma pressures required for dike initiation, in contrast to dikes and lavas formed at a super-fast spreading rate, where lower initial magma pressures result in a more minor role of buoyancy in magma partitioning.

3.8 Conclusions

An examination of dikes and lavas from Pito Deep reveals that lavas are systematically offset toward lower FeO* (lower density) compositions compared to dikes, a characteristic that is not unique to Pito Deep, but also occurs to various extents in other dike-lava populations from ocean crust formed at intermediate- to super-fast spreading rates. A rough correlation was identified between spreading rate and the intensity of the geochemical distinction, where the compositional contrast between dikes and lavas is greatest in intermediate- to fast-rate crust, which can be related to factors that govern dike intrusion and eruption.

A model for the intrusion of a single dike shows that low density magmas are strongly selected for eruption when dikes with high initial magma pressures intrude into low density crust experiencing weak tectonic deviatoric tension, a prediction that is confirmed in analyses of dikes and lavas from Hess Deep Rift, Oman ophiolite, and DSDP/ODP Holes 504B/896A. Dikes and lavas from ocean crust formed at super-fast rate spreading centers (PD and Hole 1256D) show a minor geochemical distinction, suggesting that buoyancy plays less of a role in magma partitioning at faster spreading rates.

Undoubtedly, additional analyses of dike-lava populations from various spreading rates are required to obtain a full understanding of density-filtering in the upper crust. Other factors controlling dike intrusion, such as changes in local stress during an intrusion sequence (e.g., Buck et al., 2006), must also be considered. Density-based partitioning of magma between dikes and lavas has important implications for the construction of the upper oceanic crust, bearing on the composition of lavas that are erupted. As the role of buoyancy in magma partitioning emerges, we can begin to gain a

more complete understanding of the processes that occur during the accretion of the upper ocean crust.

Appendix A: Pito Deep Chemical Analyses

Major and trace element data for 206 fresh whole rock samples from Pito Deep. [1]Morphology refers to dike (d), pillow (p), massive (m), sheet flow (s), or talus (t). [2]Lithologic zone refers to dike unit (D), volcanic unit (V), dike-lava transition zone (T), and gabbro-dike transition zone (GDT). [3]Samples that fall into the Low FeO* Group are marked. Major element oxides are reported in weight%; trace elements in ppm. FeO* is total Fe recalculated as FeO. Mg# is calculated as cation mole % [Mg/[Mg+Fe)]. Major elements and Sr, Sc, Zn, and V were analyzed by DCP. Reproducibility for DCP analyses is 1-2% for all major and minor elements with the exception of the following: <5% for K. The remaining trace elements were analyzed by ICP-MS, for which the reproducibility is 1-3% for REE and 1-4% for all other elements except Cs (<5%) and U (<5%). Replicate analyses of standards are in agreement with previously published values (see electronic database of Stewart et al., 2002).

Sample ID	020705-1207	020705-1219	020705-1408	020705-1438	020705-1451	020705-2131	020705-2225	020705-2317	020805-0108	020805-1035	020805-1048	020805-1439
Study Area	A	A	A	A	A	A	A	A	A	A	A	A
Jason Transect	1	1	1	1	1	1	1	1	1	2	2	2
Morphology[1]	d	d	d	d	d	d	d	d	p	m	m	m
Lithologic Zone[2]	D	D	D	D	D	D	D	T	V	D	D	D
Depth (mbsl)	3874.9	3830.2	3657	3592	3601	3523	3425	3310	3042	4003	3982	3388
Latitude (°S)	22.885	22.885	22.884	22.883	22.883	22.882	22.881	22.880	22.878	22.885	22.885	22.882
Longitude (°W)	112.058	112.058	112.056	112.056	112.056	112.055	112.055	112.054	112.051	112.061	112.061	112.059
SiO_2 (wt%)	48.56	49.69	51.78	50.30	50.30	50.18	49.92	51.16	50.60	51.16	50.43	48.85
TiO_2	1.21	1.41	1.44	1.36	1.56	1.28	1.15	1.51	1.53	1.44	1.42	1.08
Al_2O_3	15.86	14.33	13.90	14.42	13.66	13.70	15.59	14.04	14.94	14.03	14.23	16.10
Fe_2O_3	10.20	11.28	11.89	11.23	12.03	10.85	9.77	11.62	10.88	10.15	11.46	10.02
FeO*	9.18	10.15	10.70	10.11	10.82	9.77	8.79	10.45	9.79	9.13	10.31	9.01
MnO	0.18	0.16	0.22	0.17	0.22	0.18	0.16	0.18	0.18	0.15	0.24	0.18
MgO	8.42	7.77	7.27	8.05	7.53	8.51	8.69	7.95	8.21	8.08	8.10	9.08
CaO	11.13	11.80	10.46	11.51	11.24	11.78	12.10	10.86	11.75	12.18	11.05	11.39
Na_2O	2.89	2.79	2.75	3.11	2.58	2.41	2.49	2.56	2.60	3.04	3.05	2.24
K_2O	0.13	0.05	0.04	0.11	0.03	0.05	0.10	0.07	0.23	0.08	0.06	0.07
Total	98.57	99.28	99.75	100.27	99.15	98.95	99.96	99.96	100.92	100.32	100.03	99.02
Low FeO* Grp[3]												
Mg#	62.1	57.7	54.8	58.7	55.3	60.8	63.8	57.6	59.9	61.2	58.3	64.2
LOI	2.0	0.7	0.9	1.8	1.8	1.5	1.3	1.2	0.5	0.9	1.6	1.8
Sr (ppm)	115	85	78	91	101	92	108	102	147	98	101	105
Ba	2.35	2.54	2.59	3.58	3.53	2.08	1.86	2.89	16.95	1.37	2.48	1.58
Zn	52	45	75	43	63	52	73	81	87	52	68	66
Cu	107	59	74	90	70	63	65	50	64	9	71	57
Ni	98	70	61	65	58	64	98	56	117	64	63	131
V	246	318	250	328	347	324	260	340	314	343	334	245
Sc	38.1	40.1	39.3	41.8	42.3	43.9	38.3	41.4	39.2	44.4	43.2	37.3
Cr	331	254	205	255	147	262	308	138	325	210	166	361
P	462	885	439	521	823	1069	247	1462	1756	872	1263	879
Y	29	33	29	30	36	27	26	32	34	32	31	26
Zr	83	95	48	96	92	68	72	88	114	71	66	62
Be	0.44	0.48	0.34	0.42	0.56	0.38	0.34	0.44	0.66	0.42	0.44	0.39
Co	44.0	43.7	44.1	41.4	42.6	39.9	39.6	41.8	41.4	35.8	42.0	44.5
Rb	0.11	0.03		0.12	0.05	0.01	0.17	0.16	1.74	0.15	0.16	0.18
Nb	0.76	1.07	0.60	1.32	1.59	0.91	0.63	1.27	4.29	0.98	1.30	0.85
Cs	0.007	0.004	0.003	0.004	0.006	0.002	0.017	0.008	0.021	0.005	0.010	0.009
La	1.88	2.11	1.29	2.25	2.78	1.55	1.67	2.34	4.51	1.77	2.28	1.69
Ce	7.09	7.89	4.99	8.19	10.02	5.95	6.41	8.62	13.54	6.93	8.35	6.34
Pr	1.33	1.47	1.00	1.50	1.82	1.16	1.20	1.62	2.20	1.32	1.55	1.16
Nd	7.33	8.25	6.08	8.32	9.90	6.65	6.81	9.03	11.19	7.59	8.69	6.33
Sm	2.72	3.16	2.68	2.99	3.53	2.57	2.51	3.26	3.65	2.93	3.21	2.35
Eu	1.00	1.11	1.03	1.04	1.22	0.94	0.94	1.15	1.26	1.05	1.16	0.86
Gd	3.75	4.32	4.23	4.21	4.88	3.72	3.47	4.52	4.76	4.04	4.32	3.30
Tb	0.70	0.81	0.78	0.77	0.90	0.68	0.65	0.82	0.87	0.80	0.82	0.63
Dy	4.76	5.45	5.26	5.12	5.96	4.70	4.43	5.57	5.76	5.36	5.40	4.24
Ho	1.02	1.15	1.08	1.10	1.28	0.98	0.94	1.16	1.23	1.17	1.16	0.92
Er	2.80	3.15	2.89	2.92	3.46	2.77	2.65	3.25	3.42	3.20	3.17	2.53
Yb	2.77	3.03	2.74	2.86	3.45	2.70	2.52	3.17	3.43	3.12	3.05	2.49
Lu	0.44	0.47	0.42	0.45	0.56	0.42	0.39	0.50	0.53	0.48	0.47	0.40
Hf	2.15	1.30	1.77	1.36	2.03	1.54	1.67	1.85	2.90	1.65	1.73	1.68
Ta	0.07	0.09	0.06	0.10	0.12	0.07	0.06	0.10	0.29	0.08	0.10	0.07
Pb	0.491	0.339	0.195	0.157	1.276	0.132	0.138	0.232	0.592	0.149	0.255	0.209
Th	0.046	0.041	0.045	0.039	0.069	0.027	0.037	0.050	0.272	0.032	0.053	0.047
U	0.055	0.068	0.019	0.044	0.022	0.011	0.004	0.023	0.110	0.010	0.011	0.010
Y/Nb	38	31	48	23	23	30	41	25	8	32	24	30
Nb/Ta	11	12	10	13	13	13	11	12	15	12	13	12
Ce/Yb_N	0.71	0.72	0.51	0.80	0.81	0.61	0.71	0.75	1.10	0.62	0.76	0.71
La/Sm_N	0.45	0.43	0.31	0.48	0.51	0.39	0.43	0.46	0.80	0.39	0.46	0.47

Sample ID	020805-1708	020805-1913	020905-0640	020905-0729	020905-0833	020905-0836	020905-0939	020905-1023	020905-1040	020905-1348	020905-1404	020905-1518
Study Area	A	A	A	A	A	A	A	A	A	A	A	A
Jason Transect	2	2	3	3	3	3	3	3	3	3	3	3
Morphology[1]	s	p	t	d	d	d	d	d	m	d	d	d
Lithologic Zone[2]	T	V	D	D	D	D	D	D	D	D	D	D
Depth (mbsl)	3186	3044	4172	3993	4009	4009	3903	3887	3884	3699	3676	3527
Latitude (°S)	22.878	22.876	22.884	22.883	22.883	22.883	22.883	22.883	22.883	22.882	22.882	22.881
Longitude (°W)	112.058	112.057	112.065	112.065	112.065	112.065	112.064	112.064	112.064	112.063	112.063	112.062
SiO_2 (wt%)	50.86	50.45	51.26	51.18	50.73	50.75	51.26	51.19	50.85	50.67	50.89	51.11
TiO_2	1.88	1.23	1.50	1.51	1.39	1.73	1.51	1.67	1.66	1.89	1.51	1.60
Al_2O_3	13.83	14.97	14.09	13.98	14.58	13.87	13.76	13.84	13.94	13.54	13.86	14.08
Fe_2O_3	13.26	9.95	11.71	11.83	11.03	12.63	11.66	12.92	12.50	13.34	12.92	12.08
FeO*	11.93	8.96	10.53	10.65	9.92	11.37	10.49	11.63	11.25	12.00	11.63	10.87
MnO	0.21	0.16	0.20	0.19	0.19	0.18	0.21	0.23	0.23	0.23	0.20	0.21
MgO	6.83	8.14	7.76	7.45	8.00	7.48	8.22	7.04	7.48	6.93	7.65	7.54
CaO	10.42	11.94	10.98	11.29	11.85	10.60	11.43	11.07	11.56	10.02	10.87	11.06
Na_2O	2.96	2.50	3.16	2.70	2.69	3.07	2.55	2.75	2.51	3.25	3.12	2.96
K_2O	0.06	0.11	0.06	0.06	0.05	0.05	0.06	0.06	0.05	0.06	0.06	0.04
Total	100.32	99.47	100.73	100.22	100.50	100.38	100.64	100.78	100.79	99.93	101.10	100.69
Mg#	50.5	61.8	56.8	55.5	59.0	54.0	58.3	51.9	54.2	50.7	54.0	55.3
LOI	1.7	1.4	1.2	1.1	0.1	1.0	1.9	1.7	1.8	1.3	0.9	0.5
Sr (ppm)	112	124	102	99	110	96	101	96	91	104	99	100
Ba	4.58	6.09	4.66	3.19	3.92	3.62	4.50	3.97	4.10	5.17	128.58	3.23
Zn	104	72	45	56	61	48	85	75	75	44	47	81
Cu	61	71	64	14	30	12	42	78	70	124	142	62
Ni	45	97	57	50	73	52	70	46	64	44	113	53
V	411	285	341	340	304	368	340	361	356	406	352	343
Sc	43.8	39.4	43.8	43.0	42.6	42.9	45.1	42.3	42.5	41.4	43.7	44.0
Cr	87	333	128	142	257	124	223	75	184	70	283	176
P	1791	1261	1409	338	349	1785	1028	841	972	1652	2934	958
Y	44	28	33	31	30	39	32	39	38	42	27	36
Zr	130	91	72	81	68	116	72	105	88	101	102	97
Be	0.64	0.44	0.47	0.43	0.44	0.61	0.51	0.60	0.58	0.65	1.09	0.52
Co	43.0	40.8	43.4	39.9	39.7	43.3	43.1	44.1	44.2	43.0	43.4	41.7
Rb	0.07	1.39	0.07	0.03	0.02	0.05	0.06	0.06	0.06	0.10	10.12	0.05
Nb	2.40	2.37	1.92	1.55	1.72	1.77	2.15	1.91	1.99	2.83	19.52	1.33
Cs	0.007	0.103	0.004	0.005	0.002	0.004	0.006	0.008	0.008	0.005	0.096	0.003
La	3.58	2.87	2.44	2.16	2.37	2.75	2.68	2.85	2.97	3.53	14.53	2.63
Ce	12.16	9.30	8.64	7.81	8.17	10.01	9.21	10.09	10.50	12.26	37.15	9.73
Pr	2.20	1.58	1.60	1.45	1.48	1.90	1.67	1.86	1.93	2.22	5.38	1.81
Nd	11.98	8.36	8.87	8.18	8.09	10.45	9.11	10.26	10.66	12.17	24.35	10.08
Sm	4.25	2.95	3.26	3.05	2.95	3.85	3.24	3.75	3.83	4.29	6.01	3.54
Eu	1.46	1.07	1.13	1.08	1.06	1.21	1.17	1.27	1.28	1.38	2.02	1.28
Gd	6.13	3.83	4.64	4.36	4.15	5.26	4.53	5.12	5.26	5.79	6.26	4.86
Tb	1.09	0.72	0.84	0.79	0.76	0.97	0.83	0.94	0.95	1.04	0.98	0.89
Dy	7.32	4.76	5.71	5.36	5.09	6.49	5.53	6.36	6.35	7.04	5.29	5.97
Ho	1.58	1.03	1.20	1.14	1.09	1.38	1.17	1.37	1.36	1.50	0.99	1.29
Er	4.39	2.79	3.31	3.11	2.95	3.78	3.18	3.75	3.70	4.02	2.49	3.54
Yb	4.35	2.73	3.14	3.09	2.82	3.60	3.05	3.61	3.56	3.95	1.99	3.45
Lu	0.68	0.44	0.50	0.49	0.45	0.58	0.50	0.60	0.57	0.62	0.29	0.55
Hf	3.32	2.17	1.71	1.92	1.35	1.53	1.63	2.59	2.06	2.44	4.66	2.47
Ta	0.18	0.17	0.14	0.11	0.13	0.13	0.15	0.15	0.15	0.19	1.26	0.10
Pb	0.553	0.487	0.154	0.317	0.144	0.852	0.376	0.950	0.512	0.438	2.150	0.307
Th	0.149	0.153	0.065	0.052	0.047	0.058	0.074	0.085	0.089	0.091	1.196	0.064
U	0.054	0.060		0.008	0.007	0.012	0.023	0.027	0.018	0.025	0.403	0.017
Y/Nb	18	12	17	20	17	22	15	20	19	15	1	27
Nb/Ta	13	14	14	14	13	14	14	13	13	15	16	13
Ce/Yb_N	0.78	0.95	0.76	0.70	0.80	0.77	0.84	0.78	0.82	0.86	5.18	0.78
La/Sm_N	0.54	0.63	0.48	0.46	0.52	0.46	0.53	0.49	0.50	0.53	1.56	0.48

Sample ID	021005-0532	021005-0708	021005-0731	021005-1119	021005-1202	021005-1253	021005-1317	021005-1355	021005-1411	021005-1421	021005-1432	021005-1503
Study Area	A	A	A	A	A	A	A	A	A	A	A	A
Jason Transect	4	4	4	4	4	4	4	4	4	4	4	4
Morphology[1]	d	d	m	l	m	d	l	p	s	s	p	p
Lithologic Zone[2]	D	D	D	T	T	T	V	V	V	V	V	V
Depth (mbsl)	3574	3593	3561	3385	3337	3263	3250	3190	3164	3122	3108	3088
Latitude (°S)	22.885	22.884	22.884	22.882	22.882	22.881	22.881	22.880	22.880	22.880	22.880	22.879
Longitude (°W)	112.053	112.053	112.053	112.051	112.050	112.050	112.050	112.050	112.049	112.049	112.049	112.049
SiO_2 (wt%)	50.82	50.34	51.01	51.10	50.86	51.36	51.90	51.88	50.81	50.61	52.07	50.32
TiO_2	1.40	1.28	1.33	1.48	1.58	1.60	1.42	1.33	1.53	1.12	1.35	1.27
Al_2O_3	13.99	15.11	14.20	14.14	14.16	14.25	14.62	15.04	14.96	15.79	15.31	15.21
Fe_2O_3	11.44	10.50	10.69	11.07	11.06	11.22	9.29	9.15	11.01	9.52	9.31	10.75
FeO*	10.29	9.45	9.62	9.96	9.95	10.09	8.36	8.23	9.90	8.56	8.38	9.67
MnO	0.18	0.17	0.21	0.16	0.22	0.19	0.18	0.18	0.16	0.16	0.18	0.18
MgO	8.25	8.44	8.70	7.75	7.65	7.32	7.85	7.70	6.31	8.01	7.73	7.97
CaO	10.66	11.37	11.26	11.36	11.61	11.48	12.19	12.55	11.80	12.34	12.63	12.05
Na_2O	2.75	2.54	2.49	2.68	2.72	2.65	2.71	2.70	2.90	2.60	2.72	2.58
K_2O	0.05	0.04	0.03	0.07	0.18	0.23	0.18	0.16	0.23	0.11	0.17	0.17
Total	99.53	99.78	99.92	99.82	100.05	100.32	100.36	100.69	99.70	100.26	101.49	100.50
							X	X	X	X	X	
Mg#	58.8	61.4	61.7	58.1	57.8	56.4	62.6	62.5	53.2	62.5	62.2	59.5
LOI	1.8	1.5	2.0	1.4	0.9	0.6	0.7	0.2	2.3	1.5	0.3	0.6
Sr (ppm)	89	100	94	102	134	121	123	123	110	107	116	110
Ba	2.16	2.95	2.33	3.32	11.36	13.46	19.58	14.77	4.53	3.42	13.65	3.51
Zn	39	53	67	81	81	93	86	76	84	72	88	80
Cu	34	49	68	61	69	74	63	55	73	72	57	77
Ni	58	85	69	64	68	59	80	64	102	112	63	93
V	344	286	318	337	336	353	325	293	330	269	305	298
Sc	42.9	38.2	42.5	42.1	42.0	41.7	44.1	42.8	41.5	39.5	45.0	41.7
Cr	166	311	249	226	216	173	236	265	236	338	317	370
P	1190	1189	1261	1347	1699	1548	1420	1166	1381	1023	1116	1163
Y	33	30	31	37	37	41	41	35	37	27	34	32
Zr	64	78	76	96	117	99	91	87	120	75	86	80
Be	0.43	0.39	0.48	0.47	0.53	0.53	0.51	0.49	0.51	0.36	0.41	0.45
Co	42.7	42.4	42.4	41.9	42.0	45.7	60.5	51.1	48.1	42.2	46.2	43.4
Rb				0.01	0.83	2.27	1.43	0.64	5.06	0.67	0.37	1.15
Nb	1.30	1.47	1.33	1.43	3.25	1.63	1.39	1.34	1.46	1.01	1.24	0.98
Cs		0.002	0.003	0.002	0.011	0.096	0.055	0.008	0.392	0.047	0.008	0.045
La	2.18	2.26	2.42	2.45	3.81	2.93	2.94	2.41	2.59	1.76	2.40	2.04
Ce	8.04	8.03	8.58	9.54	12.24	10.72	9.71	8.81	9.40	6.35	7.77	7.82
Pr	1.49	1.46	1.54	1.72	2.11	1.92	1.75	1.59	1.71	1.15	1.44	1.44
Nd	8.62	8.14	8.47	9.58	11.07	10.71	9.93	8.88	9.59	6.55	8.18	8.12
Sm	3.23	2.96	3.03	3.48	3.84	3.86	3.67	3.24	3.53	2.49	3.05	2.98
Eu	1.11	1.05	1.09	1.22	1.34	1.36	1.29	1.19	1.27	0.93	1.13	1.11
Gd	4.68	4.21	4.33	4.96	5.22	5.43	5.38	4.71	5.00	3.58	4.51	4.33
Tb	0.84	0.75	0.77	0.89	0.91	0.98	0.97	0.86	0.90	0.64	0.81	0.77
Dy	5.59	5.05	5.20	5.96	6.12	6.69	6.61	5.70	6.12	4.38	5.52	5.26
Ho	1.19	1.08	1.10	1.31	1.32	1.45	1.45	1.25	1.31	0.95	1.19	1.15
Er	3.21	2.93	3.03	3.64	3.67	3.98	4.13	3.45	3.72	2.62	3.36	3.17
Yb	3.18	2.94	2.95	3.59	3.63	3.94	4.12	3.49	3.72	2.65	3.34	3.15
Lu	0.51	0.46	0.47	0.58	0.59	0.63	0.65	0.54	0.60	0.41	0.54	0.49
Hf	1.73	1.95	1.83	2.61	2.96	2.86	2.77	2.42	2.80	1.85	2.38	2.28
Ta	0.10	0.11	0.10	0.11	0.23	0.13	0.12	0.10	0.12	0.08	0.10	0.08
Pb	0.028	0.084	0.359	0.182	0.417	0.301	0.346	0.374	0.323	0.142	0.483	0.283
Th	0.046	0.064	0.050	0.072	0.190	0.083	0.080	0.072	0.087	0.047	0.061	0.048
U	0.017	0.021	0.013	0.025	0.399	0.105	0.041	0.056	0.038	0.017	0.039	0.034
Y/Nb	26	21	23	26	12	25	30	26	26	26	27	33
Nb/Ta	13	13	13	12	14	13	12	13	12	12	12	12
Ce/Yb_N	0.70	0.76	0.81	0.74	0.94	0.76	0.65	0.70	0.70	0.67	0.65	0.69
La/Sm_N	0.44	0.49	0.52	0.45	0.64	0.49	0.52	0.48	0.47	0.45	0.51	0.44

Sample ID	021105-0038	021105-0150	021105-0235	021105-0256	021105-0441	021105-0520	021105-0558	021105-0616	021105-0627	021105-0639	021105-0650	021105-0714
Study Area	A	A	A	A	A	A	A	A	A	A	A	A
Jason Transect	3	3	3	3	3	3	3	3	3	3	3	3
Morphology[1]	d	d	d	d	d	s	d	p	s	p	p	p
Lithologic Zone[2]	D	T	T	T	T	T	V	V	V	V	V	V
Depth (mbsl)	3401	3342	3273	3234	3159	3199	3141	3102	3065	3057	3042	3076
Latitude (°S)	22.880	22.880	22.880	22.879	22.878	22.877	22.876	22.876	22.876	22.876	22.876	22.875
Longitude (°W)	112.062	112.061	112.061	112.061	112.061	112.062	112.062	112.062	112.062	112.062	112.062	112.062
SiO_2 (wt%)	51.32	50.20	50.71	50.93	50.50	51.06	50.55	51.14	49.77	49.97	49.81	51.33
TiO_2	1.60	1.26	2.65	1.48	1.24	1.52	1.35	1.47	1.26	1.54	1.42	1.56
Al_2O_3	14.07	14.95	13.14	14.30	15.24	14.01	14.78	14.19	15.80	15.63	15.04	14.98
Fe_2O_3	12.21	10.96	15.12	11.21	10.07	11.88	10.42	10.56	9.36	9.76	10.29	9.41
FeO*	10.98	9.86	13.60	10.09	9.06	10.69	9.38	9.50	8.42	8.78	9.26	8.47
MnO	0.19	0.18	0.22	0.19	0.17	0.19	0.17	0.20	0.16	0.17	0.17	0.18
MgO	7.29	8.34	6.91	7.90	8.34	7.48	8.13	7.72	7.84	7.56	8.65	7.86
CaO	10.74	11.22	8.71	11.03	11.93	11.41	11.74	11.64	12.54	11.97	11.22	11.82
Na_2O	2.97	2.65	2.83	2.69	2.40	2.49	2.45	2.69	2.48	2.60	2.55	2.62
K_2O	0.11	0.06	0.11	0.08	0.07	0.07	0.13	0.16	0.19	0.32	0.21	0.25
Total	100.49	99.83	100.40	99.80	99.95	100.12	99.72	99.75	99.40	99.52	99.33	100.00
										X		X
Mg#	54.2	60.1	47.5	58.3	62.1	55.5	60.7	59.1	62.4	60.5	62.5	62.3
LOI	1.3	2.0	2.2	1.6	1.3	1.1	1.5	0.6	1.2	0.8	0.6	1.6
Sr (ppm)	93	92	95	104	120	97	111	117	140	161	139	133
Ba	4.02	2.50	8.29	4.21	4.46	6.53	3.64	11.55	11.22	21.48	10.42	21.76
Zn	73	55	118	81	77	78	87	68	74	81	77	100
Cu	80	21	56	72	72	71	67	91	79	69	66	102
Ni	52	85	48	72	97	57	94	82	118	106	129	70
V	364	285	487	326	294	344	310	337	283	302	287	340
Sc	42.6	39.4	42.2	41.7	40.0	43.5	39.6	42.7	40.0	38.9	36.4	42.1
Cr	140	242	69	232	335	167	284	185	373	328	281	255
P	1462	1184	2509	1454	1283	1431	1308	1464	1464	1890	1706	1583
Y	37	29	59	34	27	36	33	36	30	35	33	42
Zr	98	78	190	82	83	101	106	97	92	114	100	106
Be	0.50	0.42	0.86	0.52	0.48	0.51	0.47	0.53	0.55	0.71	0.62	0.60
Co	45.0	45.0	43.0	43.1	41.8	43.5	42.6	49.4	41.1	40.8	44.4	48.8
Rb			0.10				0.45	0.69	1.62	2.55	1.33	1.06
Nb	1.50	1.39	3.64	2.12	2.52	1.56	1.63	2.45	3.91	5.39	3.48	2.48
Cs	0.002		0.005				0.013	0.010	0.033	0.037	0.018	0.016
La	2.60	2.19	5.14	2.90	3.03	2.69	2.63	3.15	3.83	5.19	3.72	3.70
Ce	9.63	7.75	17.67	10.11	9.43	9.06	9.19	10.30	11.36	15.00	12.25	12.13
Pr	1.77	1.38	3.10	1.76	1.59	1.66	1.64	1.80	1.82	2.38	2.00	2.09
Nd	10.03	7.80	16.93	9.67	8.47	9.21	9.02	9.88	9.37	11.88	10.46	11.26
Sm	3.69	2.94	5.95	3.52	2.91	3.40	3.24	3.39	3.05	3.84	3.55	4.03
Eu	1.26	1.00	1.89	1.19	1.05	1.22	1.18	1.22	1.11	1.31	1.22	1.36
Gd	5.26	4.06	8.19	4.86	3.91	4.83	4.51	4.97	4.26	4.93	4.72	5.60
Tb	0.92	0.71	1.46	0.87	0.69	0.86	0.79	0.88	0.73	0.87	0.83	1.00
Dy	6.23	4.84	9.83	5.76	4.50	5.90	5.38	5.95	4.85	5.73	5.47	6.83
Ho	1.35	1.03	2.12	1.23	0.98	1.30	1.19	1.29	1.06	1.24	1.19	1.48
Er	3.65	2.79	5.77	3.35	2.63	3.49	3.19	3.49	2.86	3.40	3.21	4.10
Yb	3.61	2.71	5.97	3.41	2.60	3.62	3.30	3.53	2.89	3.32	3.29	4.26
Lu	0.56	0.41	0.91	0.52	0.38	0.54	0.52	0.54	0.45	0.51	0.50	0.66
Hf	2.02	1.09	4.71	2.09	1.57	2.50	2.53	2.22	2.37	2.96	2.74	2.85
Ta	0.11	0.11	0.25	0.15	0.18	0.12	0.13	0.17	0.26	0.34	0.23	0.18
Pb	4.171	0.186	0.587	0.474	0.078	0.218	0.307	0.200	0.351	0.539	0.476	0.342
Th	0.056	0.039	0.219	0.088	0.086	0.080	0.080	0.119	0.225	0.331	0.203	0.135
U	0.106	0.008	0.078	0.035	0.041	0.086	0.051	0.047	0.238	0.178	0.100	0.100
Y/Nb	24	21	16	16	11	23	20	15	8	6	10	17
Nb/Ta	13	13	14	14	14	13	13	14	15	16	15	14
Ce/Yb_N	0.74	0.80	0.82	0.82	1.01	0.70	0.77	0.81	1.09	1.26	1.04	0.79
La/Sm_N	0.45	0.48	0.56	0.53	0.67	0.51	0.52	0.60	0.81	0.87	0.67	0.59

Sample ID	021705-1929	021705-2035	021705-2353	021805-0008	021805-0417	021805-0513	021805-0556	021805-0706	021805-1355	021905-0132	021905-0148	021905-0226
Study Area	B	B	B	B	B	B	B	B	B	B	B	B
Jason Transect	1	1	1	1	1	1	1	1	1	2	2	2
Morphology[1]	d	d	m	d	d	d	d	l	t	t	t	d
Lithologic Zone[2]	GDT	GDT	GDT	GDT	GDT	D	T	T			GDT	D
Depth (mbsl)	4231	4210	4139	4134	3376	3303	3129	3079	4410	3498	3887	3780
Latitude (°S)	22.939	22.939	22.939	22.939	22.937	22.937	22.937	22.937	22.943	22.947	22.946	22.947
Longitude (°W)	111.910	111.909	111.908	111.909	111.902	111.901	111.900	111.898	111.915	111.902	111.901	111.901
SiO_2 (wt%)	49.70	50.22	50.66	51.30	50.44	51.18	49.98	50.14	50.19	50.75	50.73	50.78
TiO_2	2.91	2.76	1.81	1.99	2.08	2.05	1.98	1.68	2.59	1.41	1.27	2.19
Al_2O_3	13.77	13.53	14.25	13.50	13.60	13.61	13.74	14.29	13.14	14.49	14.45	13.05
Fe_2O_3	15.49	14.63	13.03	13.93	13.48	13.12	12.89	11.96	15.16	11.15	10.31	14.59
FeO*	13.94	13.17	11.73	12.53	12.13	11.80	11.60	10.76	13.64	10.03	9.27	13.13
MnO	0.24	0.25	0.22	0.21	0.23	0.21	0.20	0.19	0.24	0.22	0.21	0.27
MgO	5.76	6.42	6.94	6.51	6.90	6.85	6.96	7.17	6.33	7.84	7.89	6.54
CaO	9.93	10.53	10.92	10.55	10.52	10.13	10.80	11.26	10.27	11.85	12.23	9.53
Na_2O	2.96	2.90	2.92	2.82	2.97	2.77	2.56	2.70	2.78	2.19	2.36	2.57
K_2O	0.10	0.07	0.08	0.09	0.05	0.03	0.05	0.05	0.06	0.06	0.05	0.04
Total	100.86	101.32	100.84	100.90	100.27	99.95	99.16	99.45	100.76	99.96	99.49	99.57
Mg#	42.4	46.5	51.3	48.1	50.3	50.9	51.7	54.3	45.2	58.2	60.3	47.0
LOI	0.3	0.4	0.5	0.4	1.5	1.7	1.5	1.4	1.0	0.5	0.3	1.5
Sr (ppm)	100	97	105	93	96	86	88	95	92	81	87	79
Ba	5.33	4.43	4.80	4.55	4.32	4.23	6.13	3.75	4.86	4.60	1.34	3.25
Zn	119	106	93	111	145	101	91	93	91	79	64	102
Cu	55	60	70	71	66	60	67	65	69	77	38	55
Ni	37	50	55	43	52	58	61	64	46	76	69	57
V	490	427	351	401	407	383	371	373	477	311	304	395
Sc	41.5	41.5	41.2	42.7	43.5	41.4	42.0	45.3	46.1	42.0	43.5	39.3
Cr	38	77	79	46	91	142	165	171	63	299	226	91
P	2005	2002	1516	1559	1920	1991	1834	1412	2326	1171	970	1985
Y	49	48	41	46	42	49	45	39	55	34	30	50
Zr	110	93	118	123	101	129	110	106	120	70	71	111
Be	0.62	0.60	0.62	0.50	0.63	0.65	0.63	0.54	0.83	0.43	0.35	0.56
Co	43.4	43.4	45.6	48.4	43.1	41.5	41.1	41.6	43.2	38.7	30.3	44.5
Rb	0.34	0.19	0.23	0.16	0.18	0.03	0.08	0.08	0.14	0.08	0.02	0.13
Nb	2.46	2.60	1.93	1.72	2.38	2.62	2.38	1.84	3.14	1.24	1.04	2.05
Cs	0.006	0.008	0.006	0.004	0.014	0.002	0.004	0.004	0.009	0.004	0.002	0.010
La	3.48	3.49	3.13	2.85	3.66	3.91	3.68	2.88	4.60	2.16	1.46	3.71
Ce	12.48	12.25	10.98	10.44	12.64	13.50	12.61	10.11	16.08	7.98	6.20	12.78
Pr	2.35	2.29	2.00	2.02	2.31	2.49	2.33	1.89	2.99	1.52	1.22	2.43
Nd	13.16	12.79	11.04	11.70	12.68	13.73	12.80	10.34	16.41	8.61	7.13	13.41
Sm	4.71	4.52	3.86	4.23	4.39	4.78	4.55	3.73	5.65	3.12	2.75	4.89
Eu	1.70	1.59	1.38	1.48	1.43	1.60	1.52	1.29	1.81	1.16	0.97	1.66
Gd	6.97	6.71	5.69	6.43	5.89	6.93	6.58	5.46	8.19	4.78	3.97	7.22
Tb	1.24	1.20	1.01	1.14	1.04	1.26	1.17	0.99	1.47	0.89	0.71	1.29
Dy	8.29	7.98	6.69	7.61	7.25	8.25	7.76	6.62	9.50	5.84	4.98	8.45
Ho	1.78	1.71	1.47	1.65	1.53	1.80	1.67	1.44	2.00	1.25	1.09	1.85
Er	4.83	4.72	4.05	4.54	3.87	4.89	4.51	3.95	5.36	3.45	2.85	5.03
Yb	4.87	4.62	3.95	4.39	4.00	4.74	4.39	3.99	5.09	3.24	2.75	5.08
Lu	0.74	0.71	0.61	0.67	0.64	0.74	0.67	0.61	0.78	0.49	0.40	0.74
Hf	1.15	0.90	0.93	0.59	2.09	3.30	2.86	2.84	2.21	1.71	1.23	3.19
Ta	0.18	0.19	0.14	0.13	0.19	0.19	0.17	0.13	0.22	0.10	0.09	0.16
Pb	0.648	0.164	0.331	0.904	0.783	0.413	0.689	0.186	0.247	0.177	0.054	0.349
Th	0.076	0.080	0.096	0.071	0.075	0.124	0.114	0.106	0.100	0.051	0.039	0.103
U	0.022	0.021	0.028	0.019	0.047	0.054	0.065	0.059	0.041	0.025	0.021	0.057
Y/Nb	20	18	21	26	18	19	19	21	17	27	28	25
Nb/Ta	13	13	14	13	13	14	14	14	14	13	11	13
Ce/Yb_N	0.71	0.74	0.77	0.66	0.88	0.79	0.80	0.70	0.88	0.68	0.63	0.70
La/Sm_N	0.48	0.50	0.52	0.43	0.54	0.53	0.52	0.50	0.53	0.45	0.34	0.49

Sample ID	021905-0409	021905-0428	022105-0059	022105-0244	022105-0250	022105-0412	022105-0647	022105-0720	022105-0836	022205-0320	022205-0333	022205-0335
Study Area	B	B	B	B	B	B	B	B	B	B	B	B
Jason Transect	2	2	3	3	3	3	3	3	3	4	4	4
Morphology[1]	d	d	t	d	d	d	p	p	p	d	d	d
Lithologic Zone[2]	D	D	D	D	D	D	T	T	V	D	D	D
Depth (mbsl)	3518	3435	3263	3127	3127	3037	2764	2752	2627	3897	3884	3884
Latitude (°S)	22.947	22.947	22.969	22.968	22.968	22.967	22.964	22.964	22.964	22.983	22.983	22.983
Longitude (°W)	111.898	111.898	111.888	111.884	111.884	111.884	111.880	111.880	111.877	111.890	111.890	111.890
SiO_2 (wt%)	50.28	51.14	50.68	50.81	50.37	50.35	52.79	51.44	50.67	50.34	50.76	50.16
TiO_2	1.90	1.99	1.80	2.23	1.79	2.29	2.20	1.98	1.33	1.68	1.43	1.34
Al_2O_3	13.26	13.14	14.05	12.90	13.56	13.13	13.95	13.52	14.33	13.68	14.24	14.76
Fe_2O_3	13.98	14.24	12.59	14.43	13.34	14.86	10.77	13.55	11.23	12.21	11.22	10.88
FeO*	12.58	12.81	11.33	12.98	12.00	13.37	9.69	12.19	10.10	10.98	10.09	9.79
MnO	0.20	0.25	0.22	0.26	0.31	0.28	0.21	0.20	0.19	0.21	0.18	0.17
MgO	6.79	6.55	7.97	6.94	8.11	6.73	6.65	7.12	8.04	7.45	8.28	7.92
CaO	10.33	10.58	10.69	8.85	9.84	9.94	11.03	10.19	11.69	11.34	12.01	11.69
Na_2O	2.93	2.70	2.57	2.81	2.46	2.68	2.77	2.87	2.61	2.48	2.47	2.54
K_2O	0.05	0.04	0.08	0.03	0.04	0.04	0.31	0.09	0.07	0.04	0.06	0.07
Total	99.72	100.63	100.65	99.25	99.83	100.30	100.69	100.96	100.16	99.44	100.65	99.53
							X					
Mg#	49.0	47.7	55.7	48.8	54.6	47.3	55.0	51.0	58.6	54.7	59.4	59.0
LOI	0.8	1.3	1.8	1.9	1.7	1.8	0.9	0.9	0.4	1.0	1.3	1.1
Sr (ppm)	96	89	86	75	74	86	133	95	100	99	90	89
Ba	3.03	2.97	3.33	3.74	2.54	3.71	25.94	5.98	4.51	3.61	2.59	2.20
Zn	84	105	66	103	114	118	141	100	80	64	59	46
Cu	78	58	76	50	60	54	106	61	62	55	89	50
Ni	41	37	64	45	46	44	59	50	71	73	95	93
V	375	416	374	412	402	467	432	460	291	377	339	218
Sc	41.6	43.8	42.6	40.1	43.3	45.8	42.5	46.5	40.9	44.1	43.1	33.3
Cr	51	46	159	77	52	65	128	119	187	188	339	313
P	1599	1678	1589	2092	1537	1985	2026	1680	1178	1535	1213	1166
Y	43	43	42	50	38	49	58	46	33	36	31	30
Zr	78	97	102	117	68	128	142	148	85	85	73	81
Be	0.60	0.61	0.51	0.71	0.59	0.65	0.65	0.59	0.39	0.59	0.47	0.43
Co	45.5	40.6	40.4	41.6	44.3	42.9	54.6	41.6	43.3	42.4	41.7	41.5
Rb	0.06	0.00	0.16	0.04	0.04	0.05	1.51	0.34	0.44	0.01	0.10	0.03
Nb	1.71	1.76	1.82	2.58	1.76	2.53	2.50	2.02	1.44	2.05	1.36	1.24
Cs	0.001	0.000	0.010	0.005	0.003	0.004	0.023	0.005	0.005	0.000	0.004	
La	2.71	3.00	2.91	3.91	3.21	3.84	4.31	3.27	2.30	3.19	2.46	2.34
Ce	10.00	10.83	10.17	13.71	11.01	13.22	14.54	11.39	7.94	10.67	8.42	8.11
Pr	1.91	2.07	1.93	2.54	2.03	2.45	2.61	2.12	1.50	1.96	1.59	1.52
Nd	11.04	11.55	10.87	14.17	11.19	13.46	14.60	11.77	8.30	10.78	8.72	8.39
Sm	4.08	4.24	4.03	5.01	4.04	4.95	5.19	4.32	3.02	3.71	3.13	2.98
Eu	1.47	1.46	1.32	1.61	1.31	1.66	1.67	1.50	1.11	1.23	1.06	1.06
Gd	6.18	6.34	6.02	7.32	5.86	7.24	6.87	6.44	4.57	5.51	4.63	4.43
Tb	1.10	1.10	1.07	1.27	1.03	1.25	1.25	1.14	0.80	0.96	0.82	0.79
Dy	7.28	7.25	7.06	8.48	6.81	8.56	9.39	7.72	5.54	6.45	5.41	5.20
Ho	1.58	1.58	1.55	1.83	1.46	1.83	2.04	1.67	1.22	1.34	1.15	1.07
Er	4.24	4.32	4.27	5.03	3.85	4.98	5.24	4.73	3.32	3.64	3.20	3.05
Yb	4.12	4.27	4.23	4.84	3.78	4.75	5.71	4.72	3.34	3.55	3.20	3.05
Lu	0.60	0.63	0.64	0.73	0.57	0.69	0.89	0.71	0.49	0.55	0.48	0.46
Hf	1.72	2.16	2.94	3.38	1.60	3.11	3.84	3.37	2.32	1.85	1.51	1.46
Ta	0.13	0.14	0.14	0.19	0.13	0.18	0.19	0.15	0.11	0.16	0.10	0.10
Pb	0.081	0.169	0.341	0.324	0.180	0.257	0.430	0.350	0.285	0.133	0.098	0.083
Th	0.058	0.085	0.096	0.142	0.047	0.118	0.147	0.118	0.081	0.059	0.039	0.035
U	0.024	0.031	0.059	0.035	0.017	0.045	0.055	0.044	0.031	0.142	0.043	0.036
Y/Nb	25	25	23	19	22	19	23	23	23	18	23	24
Nb/Ta	13	13	13	13	14	14	13	14	13	13	13	12
Ce/Yb_N	0.67	0.70	0.67	0.79	0.81	0.77	0.71	0.67	0.66	0.69	0.73	0.74
La/Sm_N	0.43	0.46	0.47	0.50	0.51	0.50	0.54	0.49	0.49	0.56	0.51	0.51

Sample ID	022205-0852	022205-0933	022205-0941	022205-1105	022205-1118	022205-1200	022205-1220	022205-1318	022205-1404	022205-2003	022205-2213	022205-2353
Study Area	B	B	B	B	B	B	B	B	B	B	B	B
Jason Transect	4	4	4	4	4	4	4	4	4	5	5	5
Morphology[1]	d	d	d	d	d	d	d	l	p	t	d	d
Lithologic Zone[2]	D	D	D	D	D	D	D	V	V	D	D	D
Depth (mbsl)	3197	3147	3142	3015	2985	2930	2878	2729	2630	3496	3170	3111
Latitude (°S)	22.974	22.974	22.974	22.973	22.973	22.972	22.972	22.971	22.968	22.980	22.976	22.976
Longitude (°W)	111.880	111.880	111.880	111.879	111.879	111.878	111.878	111.877	111.875	111.879	111.877	111.877
SiO_2 (wt%)	51.36	50.50	51.32	51.19	51.20	50.98	50.90	51.11	51.16	50.03	50.21	50.38
TiO_2	1.32	1.33	2.05	1.74	1.68	1.73	1.85	1.69	1.79	1.80	1.92	1.58
Al_2O_3	14.00	13.93	13.39	13.51	13.55	13.80	13.78	14.24	14.11	13.53	13.57	13.62
Fe_2O_3	11.37	11.21	13.76	13.14	12.62	12.40	13.35	11.85	11.10	12.67	13.60	12.14
FeO*	10.23	10.09	12.38	11.82	11.35	11.16	12.02	10.66	9.99	11.40	12.23	10.93
MnO	0.20	0.19	0.25	0.21	0.21	0.26	0.25	0.19	0.20	0.23	0.23	0.20
MgO	8.01	7.88	6.89	7.20	7.36	7.71	8.15	6.81	6.99	7.11	7.14	7.61
CaO	11.98	11.41	10.64	10.90	10.94	11.14	9.36	11.68	11.33	10.74	10.50	10.75
Na_2O	2.52	2.52	2.64	2.44	2.50	2.61	2.66	2.67	2.68	2.93	2.70	2.98
K_2O	0.04	0.06	0.05	0.05	0.05	0.05	0.05	0.16	0.28	0.06	0.04	0.06
Total	100.79	99.03	100.99	100.38	100.12	100.66	100.35	100.39	99.64	99.11	99.91	99.32
								X	X			
Mg#	58.2	58.2	49.8	52.0	53.6	55.2	54.7	53.2	55.5	52.6	51.0	55.4
LOI	1.0	1.4	1.2	1.3	1.3	1.3	1.7	0.6	0.6	1.4	1.4	1.0
Sr (ppm)	90	81	81	79	88	94	86	107	115	93	84	89
Ba	4.03	4.04	3.33	2.95	2.98	3.61	2.90	3.89	17.78	3.58	2.47	2.30
Zn	55	48	64	80	77	75	111	98	107	76	104	48
Cu	61	84	57	57	59	59	65	62	81	57	64	95
Ni	66	67	50	55	76	60	49	103	57	54	61	63
V	324	329	399	353	361	370	403	395	387	362	397	340
Sc	43.2	42.5	42.5	41.3	41.8	43.2	44.8	46.7	45.0	42.6	43.3	42.4
Cr	188	174	102	118	147	148	90	186	129	108	127	188
P	1101	1154	1875	1507	1479	1517	1694	1559	1517	1764	1924	1354
Y	29	29	45	40	39	36	39	37	43	38	45	34
Zr	70	59	111	81	88	98	90	110	115	98	120	63
Be	0.44	0.41	0.63	0.52	0.54	0.52	0.67	0.52	0.53	0.62	0.63	0.47
Co	42.3	42.9	44.0	41.4	40.4	38.4	37.2	47.3	44.3	40.9	43.5	41.7
Rb	0.04	0.02		0.03	0.01			0.61	2.38			
Nb	1.78	1.85	2.20	1.69	1.77	2.34	2.08	1.57	1.72	1.92	1.87	1.47
Cs	0.001	0.003	0.004	0.001	0.003		0.003	0.044	0.120	0.000	0.000	
La	2.44	2.47	3.46	2.86	2.84	3.04	3.07	2.69	3.05	3.14	3.36	2.39
Ce	7.80	7.91	12.05	10.02	9.80	10.11	10.85	9.63	10.68	11.27	12.19	8.76
Pr	1.41	1.44	2.30	1.88	1.83	1.76	1.92	1.70	1.92	2.02	2.21	1.59
Nd	7.80	7.84	12.63	10.56	10.17	9.89	10.93	9.59	10.77	11.27	12.50	9.21
Sm	2.85	2.87	4.57	3.89	3.76	3.66	4.12	3.59	4.04	4.05	4.79	3.54
Eu	1.05	1.02	1.46	1.30	1.27	1.15	1.18	1.17	1.28	1.24	1.41	1.13
Gd	4.25	4.23	6.74	5.78	5.53	5.04	5.66	5.06	5.91	5.75	6.59	4.75
Tb	0.75	0.75	1.16	1.00	0.98	0.85	0.92	0.87	0.98	0.94	1.06	0.81
Dy	5.14	5.04	7.83	6.82	6.58	6.18	6.81	6.32	7.26	6.71	8.07	5.79
Ho	1.05	1.07	1.64	1.46	1.43	1.36	1.44	1.36	1.53	1.34	1.71	1.22
Er	2.91	2.89	4.55	3.96	3.98	3.51	3.88	3.72	4.26	3.65	4.50	3.31
Yb	2.95	2.87	4.59	3.97	3.92	3.48	3.77	3.66	4.37	3.61	4.63	3.21
Lu	0.45	0.44	0.70	0.59	0.59	0.58	0.60	0.60	0.67	0.58	0.72	0.51
Hf	1.42	1.30	2.91	1.89	2.50	2.58	1.88	2.80	2.96	2.47	3.02	1.21
Ta	0.13	0.14	0.16	0.13	0.13	0.17	0.16	0.13	0.14	0.15	0.15	0.12
Pb	0.074	0.103	0.135	0.132	0.177	0.328	0.137	0.382	0.379	0.228	0.428	0.152
Th	0.073	0.072	0.092	0.063	0.087	0.147	0.094	0.109	0.119	0.076	0.104	0.042
U	0.031	0.019	0.031	0.020	0.027	0.031		0.365				0.019
Y/Nb	16	16	21	23	22	16	19	23	25	20	24	23
Nb/Ta	14	14	13	13	13	14	13	12	12	13	13	13
Ce/Yb_N	0.73	0.77	0.73	0.70	0.69	0.81	0.80	0.73	0.68	0.87	0.73	0.76
La/Sm_N	0.55	0.56	0.49	0.47	0.49	0.54	0.48	0.48	0.49	0.50	0.45	0.44

Sample ID	022305-0019	022305-0306	022305-0310	022305-0316	022305-0320	022305-0323	022305-0336	022305-0343	022305-0351	022305-0357	022305-0418	022305-0422
Study Area	B	B	B	B	B	B	B	B	B	B	B	B
Jason Transect	5	5	5	5	5	5	5	5	5	5	5	5
Morphology[1]	d	d	d	d	d	d	d	d	d	d	d	d
Lithologic Zone[2]	D	D	D	D	D	D	D	D	D	D	D	D
Depth (mbsl)	3076	2989	2989	2989	2989	2989	2988	2988	2987	2985	2983	2982
Latitude (°S)	22.975	22.974	22.974	22.974	22.974	22.974	22.974	22.974	22.974	22.974	22.974	22.975
Longitude (°W)	111.877	111.876	111.877	111.876	111.876	111.876	111.876	111.876	111.876	111.876	111.876	111.876
SiO_2 (wt%)	49.98	50.34	49.92	50.26	50.24	50.29	50.84	50.05	51.26	50.97	50.45	50.46
TiO_2	1.65	1.93	1.90	1.65	1.69	1.71	1.88	1.64	1.66	2.03	1.50	1.64
Al_2O_3	13.71	13.46	13.26	13.98	13.86	13.54	13.54	13.97	13.77	13.27	14.41	13.68
Fe_2O_3	12.18	14.14	14.36	12.17	12.41	12.39	13.38	12.12	12.52	14.72	11.47	12.08
FeO*	10.96	12.72	12.92	10.95	11.17	11.15	12.04	10.91	11.26	13.24	10.32	10.87
MnO	0.24	0.24	0.24	0.22	0.22	0.21	0.23	0.21	0.21	0.24	0.30	0.23
MgO	7.75	6.94	7.14	7.47	7.55	7.39	6.99	7.57	7.44	6.79	7.96	7.60
CaO	10.61	10.18	10.42	10.86	10.99	10.95	10.22	10.91	10.38	10.11	11.12	10.93
Na_2O	2.63	2.73	2.62	2.70	2.77	2.81	3.42	2.77	2.93	2.74	2.78	2.68
K_2O	0.06	0.12	0.03	0.08	0.06	0.08	0.10	0.09	0.12	0.05	0.09	0.08
Total	98.82	100.08	99.89	99.38	99.77	99.38	100.60	99.33	100.29	100.91	100.07	99.38
Mg#	55.8	49.3	49.6	54.9	54.6	54.1	50.8	55.3	54.1	47.8	57.9	55.5
LOI	1.1	1.3	1.4	1.2	1.2	1.1	0.9	0.7	1.3	1.7	1.2	0.9
Sr (ppm)	86	84	82	97	93	89	96	97	91	80	95	91
Ba	2.86	2.70	1.46	3.20	3.79	4.64	3.70	4.90	5.43	1.57	4.33	3.38
Zn	60	108	104	84	59	66	48	86	75	103	52	92
Cu	59	68	61	65	74	57	59	62	60	62	73	49
Ni	62	49	46	72	76	66	58	77	56	42	75	64
V	351	381	393	362	364	373	393	361	378	403	315	337
Sc	41.4	39.9	41.4	41.8	41.7	44.5	43.7	42.4	45.7	44.2	42.6	42.7
Cr	172	33	30	194	210	153	185	214	113	31	300	165
P	1446		1562	1372	1660		1585	1503	1464	1856	1411	1429
Y	34	45	41	31	38	37	42	35	33	44	34	35
Zr	77	113	109	76	88	65	106	78	83	110	66	80
Be	0.46	0.61	0.55	0.47	0.54	0.48	0.58	0.51	0.50	0.61	0.47	0.49
Co	38.4	45.0	43.2	40.4	42.2	44.5	40.4	41.0	40.8	44.9	40.7	38.7
Rb						0.08		0.03				
Nb	1.53	1.74	1.59	1.80	2.06	1.84	1.85	1.94	1.61	1.71	1.86	1.61
Cs	0.000	0.004	0.000					0.004		0.005	0.004	0.000
La	2.54	3.15	2.84	2.47	3.19	3.04	3.07	3.24	2.64	3.17	2.58	2.61
Ce	9.18	11.46	10.35	8.78	10.77	10.43	11.13	10.66	9.53	11.73	9.08	9.60
Pr	1.64	2.13	1.90	1.56	1.93	2.07	2.04	1.89	1.73	2.15	1.59	1.73
Nd	9.34	11.75	10.72	8.82	10.40	10.98	11.49	10.40	9.98	12.08	9.02	9.72
Sm	3.47	4.34	4.00	3.21	3.76	4.01	4.33	3.62	3.70	4.71	3.27	3.74
Eu	1.08	1.39	1.31	1.05	1.23	1.26	1.29	1.17	1.20	1.45	1.07	1.14
Gd	4.86	5.75	5.74	4.29	5.17	5.27	5.82	5.08	4.97	6.42	4.50	4.94
Tb	0.79	0.98	0.94	0.72	0.87	0.96	1.00	0.88	0.88	1.06	0.77	0.85
Dy	5.81	7.73	6.98	5.17	6.35	6.52	7.00	5.87	5.74	7.50	5.40	5.99
Ho	1.23	1.64	1.53	1.13	1.39	1.39	1.55	1.27	1.21	1.60	1.17	1.26
Er	3.28	4.18	4.08	2.89	3.69	3.67	4.04	3.36	3.21	4.21	3.14	3.24
Yb	3.21	4.66	4.20	2.94	3.63	3.70	4.11	3.28	3.13	4.18	3.00	3.13
Lu	0.51	0.75	0.68	0.47	0.58	0.56	0.63	0.52	0.50	0.64	0.48	0.50
Hf	1.78	3.34	2.93	1.47	2.11	2.27	2.52	1.76	1.90	2.69	1.35	1.81
Ta	0.12	0.15	0.13	0.14	0.15	0.14	0.14	0.16	0.14	0.15	0.15	0.13
Pb	0.239	0.518	0.408	0.720	0.353	0.160	0.290	0.148	0.257	0.396	0.294	0.184
Th	0.063	0.106	0.084	0.054	0.068	0.051	0.082	0.049	0.040	0.069	0.068	0.038
U	0.010	0.040	0.024	0.013	0.011	0.019	0.025	0.007	0.018	0.024	0.011	
Y/Nb	22	26	26	17	18	20	23	18	20	26	18	22
Nb/Ta	13	11	12	13	13	13	13	12	11	12	13	12
Ce/Yb_N	0.79	0.68	0.69	0.83	0.83	0.78	0.75	0.90	0.85	0.78	0.84	0.85
La/Sm_N	0.47	0.47	0.46	0.50	0.55	0.49	0.46	0.58	0.46	0.43	0.51	0.45

Sample ID	022305-0428	022305-0434	022305-0440	022305-0452	022305-0456	022305-0509	022305-0617	022305-0636	022305-0756	022305-0837	022305-0904	4075-1752
Study Area	B	B	B	B	B	B	B	B	B	B	B	A
Jason Transect	5	5	5	5	5	5	5	5	5	5	5	
Morphology[1]	d	d	d	d	d	d	p	p	p	p	p	m
Lithologic Zone[2]	D	D	D	D	D	D	D	T	V	V	V	D
Depth (mbsl)	2982	2981	2979	2977	2978	2979	2891	2829	2696	2653	2633	3956
Latitude (°S)	22.974	22.974	22.974	22.974	22.974	22.974	22.973	22.973	22.971	22.969	22.969	22.880
Longitude (°W)	111.876	111.876	111.876	111.876	111.876	111.876	111.875	111.875	111.875	111.875	111.876	112.069
SiO_2 (wt%)	50.44	49.85	51.07	50.58	50.66	50.49	50.51	50.81	50.47	51.67	52.14	50.79
TiO_2	1.71	2.58	1.68	1.65	1.68	1.67	1.82	1.83	1.49	1.58	1.85	2.50
Al_2O_3	13.52	12.34	14.05	13.62	13.79	13.75	13.53	13.81	14.65	14.56	14.09	12.91
Fe_2O_3	12.78	15.92	12.39	12.17	12.31	12.21	13.66	13.51	11.72	9.47	10.76	14.35
FeO*	11.50	14.33	11.14	10.95	11.07	10.98	12.29	12.15	10.54	8.52	9.68	12.91
MnO	0.20	0.27	0.25	0.22	0.23	0.21	0.22	0.22	0.19	0.18	0.22	0.23
MgO	7.34	6.51	7.77	7.84	7.84	7.78	7.26	7.25	7.44	7.69	6.99	6.48
CaO	9.97	9.64	10.59	10.75	10.48	10.83	10.50	10.48	11.44	12.10	11.44	9.46
Na_2O	2.87	2.64	2.88	2.74	2.72	2.69	2.77	2.86	2.62	2.59	2.75	3.49
K_2O	0.11	0.08	0.08	0.07	0.06	0.11	0.07	0.09	0.23	0.20	0.19	0.12
Total	98.95	99.83	100.76	99.64	99.76	99.74	100.35	100.85	100.25	100.04	100.43	100.32
										X	X	
Mg#	53.2	44.7	55.4	56.1	55.8	55.8	51.3	51.5	55.7	61.7	56.3	47.2
LOI	1.4	1.1	1.4	1.5	1.5	1.0	0.6	0.9	1.0	0.6	0.5	1.5
Sr (ppm)	89	81	89	86	84	89	93	95	103	118	113	109
Ba	2.91	1.84	3.32	2.97	3.09	3.74	1.33	1.66	3.72	24.17	10.58	5.79
Zn	83	108	65	75	60	65	105	104	81	97	110	78
Cu	68	54	70	60	75	64	68	67	71	70	81	16
Ni	55	39	70	67	68	69	48	47	85	69	84	41
V	363	488	345	365	368	355	370	382	347	343	393	365
Sc	42.3	44.5	41.5	44.3	42.5	43.0	43.2	42.6	44.6	43.5	43.4	35.0
Cr	112	58	184	170	170	181	53	54	252	241	120	73
P	1519	2245										2572
Y	39	58	39	35	38	34	42	41	36	43	50	52
Zr	104	170	90	84	94	82	117	116	98	100	121	129
Be	0.54	0.76	0.56	0.50	0.53	0.51	0.48	0.50	0.44	0.53	0.50	0.84
Co	40.0	41.7	42.6	41.8	42.4	42.7	43.1	42.6	42.3	45.7	57.3	40.5
Rb									1.27	1.07	0.57	
Nb	1.69	2.21	1.73	1.62	1.68	1.65	1.32	1.32	1.38	1.83	1.76	3.53
Cs	0.002	0.001			0.007				0.028	0.038	0.012	0.006
La	2.82	4.24	2.90	2.52	2.80	2.80	2.73	2.71	2.50	3.05	3.12	5.17
Ce	10.30	15.20	10.22	9.28	9.92	9.78	10.11	10.05	8.92	10.30	11.30	17.69
Pr	1.87	2.76	1.86	1.69	1.81	1.77	1.87	1.90	1.59	1.84	2.10	3.18
Nd	10.55	15.19	10.21	9.29	10.11	10.08	10.52	10.53	8.93	10.30	11.78	17.19
Sm	3.88	5.71	3.88	3.55	3.59	3.60	3.93	3.93	3.28	3.67	4.38	5.93
Eu	1.24	1.66	1.15	1.07	1.13	1.15	1.23	1.19	1.05	1.20	1.37	1.81
Gd	5.33	7.91	5.20	4.78	4.79	4.77	5.46	5.42	4.04	5.11	5.31	7.94
Tb	0.90	1.32	0.85	0.76	0.80	0.79	0.88	0.85	0.71	0.89	0.94	1.39
Dy	6.53	9.66	6.28	5.88	6.31	5.83	7.03	6.99	5.80	6.74	8.05	9.11
Ho	1.41	2.06	1.38	1.28	1.36	1.29	1.56	1.56	1.27	1.55	1.73	1.90
Er	3.72	5.62	3.57	3.34	3.35	3.19	4.00	3.97	3.07	3.80	4.05	5.11
Yb	3.70	5.65	3.74	3.33	3.87	3.24	4.17	4.05	3.83	3.98	5.05	4.84
Lu	0.58	0.89	0.57	0.54	0.59	0.51	0.65	0.64	0.60	0.61	0.79	0.76
Hf	2.49	4.32	2.28	1.96	2.35	1.75	2.96	2.97	2.58	2.56	3.30	2.40
Ta	0.13	0.18	0.15	0.14	0.14	0.14	0.12	0.12	0.13	0.15	0.18	0.25
Pb	0.258	0.714	0.195	0.348	0.238	0.011	0.355	0.518	0.441	0.341	0.454	0.475
Th	0.072	0.109	0.083	0.065	0.077	0.043	0.066	0.078	0.091	0.118	0.100	0.097
U	0.023	0.037	0.021	0.010	0.027	0.021	0.041	0.034	0.039	0.097	0.042	0.017
Y/Nb	23	26	22	22	23	21	32	31	26	24	29	15
Nb/Ta	13	12	12	12	12	12	11	11	11	12	10	14
Ce/Yb_N	0.77	0.75	0.76	0.77	0.71	0.84	0.67	0.69	0.65	0.72	0.62	1.02
La/Sm_N	0.47	0.48	0.48	0.46	0.50	0.50	0.45	0.44	0.49	0.54	0.46	0.56

Sample ID	4075-1810	4075-1832	4075-1912	4075-1937	4075-2004	4075-2014	4075-2058	4076-1725	4076-1740	4076-1756	4076-1854	4076-2001
Study Area	A	A	A	A	A	A	A	A	A	A	A	A
Jason Transect												
Morphology[1]	m	d	m	d	d	m	m	d	d	d	d	d
Lithologic Zone[2]	D	D	D	D	D	D	D	D	D	D	D	D
Depth (mbsl)	3923	3899	3826	3801	3789	3772	3622	3580	3575	3557	3445	3452
Latitude (°S)	22.880	22.880	22.879	22.879	22.879	22.879	22.879	22.883	22.883	22.883	22.882	22.882
Longitude (°W)	112.068	112.068	112.068	112.068	112.068	112.068	112.067	112.061	112.061	112.061	112.060	112.058
SiO_2 (wt%)	50.94	50.94	50.43	50.34	50.77	50.79	50.83	50.71	50.68	50.97	50.17	51.06
TiO_2	1.55	1.61	1.17	2.55	2.65	2.16	2.53	1.52	1.19	1.19	1.37	1.36
Al_2O_3	13.98	14.24	15.21	12.83	12.59	13.49	12.93	14.04	14.79	15.14	14.75	14.33
Fe_2O_3	11.93	11.15	9.34	15.22	15.39	13.44	14.97	11.55	10.15	10.13	11.16	11.01
FeO*	10.73	10.04	8.41	13.69	13.84	12.09	13.47	10.39	9.14	9.11	10.04	9.91
MnO	0.22	0.17	0.17	0.25	0.28	0.23	0.26	0.16	0.19	0.18	0.22	0.18
MgO	7.63	7.68	8.28	6.47	6.04	6.79	6.27	8.09	8.68	8.46	8.48	8.28
CaO	11.24	10.56	11.76	9.54	9.35	10.23	9.54	11.68	11.89	12.01	11.72	11.76
Na_2O	2.59	3.41	2.72	3.20	3.27	3.26	3.12	2.91	2.42	2.60	2.65	2.57
K_2O	0.13	0.07	0.09	0.07	0.08	0.10	0.09	0.04	0.06	0.04	0.07	0.04
Total	100.20	99.83	99.17	100.46	100.41	100.50	100.55	100.70	100.05	100.71	100.60	100.60
			X									
Mg#	55.9	57.7	63.7	45.7	43.7	50.0	45.3	58.1	62.9	62.3	60.1	59.8
LOI	1.5	1.9	1.0	1.5	1.0	1.5	2.1	2.3	1.2	0.7	2.0	0.4
Sr (ppm)	97	103	151	91	97	104	95	95	96	99	84	97
Ba	4.91	2.86	14.62	5.43	7.26	8.87	7.02	2.97	2.14	2.49	3.24	3.97
Zn	60	40	57	66	60	56	94	31	74	73	68	80
Cu	51	12	90	64	61	50	73	12	75	76	73	77
Ni	53	62	108	48	38	50	43	64	93	91	88	89
V	331	317	267	472	466	410	477	345	287	278	311	318
Sc	40.2	38.0	37.6	42.6	41.5	41.3	43.3	45.7	39.3	39.4	40.2	42.6
Cr	141	189	356	49	56	80	65	192	359	344	354	298
P	1177	1588	1276	2549	2799	2573	2606	1039	689	711	1077	1443
Y	35	37	27	56	52	51	56	36	28	28	34	35
Zr	89	102	91	151	131	118	131	103	73	77	76	84
Be	0.53	0.54	0.49	0.86	0.86	0.82	0.89	0.56	0.39	0.36	0.38	0.48
Co	41.7	40.2	43.8	52.0	43.0	45.9	49.5	40.4	42.2	41.7	41.6	46.0
Rb	0.08	0.05						0.09	0.04	0.03		
Nb	2.25	1.81	3.63	2.77	3.64	3.80	3.65	1.54	0.82	0.82	0.88	1.22
Cs	0.006	0.002	0.007	0.011	0.006	0.014	0.007	0.006	0.004	0.004	0.005	0.006
La	2.97	2.98	3.80	5.07	6.67	5.32	5.22	2.68	1.86	1.86	1.91	2.44
Ce	10.14	10.76	11.06	17.79	21.03	17.35	17.65	9.52	7.06	7.12	7.26	9.01
Pr	1.82	1.95	1.81	3.28	3.67	3.09	3.22	1.75	1.35	1.34	1.43	1.72
Nd	9.86	10.79	9.29	18.15	19.23	16.49	17.67	9.52	7.56	7.45	8.24	9.61
Sm	3.47	3.75	2.88	6.36	6.20	5.63	6.04	3.46	2.75	2.76	3.17	3.43
Eu	1.21	1.17	1.07	1.98	1.98	1.78	1.89	1.16	1.02	1.02	1.11	1.23
Gd	4.83	5.16	4.10	8.78	8.37	7.72	8.50	4.78	3.77	3.80	4.74	4.99
Tb	0.89	0.95	0.72	1.52	1.43	1.33	1.47	0.88	0.70	0.70	0.84	0.87
Dy	5.93	6.32	4.76	10.10	9.24	8.89	9.83	5.93	4.71	4.77	5.83	5.95
Ho	1.27	1.35	1.02	2.09	1.92	1.86	2.05	1.25	1.01	1.01	1.23	1.28
Er	3.42	3.72	2.78	5.63	5.14	4.96	5.48	3.46	2.77	2.80	3.39	3.47
Yb	3.35	3.51	2.71	5.43	4.82	4.65	5.15	3.34	2.63	2.77	3.29	3.42
Lu	0.53	0.54	0.43	0.88	0.78	0.74	0.81	0.53	0.43	0.44	0.51	0.54
Hf	2.11	2.50	2.32	3.40	3.11	2.91	2.03	1.06	1.94	2.05	2.05	2.28
Ta	0.16	0.14	0.26	0.21	0.26	0.26	0.26	0.11	0.07	0.07	0.08	0.10
Pb	0.267	0.379	0.409	0.386	0.259	0.290	0.366	0.235	0.190	0.692	0.296	0.404
Th	0.101	0.061	0.239	0.108	0.111	0.146	0.119	0.061	0.043	0.049	0.054	0.075
U	0.028	0.011	0.071	0.020	0.021	0.024	0.026	0.015	0.014	0.016	0.013	0.017
Y/Nb	16	21	7	20	14	13	15	23	34	34	39	29
Nb/Ta	14	13	14	13	14	14	14	14	12	12	12	12
Ce/Yb_N	0.84	0.85	1.13	0.91	1.21	1.04	0.95	0.79	0.75	0.71	0.61	0.73
La/Sm_N	0.55	0.51	0.85	0.51	0.69	0.61	0.56	0.50	0.44	0.43	0.39	0.46

Sample ID	4076-2054	4077-1654	4077-1718	4077-1922	4077-1931	4077-2003	4077-2008	4078-1709	4078-1759	4078-1817	4078-1833	4078-1903
Study Area	A	A	A	A	A	A	A	A	A	A	A	A
Jason Transect												
Morphology[1]	d	d	d	d	d	l	l	d	d	m	d	d
Lithologic Zone[2]	T	D	D	T	T	V	V	D	D	D	T	T
Depth (mbsl)	3346	3575	3538	3285	3279	3205	3199	3561	3558	3560	3547	3523
Latitude (°S)	22.881	22.886	22.886	22.882	22.882	22.882	22.882	22.884	22.885	22.885	22.885	22.884
Longitude (°W)	112.056	112.051	112.051	112.047	112.047	112.046	112.046	112.052	112.052	112.053	112.052	112.052
SiO_2 (wt%)	50.39	50.81	49.19	49.83	50.73	51.35	50.47	50.92	50.97	51.13	50.66	51.30
TiO_2	1.59	1.66	1.16	1.88	1.87	1.47	1.62	1.35	1.84	1.47	1.45	1.85
Al_2O_3	14.08	13.70	15.21	13.83	13.37	14.27	15.02	13.45	13.50	14.07	13.89	13.57
Fe_2O_3	11.99	12.45	10.04	13.20	13.42	11.12	11.65	11.18	13.73	11.89	11.64	13.81
FeO*	10.79	11.20	9.04	11.88	12.08	10.00	10.48	10.06	12.35	10.70	10.47	12.42
MnO	0.21	0.19	0.17	0.21	0.22	0.18	0.18	0.20	0.26	0.20	0.23	0.26
MgO	7.54	7.59	9.16	6.93	6.92	7.83	7.51	8.29	6.65	8.72	8.73	6.75
CaO	11.15	11.02	11.13	10.17	10.40	11.90	11.14	12.19	9.91	10.60	10.42	9.97
Na_2O	2.49	2.44	2.49	2.83	2.77	2.81	2.80	2.57	3.09	2.39	2.48	3.06
K_2O	0.11	0.04	0.06	0.06	0.04	0.08	0.13	0.03	0.06	0.05	0.05	0.06
Total	99.55	99.90	98.62	98.94	99.75	101.00	100.50	100.19	100.01	100.52	99.55	100.63
Mg#	55.5	54.7	64.4	51.0	50.5	58.3	56.1	59.5	49.0	59.2	59.8	49.2
LOI	1.8	1.4	1.8	0.4	2.2	0.1	1.4	1.2	1.9	2.1	1.9	1.2
Sr (ppm)	107	96	89	109	99	111	98	95	101	85	89	101
Ba	4.61	4.03	1.72	5.29	5.00	5.35	5.64	3.73	5.40	3.84	3.81	5.30
Zn	83	44	48	100	104	79	88	83	105	60	99	96
Cu	69	27	12	83	72	66	73	67	71	87	78	65
Ni	64	63	98	54	51	62	89	67	45	66	59	42
V	350	360	283	390	395	327	331	328	392	339	336	404
Sc	43.3	43.2	39.4	41.8	42.7	42.5	38.7	47.4	43.5	44.4	44.3	44.9
Cr	190	170	378	107	109	172	252	185	73	201	145	69
P	1542	1602	1190	1967	2154	1640	1679	1509	1936	1308	1297	1711
Y	37	40	28	46	44	33	41	33	45	37	32	42
Zr	88	98	58	110	107	86	107	72	100	64	76	93
Be	0.64	0.64	0.73	0.61	0.68	0.56	0.57	0.53	0.67	0.51	0.46	0.65
Co	48.0	44.5	41.6	54.7	47.7	44.7	45.6	44.8	47.2	46.3	40.0	43.2
Rb			0.15									
Nb	1.65	2.00	0.91	2.16	2.20	1.74	1.56	1.33	2.02	1.34	1.42	1.91
Cs	0.019	0.006	0.006	0.007	0.006	0.014	0.004	0.006	0.006	0.009	0.010	0.006
La	2.83	3.22	1.93	3.81	3.75	3.03	2.88	2.55	3.64	2.56	2.37	3.40
Ce	10.07	11.39	7.34	13.15	13.06	10.39	10.35	9.06	12.65	9.06	8.33	11.90
Pr	1.88	2.09	1.39	2.45	2.45	1.91	1.96	1.69	2.36	1.71	1.56	2.23
Nd	10.51	11.52	7.69	13.57	13.48	10.37	11.00	9.47	13.00	9.51	8.59	12.17
Sm	3.78	4.10	2.81	4.74	4.71	3.56	3.99	3.37	4.64	3.57	3.18	4.37
Eu	1.36	1.40	1.02	1.66	1.60	1.31	1.36	1.21	1.50	1.25	1.14	1.41
Gd	5.45	5.82	3.84	6.87	6.56	5.05	5.74	4.81	6.58	5.19	4.67	6.16
Tb	0.95	1.03	0.73	1.20	1.13	0.87	1.01	0.85	1.15	0.91	0.82	1.07
Dy	6.48	6.91	4.83	8.06	7.47	5.64	6.91	5.70	7.70	6.16	5.43	7.18
Ho	1.37	1.47	1.03	1.71	1.60	1.19	1.45	1.19	1.60	1.31	1.17	1.48
Er	3.72	3.97	2.76	4.59	4.29	3.16	3.95	3.17	4.38	3.54	3.17	3.97
Yb	3.55	3.74	2.67	4.43	4.19	2.91	3.80	3.02	4.14	3.42	3.02	3.83
Lu	0.56	0.57	0.41	0.68	0.65	0.46	0.59	0.47	0.65	0.53	0.46	0.58
Hf	2.05	2.27	1.34	2.65	2.26	1.88	2.45	1.77	2.58	1.66	2.00	2.37
Ta	0.12	0.14	0.07	0.17	0.16	0.13	0.12	0.11	0.15	0.11	0.11	0.14
Pb	0.218	0.255	0.211	1.317	0.386	0.370	0.414	0.554	0.463	0.412	0.170	2.507
Th	0.057	0.089	0.043	0.117	0.103	0.065	0.079	0.058	0.086	0.060	0.062	0.075
U	0.133	0.029	0.014	0.035	0.025	0.378	0.054	0.030	0.023	0.017	0.020	0.015
Y/Nb	23	20	31	22	20	19	26	25	23	28	23	22
Nb/Ta	14	14	13	13	14	13	13	12	13	12	13	13
Ce/Yb_N	0.79	0.85	0.76	0.83	0.87	0.99	0.76	0.83	0.85	0.74	0.77	0.86
La/Sm_N	0.48	0.51	0.44	0.52	0.51	0.55	0.47	0.49	0.51	0.46	0.48	0.50

Sample ID	4078-2008	4078-2020	4079-1616	4079-1656	4079-1707	4079-1744	4079-1811	4079-1815	4079-1840	4079-1846	4079-1847	4079-1854
Study Area	A	A	A	A	A	A	A	A	A	A	A	A
Jason Transect												
Morphology[1]	d	p	d	p	s	s	d	d	p	p	p	p
Lithologic Zone[2]	T	V	D	T	T	V	V	V	V	V	V	V
Depth (mbsl)	3344	3333	3432	3348	3336	3277	3234	3234	3134	3177	3177	3167
Latitude (°S)	22.883	22.883	22.875	22.875	22.874	22.874	22.874	22.874	22.874	22.874	22.874	22.874
Longitude (°W)	112.052	112.052	112.068	112.068	112.067	112.067	112.067	112.067	112.067	112.067	112.067	112.067
SiO_2 (wt%)	51.76	50.81	51.57	50.30	50.45	50.78	50.66	50.76	50.15	50.93	50.67	50.28
TiO_2	1.53	1.29	2.39	1.42	2.05	1.56	2.34	1.66	1.65	1.69	1.67	2.67
Al_2O_3	13.96	14.65	13.24	14.26	13.80	14.07	13.26	13.98	13.73	14.11	14.21	12.96
Fe_2O_3	11.98	10.72	14.45	10.99	13.55	12.18	14.05	12.49	11.68	12.25	12.14	15.02
FeO*	10.78	9.65	13.00	9.89	12.20	10.96	12.64	11.24	10.51	11.02	10.92	13.51
MnO	0.22	0.18	0.25	0.20	0.22	0.29	0.21	0.19	0.19	0.21	0.20	0.24
MgO	8.08	8.30	7.09	8.42	7.16	8.07	7.02	8.07	7.90	7.67	7.65	6.04
CaO	11.03	11.44	10.19	10.48	9.96	10.40	9.76	10.51	11.14	10.70	10.45	9.44
Na_2O	2.63	2.75	2.57	2.45	2.45	2.47	2.85	2.57	2.65	2.71	2.72	3.02
K_2O	0.05	0.06	0.05	0.06	0.06	0.05	0.05	0.08	0.10	0.06	0.08	0.08
Total	101.24	100.21	101.78	98.57	99.71	99.87	100.20	100.32	99.19	100.31	99.88	99.85
Mg#	57.2	60.5	49.3	60.3	51.1	56.8	49.8	56.1	57.3	55.4	55.5	44.3
LOI	1.6	2.1	2.1	2.2	1.5	2.0	2.0	1.9	1.7	1.5	1.4	1.2
Sr (ppm)	100	102	100	92	89	92	95	104	110	113	111	103
Ba	5.55	4.49	4.93	3.79	5.00	3.72	5.91	4.78	5.63	6.82	6.03	6.67
Zn	107	87	58	67	96	125	102	87	83	106	140	123
Cu	60	70	63	73	65	64	56	117	65	67	65	54
Ni	59	89	48	70	60	55	61	63	66	61	68	49
V	350	299	341	300	376	329	345	300	304	297	343	455
Sc	45.4	41.7	34.3	38.9	40.5	41.0	34.9	35.3	36.0	34.3	36.9	37.4
Cr	145	250	133	220	130	116	128	163	212	179	153	77
P	1436	1197	2207	1396	2062	1429	2460	1620	1651	1682	1633	2719
Y	35	31	47	32	46	34	51	35	38	37	36	63
Zr	94	75	123	80	132	77	132	80	113	106	101	187
Be	0.54	0.49	0.69	0.77	0.88	0.81	0.85	0.79	0.84	0.83	0.31	0.44
Co	39.9	42.9	42.6	40.1	45.7	41.3	42.8	42.1	41.4	41.9	41.3	42.1
Rb			0.06	0.22	0.19	0.18		0.20	0.31	0.25	0.23	0.22
Nb	1.92	1.67	3.09	1.54	2.72	2.03	3.09	2.45	2.43	2.67	2.65	3.59
Cs	0.005	0.019	0.005	0.010	0.009	0.008	0.006	0.005	0.007	0.010	0.008	0.006
La	2.86	2.54	4.35	2.61	4.09	2.99	4.77	3.23	3.44	3.51	3.52	5.42
Ce	9.60	8.75	14.77	9.45	14.55	10.34	16.31	11.18	11.96	11.86	12.03	19.38
Pr	1.76	1.61	2.68	1.73	2.66	1.89	3.00	1.98	2.14	2.10	2.13	3.53
Nd	9.70	8.75	14.54	9.39	13.70	9.96	16.29	10.76	10.79	11.03	11.01	18.68
Sm	3.43	3.09	5.13	3.32	4.73	3.56	5.67	3.79	3.85	3.82	3.83	6.50
Eu	1.22	1.10	1.63	1.17	1.53	1.17	1.81	1.22	1.31	1.31	1.31	2.06
Gd	4.89	4.38	7.17	4.45	6.19	4.66	7.68	4.86	5.00	4.97	5.06	8.44
Tb	0.86	0.77	1.26	0.83	1.16	0.89	1.33	0.91	0.96	0.95	0.95	1.60
Dy	5.79	5.15	8.20	5.56	7.79	5.91	8.72	6.02	6.48	6.30	6.25	10.77
Ho	1.22	1.07	1.72	1.20	1.70	1.28	1.84	1.30	1.41	1.36	1.34	2.33
Er	3.39	2.91	4.72	3.24	4.64	3.44	4.87	3.41	3.84	3.66	3.61	6.33
Yb	3.35	2.81	4.59	3.11	4.56	3.31	4.65	3.33	3.87	3.64	3.51	6.22
Lu	0.51	0.42	0.71	0.49	0.71	0.50	0.71	0.51	0.60	0.57	0.55	0.97
Hf	2.28	1.88	2.82	2.01	3.27	1.57	3.03	1.50	2.94	2.58	2.31	4.73
Ta	0.14	0.13	0.23	0.11	0.19	0.14	0.22	0.18	0.17	0.19	0.18	0.25
Pb	0.486	0.432	0.335	0.547	0.420	0.811	0.628	0.633	0.520	0.874	0.936	0.942
Th	0.099	0.081	0.130	0.065	0.130	0.078	0.105	0.087	0.148	0.140	0.127	0.197
U	0.027	0.023	0.050	0.022	0.047	0.021	0.030	0.019	0.054	0.046	0.035	0.064
Y/Nb	18	18	15	21	17	17	17	14	16	14	14	18
Nb/Ta	14	13	13	13	14	14	14	14	15	14	14	14
Ce/Yb_N	0.80	0.87	0.89	0.84	0.89	0.87	0.97	0.93	0.86	0.91	0.95	0.86
La/Sm_N	0.54	0.53	0.55	0.51	0.56	0.54	0.54	0.55	0.58	0.59	0.59	0.54

Sample ID	4079-1920	4079-1933	4079-2003	4080-1711	4080-1858	4080-1917	4080-1918	4080-2049	4081-1921	4081-1933	4081-2005	4081-2019
Study Area	A	A	A	A	A	A	A	A	B	B	B	B
Jason Transect												
Morphology[1]	p	s	p	d	d	d	d	p	d	d	d	d
Lithologic Zone[2]	V	V	V	D	D	D	D	T	D	D	D	D
Depth (mbsl)	3114	3090	2984	3570	3495	3428	3428	3069	3174	3147	3117	3114
Latitude (°S)	22.873	22.873	22.873	22.891	22.890	22.890	22.890	22.886	22.973	22.973	22.973	22.973
Longitude (°W)	112.067	112.067	112.066	112.044	112.043	112.043	112.043	112.041	111.880	111.880	111.879	111.879
SiO_2 (wt%)	51.66	50.14	50.10	50.45	50.54	50.45	50.87	50.99	50.96	50.38	50.85	50.65
TiO_2	1.70	2.38	1.20	1.32	1.60	1.82	1.82	1.23	1.59	1.74	1.85	1.74
Al_2O_3	14.31	13.07	15.44	14.77	13.99	13.75	13.95	15.00	13.48	13.82	13.31	13.47
Fe_2O_3	9.69	15.00	9.97	10.36	11.75	12.97	12.97	9.95	12.47	12.34	13.51	12.83
FeO*	8.72	13.49	8.98	9.32	10.57	11.67	11.67	8.96	11.22	11.10	12.16	11.54
MnO	0.20	0.23	0.17	0.19	0.23	0.27	0.25	0.17	0.18	0.21	0.22	0.23
MgO	7.31	5.79	8.25	8.33	7.92	7.63	7.26	8.01	7.47	7.42	7.24	7.37
CaO	11.66	10.18	12.06	11.60	11.10	9.99	10.20	12.17	10.59	11.56	11.22	11.00
Na_2O	2.70	2.62	2.48	2.41	2.65	2.53	2.56	2.62	2.57	2.58	2.49	2.54
K_2O	0.22	0.36	0.13	0.04	0.05	0.07	0.04	0.09	0.05	0.05	0.06	0.05
Total	99.43	99.67	99.83	99.55	99.88	99.47	99.91	100.24	99.37	100.10	100.74	99.87
	X											
Mg#	59.9	43.3	62.1	61.4	57.2	53.8	52.6	61.4	54.3	54.4	51.5	53.2
LOI	0.3	1.1	0.7	1.9	1.2	1.9	1.6	0.5	1.7	1.2	1.4	0.9
Sr (ppm)	135	104	127	105	98	91	92	91	85	101	85	84
Ba	21.29	10.01	10.41	2.79	2.45	2.18	2.15	2.95	18.21	2.99	13.45	1.61
Zn	91	121	69	72	53	52	54	1242	49	52	76	52
Cu	78	59	89	73	69	30	74	76	75	82	55	55
Ni	60	42	119	96	80	58	57	74	59	67	56	61
V	373	472	287	378	344	390	344	284	343	390	418	374
Sc	44.1	42.9	43.4	39.9	41.3	44.2	42.7	43.0	43.6	46.4	47.9	43.9
Cr	204	67	425	330	311	152	151	319	116	158	95	126
P	1700	2429	1410	1169	1370	1518	1569	1044				
Y	45	56	31	29	37	40	39	32	35	38	39	35
Zr	121	173	75	69	93	79	89	64	74	105	104	79
Be	0.28	0.39	0.51	0.42	0.51	0.56	0.60	0.34	0.49	0.58	0.51	0.48
Co	46.2	44.0	47.6	38.7	42.5	41.2	42.0	40.3	40.7	42.4	42.2	40.4
Rb	1.12	6.27	0.92	0.04	0.13	0.17	0.20	1.68				
Nb	2.31	3.15	2.50	1.59	1.40	1.58	1.59	0.84	1.59	2.17	1.69	1.57
Cs	0.023	0.195	0.015	0.005	0.005	0.009	0.009	0.104				
La	3.65	4.74	2.98	2.43	2.69	2.97	3.03	1.80	2.90	3.13	2.85	2.50
Ce	12.45	16.32	9.86	8.36	9.80	10.87	11.03	6.84	9.90	10.94	10.11	9.42
Pr	2.24	3.07	1.70	1.50	1.77	2.00	2.04	1.29	1.77	1.99	1.85	1.75
Nd	11.67	16.25	9.22	8.32	9.90	11.30	11.13	7.45	9.90	10.91	10.20	9.55
Sm	4.12	5.67	3.15	3.02	3.61	4.08	4.10	2.85	3.46	3.75	3.78	3.46
Eu	1.42	1.85	1.16	1.02	1.23	1.37	1.36	1.04	1.13	1.24	1.17	1.03
Gd	5.61	7.37	4.17	4.27	4.87	5.46	5.34	3.97	4.74	5.26	5.18	4.69
Tb	1.08	1.42	0.79	0.76	0.93	1.03	1.02	0.77	0.78	0.86	0.88	0.81
Dy	7.30	9.59	5.23	5.12	6.19	6.88	6.67	5.22	5.76	6.35	6.58	5.92
Ho	1.57	2.06	1.13	1.09	1.34	1.46	1.43	1.16	1.30	1.43	1.46	1.30
Er	4.38	5.74	3.04	2.95	3.57	3.83	3.81	3.19	3.20	3.46	3.62	3.19
Yb	4.40	5.66	3.07	2.90	3.63	3.75	3.71	3.18	3.32	3.69	3.72	3.28
Lu	0.71	0.91	0.47	0.44	0.57	0.60	0.59	0.50	0.49	0.57	0.61	0.54
Hf	3.20	4.59	2.44	1.52	2.25	2.32	2.35	2.12	1.67	2.46	2.47	1.68
Ta	0.17	0.23	0.18	0.12	0.11	0.12	0.12	0.07	0.13	0.17	0.14	0.14
Pb	0.718	0.809	0.601	0.118	0.274	0.308	0.317	1.537	0.055	0.084	4.386	0.177
Th	0.142	0.181	0.148	0.064	0.063	0.054	0.063	0.061	0.060	0.110	0.087	0.058
U	0.084	0.091	0.054	0.016	0.013	0.023	0.019	2.009	0.011	0.044	0.044	0.007
Y/Nb	20	18	13	18	26	25	25	38	22	18	23	22
Nb/Ta	14	14	14	13	12	13	13	12	12	13	12	11
Ce/Yb_N	0.79	0.80	0.89	0.80	0.75	0.81	0.82	0.60	0.83	0.82	0.76	0.80
La/Sm_N	0.57	0.54	0.61	0.52	0.48	0.47	0.48	0.41	0.54	0.54	0.49	0.47

Sample ID	4081-2035	4081-2047	4081-2110	4081-2124	4081-2132	4081-2149	4081-2209	4081-2234	4081-2248	4082-1620	4082-1651	4082-1702
Study Area	B	B	B	B	B	B	B	B	B	B	B	B
Jason Transect												
Morphology[1]	d	d	d	d	d	d	d	d	d	d	d	d
Lithologic Zone[2]	D	D	D	D	D	D	D	D	D	D	D	D
Depth (mbsl)	3114	3113	3088	3083	3083	3081	3035	2985	2968	3121	3093	3093
Latitude (°S)	22.973	22.974	22.974	22.974	22.974	22.974	22.974	22.973	22.973	22.972	22.972	22.972
Longitude (°W)	111.879	111.879	111.879	111.878	111.878	111.878	111.878	111.878	111.878	111.882	111.882	111.882
SiO_2 (wt%)	51.54	50.35	50.55	50.79	49.98	50.38	50.43	51.57	50.35	50.47	50.78	50.19
TiO_2	1.96	1.62	1.71	1.73	1.43	1.64	1.47	2.04	1.57	1.83	2.50	2.52
Al_2O_3	13.42	13.75	13.36	13.73	14.16	13.84	13.94	13.41	14.71	13.35	12.94	12.60
Fe_2O_3	11.67	11.96	12.77	12.41	11.03	12.24	11.47	14.22	12.24	13.73	15.73	15.71
FeO*	10.50	10.77	11.49	11.17	9.93	11.01	10.32	12.79	11.01	12.35	14.16	14.13
MnO	0.19	0.21	0.21	0.19	0.18	0.19	0.19	0.27	0.24	0.23	0.24	0.23
MgO	6.85	7.44	7.24	7.37	7.86	7.60	7.85	7.01	8.06	6.81	6.61	6.18
CaO	10.99	11.48	11.02	11.20	11.45	11.36	11.69	10.39	10.65	10.61	9.49	9.35
Na_2O	2.95	2.52	2.56	2.69	2.47	2.42	2.40	2.65	2.54	2.65	2.94	2.82
K_2O	0.08	0.05	0.06	0.05	0.05	0.07	0.06	0.04	0.03	0.06	0.06	0.06
Total	99.64	99.38	99.47	100.17	98.62	99.74	99.51	101.59	100.38	99.73	101.30	99.66
	X											
Mg#	53.7	55.2	52.9	54.1	58.5	55.2	57.5	49.4	56.6	49.6	45.4	43.8
LOI	1.9	1.1	0.9	0.8	1.1	0.9	1.0	1.6	1.7	1.4	1.4	1.3
Sr (ppm)	85	90	88	99	94	93	94	91	93	83	86	86
Ba	2.58	2.53	2.76	2.18	2.51	2.24	1.95	2.45	2.69	3.27	3.79	3.96
Zn	50	86	56	67	56	66	58	87	89	109	102	83
Cu	25	66	74	23	63	60	67	63	64	68	47	58
Ni	52	69	60	62	84	78	79	46	81	45	38	37
V	399	326	351	356	310	343	315	408	333	386	493	482
Sc	44.9	44.8	42.5	43.4	43.3	43.0	42.4	44.1	41.2	43.2	45.7	43.1
Cr	91	182	116	133	301	201	280	60	205	43	33	29
P						1465	1370	1612			1873	
Y	40	34	38	36	30	35	33	43	33	37	50	49
Zr	93	89	81	87	76	77	82	102	84	103	126	132
Be	0.59	0.46	0.56	0.56	0.48	0.51	0.48	0.62	0.48	0.48	0.82	0.78
Co	35.1	40.4	45.1	41.3	41.4	41.6	41.6	41.8	42.2	42.9	44.5	41.1
Rb												
Nb	1.93	1.77	2.01	1.97	1.71	1.55	1.44	2.06	1.57	1.57	2.84	2.85
Cs						0.004	0.005	0.007	0.004	0.008	0.002	0.000
La	3.30	2.57	2.99	2.97	2.36	2.70	2.37	3.40	2.64	2.52	4.27	4.29
Ce	11.31	9.24	10.65	10.61	8.42	9.30	8.46	11.94	9.47	9.28	14.90	15.04
Pr	2.00	1.64	1.94	1.89	1.48	1.70	1.55	2.19	1.74	1.67	2.74	2.78
Nd	11.31	9.25	10.62	10.25	8.32	9.42	8.65	12.18	9.52	9.67	15.09	15.04
Sm	4.07	3.49	3.85	3.85	3.02	3.41	3.15	4.38	3.49	3.57	5.35	5.30
Eu	1.34	1.14	1.23	1.18	1.00	1.14	1.06	1.38	1.10	1.21	1.62	1.57
Gd	5.49	4.52	5.21	4.85	3.93	4.84	4.47	5.82	4.04	4.34	6.97	6.31
Tb	0.91	0.79	0.87	0.83	0.70	0.86	0.77	0.99	0.71	0.76	1.22	1.05
Dy	6.74	5.79	6.63	6.17	5.07	5.96	5.51	7.36	5.80	6.34	8.78	8.39
Ho	1.53	1.27	1.44	1.32	1.07	1.30	1.19	1.58	1.22	1.30	1.87	1.80
Er	3.65	3.05	3.43	3.21	2.72	3.35	3.12	3.99	2.81	3.14	4.61	4.30
Yb	3.61	3.26	3.71	3.60	2.91	3.44	3.25	4.27	3.51	3.81	5.04	5.23
Lu	0.57	0.47	0.55	0.55	0.43	0.53	0.51	0.66	0.53	0.60	0.79	0.77
Hf	2.22	2.05	1.86	1.93	1.71	1.57	2.01	2.49	1.68	2.42	3.02	2.90
Ta	0.16	0.15	0.17	0.15	0.13	0.13	0.13	0.17	0.14	0.12	0.22	0.24
Pb	9.031	0.100	0.158	0.028	0.044	0.087	0.653	0.156	0.187	0.478	0.333	0.313
Th	0.081	0.096	0.089	0.055	0.072	0.057	0.067	0.079	0.057	0.080	0.098	0.114
U		0.163	0.054	0.046	0.031	0.030	0.023	0.028	0.003	0.189	0.043	0.053
Y/Nb	21	19	19	18	18	23	23	21	21	24	18	17
Nb/Ta	12	12	12	13	13	12	11	12	11	13	13	12
Ce/Yb_N	0.87	0.79	0.80	0.82	0.80	0.75	0.72	0.78	0.75	0.68	0.82	0.80
La/Sm_N	0.52	0.47	0.50	0.50	0.50	0.51	0.49	0.50	0.49	0.46	0.52	0.52

Sample ID	4082-1722	4082-1749	4082-1754	4082-1814	4082-1820	4082-1837	4082-1838	4082-1904	4082-2002	4082-2008	4082-2104	4083-1644
Study Area	B	B	B	B	B	B	B	B	B	B	B	B
Jason Transect												
Morphology[1]	d	d	d	d	d	d	d	d	d	d	p	d
Lithologic Zone[2]	D	D	D	D	D	D	D	D	D	D	T	D
Depth (mbsl)	3087	3086	3085	3091	3091	3092	3092	3094	2942	2942	2653	3087
Latitude (°S)	22.972	22.973	22.973	22.973	22.973	22.974	22.974	22.974	22.973	22.973	22.971	22.964
Longitude (°W)	111.882	111.880	111.880	111.880	111.880	111.880	111.880	111.879	111.878	111.878	111.875	111.887
SiO_2 (wt%)	50.45	50.24	50.39	50.84	50.82	50.02	50.48	50.54	50.10	50.28	51.73	49.75
TiO_2	2.11	2.06	2.04	1.75	1.86	1.78	1.81	1.82	1.72	1.53	1.79	1.22
Al_2O_3	13.08	13.31	13.33	13.86	13.40	13.64	13.94	13.37	13.68	13.97	14.10	15.19
Fe_2O_3	14.49	14.07	13.99	12.66	13.29	12.77	12.87	12.80	13.69	12.00	10.32	10.13
FeO*	13.04	12.66	12.59	11.39	11.96	11.49	11.58	11.52	12.32	10.79	9.28	9.11
MnO	0.23	0.21	0.21	0.21	0.25	0.26	0.24	0.22	0.25	0.23	0.20	0.19
MgO	6.91	6.64	6.69	7.00	7.26	7.35	7.26	7.23	7.78	7.68	7.19	8.16
CaO	9.92	10.14	10.27	11.10	11.03	11.17	11.29	11.46	9.96	11.42	11.72	10.40
Na_2O	2.99	3.22	2.91	2.78	2.45	2.92	2.84	2.58	2.37	2.51	2.76	3.33
K_2O	0.08	0.08	0.11	0.06	0.06	0.07	0.06	0.06	0.06	0.15	0.17	0.04
Total	100.26	99.97	99.94	100.26	100.42	99.97	100.79	100.09	99.61	99.77	99.97	98.42
											X	
Mg#	48.6	48.3	48.7	52.3	52.0	53.3	52.8	52.8	53.0	55.9	58.0	61.5
LOI	1.3	1.4	1.4	1.0	1.0	1.4	1.3	1.1	1.8	1.2	0.4	2.2
Sr (ppm)	90	93	88	98	88	95	95	94	79	87	122	118
Ba	4.12	4.59	3.54	3.69	4.12	3.50	3.77	2.77	2.90	3.17	25.31	7.06
Zn	86	70	84	88	74	77	77	80	106	108	111	84
Cu	78	70	73	69	70	84	70	26	61	45	66	53
Ni	43	53	53	57	57	61	62	61	65	69	62	102
V	430	407	400	370	387	381	366	382	366	354	358	281
Sc	44.3	42.2	42.4	42.9	43.7	45.4	43.4	43.6	42.2	43.7	45.7	38.0
Cr	38	104	76	88	120	117	120	116	150	159	139	352
P												1411
Y	41	45	44	36	40	38	38	37	36	34	52	28
Zr	83	94	94	98	101	96	98	96	101	82	109	82
Be	0.64	0.66	0.61	0.54	0.57	0.55	0.57	0.57	0.48	0.48	0.50	0.64
Co	42.8	45.1	57.0	42.6	43.7	40.0	43.4	42.5	60.3	39.2	51.2	42.3
Rb		0.00			0.02						0.54	0.43
Nb	2.10	2.05	2.04	1.86	2.46	1.90	1.91	1.77	1.81	1.54	1.67	2.42
Cs	0.005	0.013	0.005	0.001	0.009	0.011	0.003	0.006	0.012	0.004	0.021	0.017
La	3.39	3.41	3.47	2.88	3.23	2.88	2.86	2.94	2.65	2.45	3.17	3.15
Ce	11.76	12.07	11.94	10.04	11.13	10.33	10.28	10.31	9.56	8.71	11.12	9.69
Pr	2.16	2.20	2.21	1.85	2.03	1.86	1.85	1.91	1.74	1.58	2.10	1.66
Nd	11.81	12.15	12.51	10.24	11.03	10.51	10.48	10.63	9.65	8.97	11.78	8.70
Sm	4.19	4.42	4.53	3.77	4.09	3.85	3.73	3.67	3.47	3.22	4.49	2.94
Eu	1.36	1.38	1.37	1.18	1.27	1.17	1.24	1.24	1.08	1.07	1.40	1.05
Gd	5.05	5.29	5.22	4.41	4.67	4.57	4.44	4.67	4.18	4.04	5.50	3.99
Tb	0.86	0.93	0.91	0.78	0.84	0.80	0.81	0.83	0.78	0.73	0.96	0.70
Dy	6.88	7.42	7.29	5.90	6.63	6.19	6.16	6.21	6.05	5.66	7.84	4.74
Ho	1.50	1.65	1.61	1.31	1.45	1.40	1.40	1.39	1.30	1.27	1.76	1.01
Er	3.48	3.85	3.78	3.07	3.44	3.24	3.29	3.30	3.12	2.95	4.30	2.74
Yb	4.04	4.51	4.39	3.52	3.89	4.03	3.87	3.71	3.93	3.76	5.31	2.67
Lu	0.64	0.72	0.70	0.57	0.62	0.65	0.62	0.57	0.59	0.55	0.77	0.43
Hf	1.77	2.23	2.50	2.13	2.01	2.24	2.38	2.21	1.76	1.95	3.15	2.13
Ta	0.16	0.16	0.17	0.15	0.19	0.17	0.15	0.14	0.15	0.13	0.13	0.19
Pb	0.288	0.347	0.572	0.438	0.316	0.293	0.308	0.191	0.232	0.333	0.545	0.070
Th	0.073	0.094	0.076	0.080	0.134	0.084	0.110	0.086	0.074	0.044	0.109	0.134
U	0.039	0.030	0.015	0.047	0.030	0.025	0.031	0.045	0.032	0.049	0.063	0.109
Y/Nb	19	22	21	19	16	20	20	21	20	22	31	11
Nb/Ta	13	13	12	13	13	12	13	13	12	12	13	13
Ce/Yb_N	0.81	0.74	0.75	0.79	0.80	0.71	0.74	0.77	0.68	0.64	0.58	1.01
La/Sm_N	0.52	0.50	0.49	0.49	0.51	0.48	0.50	0.52	0.49	0.49	0.46	0.69

Sample ID	4083-1724	4083-1750	4083-1853	4083-1923	4083-1937	4083-1944	4083-2024	4084-1638	4084-1759	4084-1814	4084-1830	4084-1847
Study Area	B	B	B	B	B	B	B	B	B	B	B	B
Jason Transect												
Morphology[1]	d	d	d	d	d	p	p	d	d	d	d	d
Lithologic Zone[2]	D	D	D	T	T	T	T	D	D	T	T	V
Depth (mbsl)	3075	3056	3018	2889	2851	2839	2839	2778	2908	2804	2768	2649
Latitude (°S)	22.964	22.963	22.963	22.963	22.963	22.963	22.963	22.961	22.960	22.959	22.959	22.958
Longitude (°W)	111.886	111.886	111.884	111.883	111.883	111.883	111.881	111.889	111.884	111.883	111.882	111.880
SiO_2 (wt%)	50.75	50.27	49.95	50.05	50.95	50.07	50.72	51.11	50.31	51.07	52.42	50.20
TiO_2	1.80	1.98	2.19	1.53	1.34	1.98	2.15	1.46	2.57	1.46	1.43	1.57
Al_2O_3	13.23	13.12	12.68	13.97	14.21	13.64	12.91	14.30	12.60	13.94	14.37	14.38
Fe_2O_3	13.34	14.16	15.31	11.68	11.50	13.11	14.97	11.41	16.68	12.39	9.35	11.94
FeO*	12.00	12.74	13.77	10.51	10.35	11.80	13.47	10.27	15.01	11.15	8.42	10.75
MnO	0.21	0.23	0.25	0.24	0.21	0.26	0.24	0.20	0.25	0.20	0.20	0.21
MgO	6.86	6.26	6.03	7.66	8.21	7.61	6.52	7.34	6.84	7.41	7.87	8.20
CaO	10.94	10.41	9.62	10.59	11.07	9.96	8.90	11.65	7.94	11.65	12.38	10.05
Na_2O	2.40	2.76	2.86	2.52	2.37	2.63	3.00	2.61	2.71	2.53	2.57	2.94
K_2O	0.11	0.05	0.06	0.07	0.07	0.10	0.16	0.15	0.06	0.20	0.21	0.07
Total	99.65	99.24	98.95	98.31	99.92	99.34	99.57	100.23	99.95	100.85	100.80	99.56
											X	
Mg#	50.5	46.7	43.8	56.5	58.6	53.5	46.3	56.0	44.8	54.2	62.5	57.6
LOI	1.3	1.3	1.3	1.6	1.4	1.9	1.3	0.5	2.0	0.7	0.4	1.8
Sr (ppm)	82	96	92	86	76	88	95	108	90	106	126	91
Ba	2.96	3.29	3.68	2.41	1.69	3.62	3.31	7.13	4.22	7.01	14.27	2.98
Zn	67	142	121	113	92	123	130	88	125	86	90	71
Cu	63	49	57	62	65	65	59	71	63	63	67	89
Ni	51	39	31	64	62	52	29	57	28	53	80	60
V	385	428	448	346	330	400	442	366	479	309	318	338
Sc	44.6	43.9	44.5	42.8	43.2	44.3	43.7	47.4	42.6	41.5	42.3	42.2
Cr	74	59	16	149	164	101	11	128	14	123	164	137
P	1622	1717	1879	1405	1191	1854	1919	1274	2391	1313	1154	1247
Y	42	40	46	37	33	44	52	36	54	35	36	34
Zr	82	93	107	91	75	101	143	91	129	96	88	66
Be	0.58	0.63	0.67	0.48	0.39	0.65	0.64	0.41	0.79	0.50	0.44	0.45
Co	43.9	44.6	44.4	43.0	43.7	39.7	45.2	42.3	46.3	40.9	48.3	39.0
Rb						0.20	0.58	2.43	0.22	2.81	0.56	0.28
Nb	1.71	1.85	1.97	1.56	1.08	2.41	1.90	1.44	2.80	1.45	1.39	1.42
Cs	0.008	0.009	0.004	0.004	0.002	0.023	0.045	0.123	0.014	0.134	0.013	0.019
La	2.85	3.18	3.62	2.55	1.94	3.57	3.37	2.53	4.47	2.52	2.45	2.55
Ce	9.98	10.92	12.51	9.03	7.21	12.50	12.43	8.74	15.59	8.50	8.42	8.72
Pr	1.91	2.02	2.34	1.69	1.36	2.29	2.36	1.63	2.91	1.61	1.56	1.65
Nd	10.70	11.28	13.01	9.53	7.87	12.60	13.32	8.97	15.82	8.96	8.78	9.12
Sm	3.97	4.14	4.75	3.60	3.01	4.51	4.90	3.24	5.59	3.29	3.21	3.34
Eu	1.34	1.37	1.61	1.25	1.10	1.50	1.67	1.23	1.82	1.20	1.17	1.15
Gd	5.82	5.72	6.69	5.15	4.57	6.42	7.11	5.03	7.97	4.84	4.79	4.94
Tb	1.02	1.00	1.18	0.91	0.81	1.13	1.27	0.92	1.46	0.89	0.87	0.90
Dy	7.04	6.85	7.87	6.11	5.49	7.46	8.61	6.04	9.40	5.95	5.90	5.86
Ho	1.53	1.44	1.71	1.36	1.20	1.60	1.86	1.31	1.99	1.28	1.28	1.25
Er	4.11	3.96	4.55	3.64	3.28	4.32	5.27	3.72	5.42	3.60	3.60	3.40
Yb	4.06	3.98	4.53	3.55	3.18	4.18	5.02	3.64	5.14	3.51	3.58	3.31
Lu	0.64	0.61	0.71	0.55	0.48	0.65	0.81	0.59	0.84	0.58	0.57	0.52
Hf	1.59	2.18	2.55	2.57	2.00	2.16	3.82	2.51	2.96	2.48	2.30	1.46
Ta	0.15	0.15	0.16	0.13	0.10	0.18	0.17	0.11	0.20	0.11	0.11	0.10
Pb		0.039	0.219	0.992	0.675	0.335	0.405	0.408	0.724	1.083	0.352	0.206
Th	0.064	0.066	0.072	0.078	0.053	0.096	0.104	0.086	0.103	0.084	0.079	0.041
U	0.031	0.049	0.037	0.026	0.022	0.052	0.038	0.048	0.035	0.049	0.150	0.020
Y/Nb	24	22	23	24	30	18	27	25	19	24	26	24
Nb/Ta	12	12	12	12	11	13	11	13	14	14	13	14
Ce/Yb_N	0.68	0.76	0.77	0.71	0.63	0.83	0.69	0.67	0.84	0.67	0.65	0.73
La/Sm_N	0.46	0.50	0.49	0.46	0.42	0.51	0.44	0.50	0.52	0.49	0.49	0.49

Sample ID	4084-1931	4084-1937	4084-2004	4085-1819	4085-1935	4086-1627	4086-1711	4086-1740	4086-1815	4086-1843	4086-1905	4086-1925	4086-2006
Study Area	B	B	B	B	B	B	B	B	B	B	B	B	B
Jason Transect													
Morphology[1]	p	p	p	d	p	d	d	d	d	d	d	d	p
Lithologic Zone[2]	V	V	V	T	V	D	D	D	D	D	D	D	V
Depth (mbsl)	2656	2644	2638	2756	2589	3124	3095	3073	3045	2977	2893	2823	2664
Latitude (°S)	22.958	22.957	22.957	22.946	22.946	22.969	22.969	22.969	22.970	22.970	22.970	22.969	22.967
Longitude (°W)	111.877	111.877	111.877	111.887	111.882	111.882	111.882	111.882	111.881	111.880	111.879	111.879	111.877
SiO_2 (wt%)	51.25	51.78	50.07	51.29	52.07	50.06	49.83	49.88	49.29	49.88	50.10	50.46	50.89
TiO_2	2.38	1.47	2.49	1.58	1.42	1.86	1.56	2.07	1.77	1.84	1.90	1.64	1.93
Al_2O_3	12.66	13.85	12.42	13.78	14.59	13.26	13.66	13.03	13.69	13.36	13.76	14.03	13.53
Fe_2O_3	15.97	10.20	16.33	12.32	9.26	14.11	12.03	14.38	12.76	13.43	13.49	11.96	12.03
FeO*	14.37	9.18	14.69	11.09	8.33	12.70	10.82	12.94	11.49	12.08	12.14	10.76	10.83
MnO	0.25	0.20	0.26	0.19	0.20	0.23	0.23	0.23	0.19	0.23	0.24	0.22	0.21
MgO	6.59	7.99	5.90	7.53	7.52	6.67	7.51	6.54	7.30	7.20	7.12	7.73	6.78
CaO	9.32	12.33	10.09	11.31	12.31	10.57	11.47	9.88	10.92	10.15	10.18	10.87	10.87
Na_2O	2.91	2.53	2.68	2.64	2.55	2.56	2.44	2.82	2.57	2.88	2.71	2.58	2.71
K_2O	0.05	0.16	0.07	0.06	0.22	0.08	0.07	0.03	0.02	0.06	0.10	0.06	0.13
Total	101.37	100.50	100.32	100.70	100.15	99.41	98.80	98.86	98.52	99.03	99.60	99.54	99.07
					X								X
Mg#	45.0	60.8	41.7	54.8	61.7	48.4	55.3	47.4	53.1	51.5	51.1	56.1	52.8
LOI	1.1	0.6	1.4	0.5	0.5	1.3	1.2	1.5	1.2	1.7	1.3	1.6	0.3
Sr (ppm)	91	121	101	94	112	82	84	91	94	90	86	93	113
Ba	4.26	18.87	17.13	2.98	11.33	2.10	3.69	3.12	2.30	2.60	2.67	4.64	10.22
Zn	116	94	123	95	83	112	84	107	50	102	122	85	110
Cu	55	47	60	62	73	50	58	47	76	65	70	66	62
Ni	37	60	33	59	93	41	65	37	62	50	48	69	51
V	451	329	458	355	346	397	353	438	365	400	412	354	407
Sc	44.0	46.2	45.0	44.8	45.3	44.4	43.7	43.3	43.6	44.6	44.7	43.2	43.4
Cr	48	146	18	147	252	40	181	44	175	92	94	196	90
P	2014	1231	2192			1506	1394	1812	1626	1514	1584	1495	1842
Y	50	41	51	36	38	41	35	44	39	38	41	38	48
Zr	143	91	117	95	84	105	86	99	77	94	107	98	128
Be	0.69	0.37	0.74	0.43	0.45	0.58	0.51	0.65	0.59	0.58	0.59	0.55	0.61
Co	45.8	46.2	48.2	41.0	49.3	44.8	43.4	43.3	43.3	41.1	42.5	41.9	43.0
Rb	0.09	1.69	0.34	0.07	0.36					0.06			1.03
Nb	2.27	1.32	2.39	1.25	1.33	1.61	1.98	2.11	1.76	1.68	1.82	2.29	2.07
Cs	0.004	0.018	0.030	0.008	0.014	0.002	0.001	0.000	0.002	0.018	0.002	0.001	0.016
La	3.84	2.46	4.02	2.32	2.42	2.77	2.96	3.50	3.08	2.77	3.05	3.13	3.43
Ce	13.25	8.59	14.20	8.58	8.71	9.85	9.56	12.04	10.68	9.95	10.61	10.18	11.96
Pr	2.46	1.66	2.65	1.58	1.56	1.88	1.75	2.24	1.96	1.86	1.96	1.84	2.23
Nd	13.58	9.50	14.89	8.91	9.04	10.53	9.57	12.52	10.95	10.23	10.98	10.22	12.36
Sm	4.91	3.58	5.23	3.28	3.19	3.88	3.50	4.48	3.94	3.82	4.05	3.68	4.66
Eu	1.66	1.29	1.75	1.09	1.12	1.40	1.19	1.46	1.30	1.33	1.39	1.23	1.52
Gd	7.09	5.36	7.44	4.10	4.08	5.66	5.00	6.27	5.68	5.40	5.87	5.35	6.49
Tb	1.28	1.00	1.34	0.74	0.74	1.02	0.89	1.11	0.99	0.95	1.04	0.93	1.14
Dy	8.49	6.65	8.78	5.82	5.91	6.82	5.94	7.41	6.65	6.39	6.96	6.33	7.98
Ho	1.84	1.45	1.86	1.25	1.29	1.49	1.25	1.56	1.41	1.39	1.50	1.38	1.77
Er	5.13	4.11	5.15	3.18	3.16	4.07	3.47	4.29	3.81	3.72	4.06	3.69	4.82
Yb	5.11	4.01	4.99	3.93	3.70	4.07	3.47	4.29	3.81	3.69	4.01	3.79	4.75
Lu	0.80	0.63	0.77	0.63	0.61	0.65	0.55	0.69	0.59	0.58	0.63	0.61	0.76
Hf	3.82	2.57	2.55	2.62	2.48	2.61	1.89	2.43	1.92	2.28	2.57	2.59	3.55
Ta	0.17	0.11	0.18	0.10	0.12	0.13	0.15	0.16	0.14	0.15	0.15	0.18	0.17
Pb	0.269	0.434	0.417	0.388	0.421	0.161			0.616		0.019	0.042	0.855
Th	0.113	0.073	0.074	0.087	0.097	0.072	0.081	0.069	0.067	0.071	0.077	0.131	0.114
U	0.042	0.050	0.038	0.021	0.042	0.133	0.032	0.027	0.021	0.038	0.038	0.044	1.622
Y/Nb	22	31	21	29	29	26	18	21	22	23	23	17	23
Nb/Ta	13	12	14	12	11	12	14	13	12	11	12	13	12
Ce/Yb_N	0.72	0.59	0.79	0.61	0.65	0.67	0.76	0.78	0.78	0.75	0.73	0.75	0.70
La/Sm_N	0.50	0.44	0.50	0.46	0.49	0.46	0.55	0.50	0.51	0.47	0.49	0.55	0.48

Appendix B: Procedure for Quantitative Analyses of Photomicrographs

Quantitative analyses of Pito Deep photomicrographs were made using the program ImageJ (version 1.4.3). Photomicrographs of Pito Deep thin sections were made under plane- and cross-polarized light at magnifications ranging from 20x to 200x. The photos were imported into ImageJ as jpeg files and converted to grayscale using the Image > Type > 8 bit command. Plagioclase phenocrysts were enhanced using the Process > Enhance Contrast tool, with the Normalize setting selected to equalize the adjustment across the image. The area encompassed by the crystals was highlighted using the Image > Adjust > Threshold tool. An auto-threshold was performed initially, followed by manual adjustments to mask all of the visible plagioclase phenocrysts. The area consisting of plagioclase crystals was calculated as a percentage of pixels using the Analyze > Measure command. Results for multiple analyses of thin sections are summarized in the table below, where LFeO* indicates Low FeO* Group Sample; MC represents Main Composition Group Sample; PP represents plane polarized light; XP indicates crossed-polarized light.

Sample	021005-1355	020705-2131	4084-2004	4082-1820	020905-1404
Dike/Lava	Lava	Dike	Lava	Dike	Dike
LFeO*/MC	LFeO*	MC	MC	MC	MC
% Plag PP	34.9	37.0	21.4	28.5	26.1
% Plag PP	33.7	38.0	30.4	38.3	32.6
% Plag PP	37.7	40.7	31.7	35.0	30.1
% Plag XP	42.3	45.7	9.6	24.2	20.3
% Plag XP	38.9	36.1	17.6	21.7	17.2
% Plag XP	37.0	31.0	14.3	24.2	21.4
Avg % Plag	37.4	38.1	20.8	28.7	24.6
± 1σ	3.1	5.0	8.8	6.7	6.0

Appendix C: Dike Intrusion Model

The model for intrusion of a single dike is based on the work of Ida (1999), who examined the influence of magma pressure (p_m) and mean normal stress (σ_m) on the width (a) and height (h) of a dike. The system is reduced to three ordinary differential equations:

$$da/dt = \frac{a^3 (p_m + 2\sigma_m)}{2h^2} \quad (1)$$

$$dh/dt = \frac{a^2}{6h} \left(\frac{G}{2} h - p_m - 3\sigma_m\right) \quad (2)$$

$$dp_m/dt = \frac{-a^3}{6h} \left(\frac{G}{2} h + 2p_m + 3\sigma_m\right) \quad (3)$$

Stress is defined by the following relationship:

$$\sigma_m = \sigma - \frac{a}{h} \quad (4)$$

where σ represents crustal stress. This system of equations is nondimensionalized when scaled by the units for height (h_u; equation 5), buoyancy (G_u; 6), pressure and stress (p_u; 7), width (a_u; 8), time (t_u; 9), and magma flux (J_u; 10):

$$h_u = [f\mu \ / \ \pi(1 - \nu)\rho L k]^{1/2} \quad (5)$$

$$G_u = g\Delta\rho \quad (6)$$

$$p_u = g\Delta\rho h_u \quad (7)$$

$$a_u = \pi(1 - \nu)h_u p_u \ / \ f\mu \quad (8)$$

$$t_u = \eta h_u^2 \ / \ a_u^2 p_u \quad (9)$$

$$J_u = g\Delta\rho a_u^3 \ / \ 6\eta \quad (10)$$

Variables and values used in the calculations are listed in the following table.

Variable	Definition	Value
f	Dimensionless Parameter that relates Elastic Stress at the Dike Tip to Stress along the Length of the Dike	5
μ	Rigidity of Crust	30 GPa
ν	Poisson's Ratio	0.25
ρ	Magma Density	Varies; 2680 – 2720 kg/m^3
L	Along-axis Dike Length	2 km
k	Elastic Response of Magma Chamber	1.1×10^{-3} Pa/Kg
g	Acceleration of Gravity	10 m/s
$\Delta\rho$	Difference in Crustal and Magma Density	Varies; 30 – 255 kg/m^3
η	Magma Viscosity	10^2 Pa s

The system of equations was solved using the Runge-Kutta Solver in Matlab (version 7.2), varying crustal density (i.e., $\Delta\rho$), initial magma pressure (p_m), and crustal stress (σ). The time step selected was sufficiently small so that the solution did not depend on time. Because magma density (ρ) is incorporated into the scaling units, initial magma pressure was referenced to the scaling unit for pressure (p_u) in models varying crustal density and stress, in order to make an equal comparison ($p_i / p_u = 1$). In models varying magma pressure and crustal stress, a crustal density of 2800 kg/m^3 was used. Initial magma pressure varied from ~1.5 MPa to ~16 MPa; Crustal stress varied from ~2.5 to 16 MPa. In all models, initial conditions for dike initiation were satisfied and each dike achieved a finite, peak height.

The Matlab script calls on a file containing the equations (idaeqns.m):

```
%idaeqns.m
% Function defining diking equations from Ida, 1999
% To be called up in Fourth Order Runge-Kutta solution
% Main program called Ida.m

function dy=idaeqns(t,y)
```

```
global G sigma f U v n rho k L; % Declare as a global parameters to define
%elsewhere

dy = zeros (3, 1); % Column vector that matches dimensions of y

% Substitute expression for sigmam into equations for h, a, and pm
% using scaled equations
dy(1) = (y(2)^2/(6*y(1)))*((G/2)*y(1)-y(3)-3*(sigma-(y(2)/y(1)))); %
y(1) = h
dy(2) = (y(2)^3*(y(3)+2*(sigma-y(2)/y(1))))/(2*y(1)^2); % y(2) = a
dy(3) = -(y(2)^3/(6*y(1)))*((G/2)*y(1)+2*y(3)+3*(sigma-(y(2)/y(1)))); %
y(3) = pm
```

The main Matlab code defines the intial conditions and runs the solver (Ida.m):

```
% Ida.m, modified 4/15/07
% Initially written 9/14/06
% Main program to use fourth order Runge-Kutta method
% Applied to function called 'idaeqns.m'
% Dike intrusion model from Ida, JGR, 1999
% Contributions made by Nick Hayman, Rachel Levy, Jaime Palter

global G sigma f U v n rho k L; % Initialize global variables

% Constants
v = 0.25; % Poisson's Ratio
n = 100; % Viscosity (PaS)
U=30; %Rigidity of crust (GPa)
rho = 2720; % Magma density (kg/m^3)
rockrho = 2875; % Host rock density (kg/m^3)
deltarho = rockrho - rho; % Difference in magma and crustal densities
%(kg/m^3)
f = 5; % Dimensionless parameter that relates mean elastic stress over
%dike length
K = 15; % Bulk modulus of magma (GPa)
R = 1000; % Radius of magma chamber (m)
k = 0.0011; % Elastic response of magma and chamber (Pa/kg)
L=2; % Along-axis dike length (km)
g = 10; % Gravity (m/s^2)

% Calculate Scaling Units
hu = (((f * U)/(pi * (1-v) * rho * L * k)))^0.5 % Height (km) scaled
pu = (g * deltarho * hu) % Pressure (10^3 Pa? hu still in km, not m) scaled
au = (pi * (1-v) * hu * pu)/(f * U) % Width (km) scaled
tu = ((n * (hu)^2))/(au^2 * pu) % Time (10^-3 s? pu in strange Pa units)
%scaled
Gu = g * deltarho % Buoyancy (Pa/m) scaled
```

```
% Initial Scaled Parameters; user-defined
G_Gu = 1; % Buoyancy
h_hu = 0.001; % Scaled initial height
p_pu = 1; % Scaled initial pressure
sigma_pu = 3; % Scaled initial external stress
tf_tu = 1000; % Scaled model duration, larger = smaller timestep

% Calculate Initial Conditions
G = G_Gu * Gu; % Numerical value of G
h0 = h_hu * hu % Numerical value of h (km)
pm0 = p_pu * pu % Numerical value of p (Pa)
sigma = sigma_pu * pu % Numerical value of tectonic stress (Pa)
a0 = ((h0*(sigma+(pm0/3)))+(h0*(sigma+(pm0/2))))/2 % Numerical
%value of width (m) from inequality 35

% Time Step
t0 = 0; % at time=0
tf = tf_tu * tu; % time (sec) at end of model

% Vectorize Initial Conditions
y0 = [h0 a0 pm0];

% Use the 4th order Runge-Kutta solver to solve the idaeqns.m function
% Use default settings, but change time step and tolerance with options
later
[t,y] = ode15s('idaeqns',[t0 tf],y0);
sigmam = sigma - y(:,2)./y(:,1);

% Scale the variables
hscale = y(:,1)./hu; % h scaled
tscale = t./tu; % t scaled
sigmamscale = sigmam./pu;
pmscale = y(:,3)./pu;
ascale = y(:,2)./au;

%Find peak dike height
h_max=max(y(:,1)) % return the maximum value of scaled height
hu; %return scaled height
h_peak = h_max * hu % output maximum height in km

%end
```

References

Acocella, V., M. Porreca, M. Neri, E. Massimi, and M. Mattei, Propagation of dikes at Vesuvio (Italy) and the effect of Mt. Somma, *Geophys. Res. Lett.*, 33, doi:10.1029/2005GL025590, 2006.

Alabaster, T., J.A. Pearce, and J. Malpas, The volcanic stratigraphy and petrogenesis of the Oman ophiolite complex, *Contrib. Mineral. Petrol.*, 81, 168-183, 1982.

Alt, J.C., Low-temperature alteration of basalts from the Hawaiian Arch, Leg 136, in *Proceedings ODP, Sci. Results*, 136, 133-146, Ocean Drilling Program, College Station, TX, 1993.

Alt, J., and ODP Leg 148 Scientists, *Proceedings ODP, Initial Reports*, 136, Ocean Drilling Program, College Station, TX, 1993.

Alt, J.C., H. Kinoshita, L.B. Stokking, and P.J. Michael (Eds.), *Proceedings of the Ocean Drilling Program, Sci. Results*, 148, 512 pp., Ocean Drilling Program, College Station, TX, 1996.

Anderson, R.N., J. Honorez, K. Becker, et al. (Eds.), *Proceedings ODP, Initial Reports*, 83, 529 pp., Ocean Drilling Program, College Station, TX, 1996.

Andrews, A.J., Low temperature fluid alteration of oceanic layer 2 basalts, DSDP Leg 37, *Canadian J. of Earth Sci.*, 14, 911-926, 1977.

Asimow, P.D., and M.S. Ghiorso, Algorithmic modifications extending MELTS to calculate subsolidus phase relations, *American Mineralogist*, 83, 1127-1132, 1998.

Autio, L.K., and J.M. Rhodes, Costa Rica Rift zone basalts: Geochemical and experimental data from a possible example of multistage melting, in *DSDP Init. Repts.*, 69, 729-745, U.S. Government Printing Office, Washington, 1983.

Autio, L.K., J.W. Sparks, and J.M. Rhodes, Geochemistry of Leg 111 basalts: intrusive feeders for highly depleted pillows and flows, in *Proc. ODP, Sci. Results*, 11, edited by K. Becker, H. Sakai, et al., Ocean Drilling Program, College Station, TX, 1989.

Auzende, J.M., M. Cannat, P. Gente, J.P. Henriet, T. Juteau, J.A. Karson, Y. Lagabrielle, and M.A. Tivey, Deep layers of mantle and oceanic crust exposed along the southern wall of the Kane Fracture Zone: submersible observations, *C.R. Acad. Sci. Ser.*, 317, 1641-1648, 1993.

Bach, W., E. Hegner, J. Erzinger, M. Satir, Chemical and isotopic variations along the superfast spreading East Pacific Rise from 6 to 30 degrees S, *Contrib. Mineral. Petrol.*, 116, 365-380, 1994.

Bach, W., J. Erzinger, J.C. Alt, and D.A. Teagle, Chemistry of the lower sheeted dike complex, Hole 504B (leg 148): Influence of magmatic differentiation and hydrothermal alteration, in *Prod. ODP, Sci. Results*, 148, 39-55, edited by Alt, J.C., H. Kinoshita, L.B. Stokking, and P.J. Michael, Ocean Drilling Program, College Station, TX, 1996.

Batiza, R., Y. Niu, J.L. Karsten, W. Boger, E. Potts, L. Norby, and R. Butler, Steady and non-steady state magma chambers below the East Pacific Rise, *Geophys. Res. Lett.*, 23, 221-224, 1996.

Becker, K., H. Sakai, et al. (Eds.), Site 504, *Proc. ODP., Init. Repts.*, 111, 35-251, 1988.

Bedard, J.H., A procedure for calculating the equilibrium distribution of trace elements among the minerals of cumulate rocks, and the concentration of trace elements in the coexisting liquids, *Chem. Geol.*, 118,143-153, 1994.

Bottinga, Y., and D.F. Weill, Densities of silicate systems calculated from partial molar volumes of oxide components, *American J. of Science*, 269, 169-182, 1970.

Brewer, T.S., W. Bach, and H. Furnes, Geochemistry of lavas from Hole 896A, in *Prod. ODP, Sci. Results*, 148, 39-55, edited by Alt, J.C., H. Kinoshita, L.B. Stokking, and P.J. Michael, Ocean Drilling Program, College Station, TX, 1996.

Buck, W.R., S.M. Carbotte, and C.Z. Mutter, Controls on extrusion at mid-ocean ridges, *Geology*, 25, 935-938, 1997.

Buck, W.R., P. Einarsson, and B. Brandsdóttir, Tectonic stress and magma chamber size as controls on dike propagation: Constraints from the 1975-1984 Krafla rifting episode, *J. Geophys. Res.*, 111, doi:10.1029/2005JB003879, 2006.

Byerly, G., The nature of differentiation trends in some volcanic rocks from the Galapagos spreading center, *J. Geophys. Res.*, 85, 3797-3810, 1980.

Canales, J., R.S. Detrick, S. Carbotte, G.M. Kent, J.B. Diebold, A. Harding, J. Babcock, M. Nedimovic, and E. van Ark, Upper crustal structure and axial topography at intermediate-spreading ridges: Seismic constraints from the Southern Juan de Fuca Ridge, *J. Geophys. Res.*, 110, doi:10.1029/2005JB003630, 2005.

Cann, J.R., M.G. Langseth, J. Honnorez, R.P. VonHerzen, S.M. White, et al., *Init. Repts. DSDP*, 69, Ocean Drilling Program, College Station, TX, 1996.

Cheatham, M., W.F. Sangrey, and W.M. White, Sources of error in external calibration ICP-MS analysis of geological samples and improved nonlinear drift correction procedure, *Spectrochim. Acta, 48B*, E487-E506, 1993.

Christeson, G.L., G.M. Purdy, and G.J. Fryer, Seismic constraints on shallow crustal emplacement processes at the fast spreading East Pacific Rise, *J. Geophys. Res.*, 99, 17957-17974, 1994.

Cogne, J.P., J. Francheteau, V. Courtillot, and Pito93 Scientific Team, Large rotation of the Easter Microplate as evidenced by oriented paleomagnetic samples from the ocean floor, *Earth Planet. Sci. Lett.*, 136, 213-222, 1995.

Constantin, M., R. Hekinian, D. Bideau, and R. Hebert, Construction of the oceanic lithosphere by magmatic intrusions; petrological evidence from plutonic rocks formed along the fast-spreading East Pacific Rise, *Geology*, 24, 731-734, 1996.

Coogan, L.A., K. M. Gillis, C.J. MacLeod, G.M. Thompson, and R. Hekinian, Petrology and geochemistry of the lower ocean crust formed at the East Pacific Rise and exposed at Hess Deep, *Geochem. Geophys. Geosyst.*, 3, doi:10.1029/2001GC000230, 2002.

Cormier, M.-H, and K.C. Macdonald, East Pacific Rise 18º-19ºS: Asymmetric spreading and ridge reorientation by ultrafast migration of axial discontinuities, *J. Geophys. Res.*, 99, 543-564, 1994.

Cotsonika, L.A., M.R. Perfit, D.S. Stakes, and W.I. Ridley, The occurrence and origin of andesites and dacites from the southern Juan de Fuca Ridge, 2005 Joint Assembly, AGU, New Orleans, LA, 23-27 May, 2005.

Danyushevsky, L.V., The effect of small amounts of H_2O on crystallization of mid-ocean ridge and backarc basin magmas, *J. Volc. Geotherm. Res.*, 110, 265-280, 2001.

Delaney, P.T., Heat transfer during emplacement and cooling of mafic dykes, in *Mafic dyke swarms*, Geol. Assoc. Can. Spec. Pap. 34, edited by H.C. Halls and W.H. Fahrig, 31-46, 1987.

Delaney, J.R., H.P. Johnson, and J.L. Karsten, The Juan de Fuca Ridge hot spot propagating rift system: New tectonic, geochemical, and magnetic data, *J. Geophys. Res.*, 86, 11747-11750, 1981.

Delaney, J.F., F.N. Spiess, W.E. Colony, J.L. Karsten, D.E. Kelley, and P. Nehlig, A complete deep-tow swath map of south-facing "wall" of the Blanco Trough, Juan de Fuca Region, *Trans. Am. Geophys. Un.*, 68, 1402, 1987.

Delaney, J.R., D.S. Kelley, M.D. Lilley, D.A. Butterfield, J.A. Baross, W.S.D. Wilcock, R.W. Embley, and M. Summit, The quantum event of oceanic crustal accretion: Impacts of diking at mid-ocean ridges, *Science*, 281, 222-230, 1998.

Dewey, J.F., and J.M. Bird, The origin and emplacement of the ophiolite suite: Appalachian ophiolites in Newfoundland, *J. Geophys. Res.*, 76, 3179-3180, 1971.

Dick, H.J.B., J. Erzinger, L.B. Stokking, and et al., *Proc. ODP, Init. Repts.*, 140, Ocean Drilling Program, College Station, TX, 1992.

Dilek, Y., E. Moores, D. Elthon, and A. Nicolas (eds.), Ophiolites and oceanic crust: New insights from field studies and the ocean drilling program, *GSA Special Paper 349*, 552 pp., 2000.

Dixon, J.E., D.A. Clague, and J.-P. Eissen, Gabbroic xenoliths and host ferrobasalt from the southern Juan de Fuca Ridge, *J. Geophys. Res.*, 91, 3795-3820, 1986.

Dziak, R.P., C.G. Fox, and A.E. Schreiner, The June-July 1993 seismo-acoustic event at CoAxial segment, Juan de Fuca Ridge: Evidence for a lateral dike injection, *Geophys. Res. Lett.*, 22, 135-138.

Einaudi, F., P.A. Pezard, J.J. Cochemé, C. Coulon, C. Laverne, and M. Godard, Petrography, geochemistry, and physical properties of a continuous extrusive section from the Sarami Massif, Semail Ophiolite, *Mar. Geophys. Res.*, 21, 387-407, 2000.

Einaudi, F., M. Godard, P. Pezard, J.J. Cochemé, C. Coulon, T. Brewer, and P. Harvey, Magmatic cycles and formation of the upper oceanic crust at spreading centers: Geochemical study of a continuous extrusive section in the Oman ophiolite, *Geochem. Geophys. Geosyst.*, 4, doi:10.1029/2002GC000362, 2003.

Embley, R.W., and D.S. Wilson, Morphology of the Blanco transform fault zone N-E Pacific: implication for it tectonic evolution, *Mar. Geophys. Res.*, 14, 25-45, 1992.

Embley, R.W., W.W. Chadwick, M.R. Perfit, M.C. Smith, and J.R. Delaney, Recent eruptions on the CoAxial segment of the Juan de Fuca Ridge: Implications for mid-ocean ridge accretion processes, *J. Geophys. Res.*, 105, 16501-16525, 2000.

Fornari, D.J., M.R. Perfit, A. Malahoff, and R. Embley, Geochemical studies of abyssal lavas recovered by DSRV *Alvin* from Eastern Galapagos Rift, Inca Transform, and Ecuador Rift 1. Major element variations in natural glasses and spatial distribution of lavas, *J. Geophys. Res.*, 88, 10519-10529, 1983.

Francheteau, J., P. Patriat, J. Segoufin, R. Armijo, M. Doucoure, A. Yelles-Chaouche, J. Zukin, S. Almant, D. Naar, and R. Searle, Pito and Orongo fracture zones: the northern and southern boundaries of the Easter Microplate (Southeast Pacific), *Earth. Planet. Sci. Lett.*, 89, 363-374, 1988.

Francheteau, J., R. Armijo, J.-L. Cheminee, R. Hekinian, and P. Lonsdale, 1 Ma East Pacific Rise oceanic crust and uppermost mantle exposed by rifting in Hess Deep (equatorial Pacific Ocean), *Earth Planet. Sci. Lett.*, 101, 281-295, 1990.

Francheteau, J., R. Armijo, J.-L Cheminee, R. Hekinian, P. Lonsdale, and N. Blum, Dyke complex of the East Pacific Rise exposed in the walls of Hess Deep and the structure of the upper oceanic crust, *Earth Planet. Sci. Lett.*, 111, 109-121, 1992.

Francheteau, J., D. Naar, R. Armijo, J.-P. Cogne, M. Constantin, J. Girardeau, R. Hekinian, R. Hey, and R. Searle, Black smoker discovered, Pito Seamount near Easter microplate propagator tip, *Eos Trans. Am. Geophys. Un.*, 75, 322, 1994.

Gast, P.W., Trace element fractionation and the origin of tholeiitic and alkaline magma types, *Geochim. Cosmochim. Acta*, 32, 1057-1068, 1968.

Ghiorso, M.S., and R.O. Sack, Chemical mass transfer in magmatic processes IV. A revised and internally consistent thermodynamic model for the interpolation and extrapolation of liquid-solid equilibria in magmatic systems at elevated temperatures and pressures, *Contrib. Mineral. Petrol.*, 119, 197-212, 1995.

Godard, M., J.M. Dautria, and M. Perrin, Geochemical variability of the Oman ophiolite lavas: relationships with spatial distribution and paleomagnetic directions, *Geochem. Geophys. Geosyst.*, 4, doi:10.1029/2002GC000452, 2003.

Goldstein, S.J., M.R. Perfit, R. Batiza, D.J. Fornari, and M.T. Murrell, Off-axis volcanism at the East Pacific Rise detected by uranium-series dating of basalts, *Nature*, 367, 157-159, 1994.

Gudmundsson, A., Emplacement and arrest of sheets and dikes in central volcanoes, *J. Volcanol. Geotherm. Res.*, 116, 279-298, 2002.

Green, T.H., and A.E. Ringwood, Crystallization of basalt and andesite under high pressure hydrous conditions, *Earth Planet. Sci. Lett.*, 3, 481-489, 1968.

Hamelin, B., B. Dupre, and J. Allegre, Lead-strontium isotopic variations along the East Pacific Rise and the Mid-Atlantic Ridge, *Earth Planet. Sci. Lett.*, 67, 340-350, 1984.

Handschumacher, D.W., R.H. Pilger, J.A. Forman, and J.F. Campbell, Structure and evolution of the Easter plate, *Mem. Geol. Soc. Am.*, 154, 63-76, 1981.

Hawkins, J.W., Geology of supra-subduction zones – Implications for the origin of ophiolites, in *Ophiolite concept and the evolution of geological thought*, GSA Special Paper 373, edited by Y. Dilek and S. Newcomb, Geological Society of America, 2003.

Hayman, N.W., and J.A. Karson, Fault-controlled fluid flow regimes along the East Pacific Rise (EPR): Geologic views through tectonic windows, *Geol. Soc. Amer. Abstracts with Programs*, 38, 17, 2006.

Heft, K.L., and K.M. Gillis, Fluid flow and hydrothermal alteration patterns in sheeted dikes at Pito Deep, *AGU Fall meeting Abstracts*, 584, 2005.

Hekinian, R., J. Francheteau, R. Armijo, J.-P. Cogné, M. Constantin, J. Girardeau, R. Hey, D. Naar, and R. Searle, Petrology of the Easter microplate region in the South Pacific, *J. Volc. Geotherm. Res.*, 72, 259-289, 1996.

Hess, P.C., Origins of igneous rocks, 336 pp, Harvard University Press, Cambridge, Mass, 1989.

Hey, R.N., D.F. Naar, M.C. Kleinrock, W.J. Phipps Morgan, E. Morales, and J.G. Schilling, Microplate tectonics along a superfast seafloor spreading system near Easter Island, *Nature*, 317, 320-325, 1985.

Hooft, E.E. and R.S. Detrick, The role of density in the accumulation of basaltic melts at mid-ocean ridges, *Geophys. Res. Lett.*, 20, 423-426, 1993.

Hooft, E.E., H. Schouten, and R.S. Detrick, Constraining crustal emplacement processes from the variation in seismic layer 2A thickness at the East Pacific Rise, *Earth Planet. Sci. Lett.*, 142, 289-310, 1996.

Hooft, E.E., R.S. Detrick, and G.M. Kent, Seismic structure and indicators of magma budget along the southern East Pacific Rise, *J. Geophys. Res.*, 102, 319-327, 1997.

Humphris, S., W. Melson, and R. Thompson, Basalt weathering on the East Pacific Rise and the Galapagos spreading center, Deep Sea Drilling Project Leg 54, in DSDP *Init. Repts.*, 54, edited by B.R. Rosendahl, R. Hekinian, et al., 773-787, 1980.

Ida, Y., 1999, Effects of crustal stress on the growth of dikes: conditions of intrusion and extrusion of magma, *J. Geophys. Res.*, 104, 17897-17909, 1999.

Ishikawa, T., N. Kazuya, and S. Umino, Boninitic volcanism in the Oman ophiolite: Implications for thermal condition during transition from spreading ridge to arc, *Geology*, 30, 899-902, 2002.

Juteau, T., D. Bideau, O. Dauteuil, G. Manach, D.D. Naidoo, P. Nehlig, H. Ondreas, M.A. Tivey, K.X. Whipple, and J.R. Delaney, A submersible study in the Western Blanco Fracture Zone, N.E. Pacific: Structure and evolution during the last 1.6 Ma, *Mar. Geophys. Res.*, 17399-430, 1995.

Kappel, E.S., and W.B.F. Ryan, W.B.F., Volcanic episodicity and a non-steady state rift valley along northeast spreading centers: Evidence from Sea MARC I, *J. Geophys. Res.*, 9113925-13940, 1986.

Karson, J.A., Internal structure of oceanic lithosphere: a perspective from tectonic windows, in *Faulting and Magmatism at Mid-Ocean Ridges*, Geophysical Monograph Series 106, edited by W. R. Buck et al., 27-58, American Geophysical Union, 1998.

Karson, J.A., Geologic structure of the uppermost oceanic crust created at fast- to intermediate-rate spreading centers, *Ann. Rev. Earth Planet Sci. Lett.*, 30, 347-384, 2002.

Karson, J.A., E.M. Klein, S.D. Hurst, C.E. Lee, P.A. Rivizzigno, D. Curewitz, A.R. Morris, and Hess Deep '99 Scientific Party, Structure of uppermost fast-spread oceanic crust exposed near Hess Deep, *Geology*, 20, 685-688, 2002a.

Karson, J.A., M.A. Tivey, and J.R. Delaney, Internal structure of uppermost oceanic crust along the Western Blanco Transform Scarp: implications for subaxial accretion and deformation at the Juan de Fuca Ridge, *J. Geophys. Res.*, 107, doi:10.1029/2000JB000051, 2002b.

Kent, G.M., A. J. Harding, J.A. Orcutt, R.S. Detrick, J.C. Mutter, and P. Buhl, Uniform accretion of oceanic crust south of the Garrett transform at 14º15'S on the East Pacific Rise, *J. Geophys. Res.*, 99, 9097-9116, 1994.

Kinzler, R.J., and T.L. Grove, Primary magmas of mid-ocean ridge basalts. 2. Applications, *J. Geophys. Res.*, 97, 6907-6926, 1992.

Klein, E.M., and C.H. Langmuir, Global correlations of ocean ridge basalt chemistry with axial depth and crustal thickness, *J. Geophys. Res.*, 92, 8089-8115, 1987.

Klein, E.M., C.H. Langmuir, and H. Staudigel, Geochemistry of basalts from the Southeast Indian Ridge, 115°E-138°E, *J. Geophys. Res.*, 96, 2089-2107, 1991.

Lange, R.A., and I.S.E Carmichael, 1990, Thermodynamic properties of silicate liquids with an emphasis on density, thermal expansion and compressibility, in *Modern methods of igneous petrology*, Min. Soc. Am. Rev. in Mineralogy, edited by J. Nicholls and K. Russell, 24, 25-64, 1990.

Langmuir, C.H., Geochemical consequences of in situ crystallization, *Nature*, 420, 199-205, 1989.

Lister, J.R., and R.C. Kerr, Fluid-mechanical models of crack propagation and their application to magma transport in dykes, *J. Geophys. Res.*, 96, 10049-10077, 1991.

Lonsdale, P., Structural pattern of the Galapagos microplate and evolution of the Galapagos triple junctions, *J. Geophys. Res.*, 93, 13551-13574, 1988.

Macdonald, K.C., R.M. Haymon, S.P. Miller, J.-C. Sempere, and P.J. Fox, Deep-tow and Sea Beam studies of dueling propagating ridges on the East Pacific Rise near 20º40'S, *J. Geophys. Res.*, 93, 2785-2898, 1988.

Macdonald, K.C., D.S. Scheirer, and S.M. Carbotte, Mid-ocean ridges: Discontinuities, segments, and giant cracks, *Science*, 253, 986-994, 1991.

MacLeod, C.J., and D.A. Rothery, Ridge axial segmentation in the Oman Ophiolite: evidence from along-strike variations in the sheeted dyke complex, in *Ophiolites and their modern oceanic analogues*, Geological Society Special Publication 60, 39-63, 1992.

Mahoney, J.J., J.M. Sinton, M.D. Kurz, J.D. MacDougall, K.J. Spencer, and G.W. Lugmair, Isotope and trace element characteristics of a superfast spreading ridge: East Pacific Rise 13-23ºS, *Earth Planet. Sci. Lett.*, 121, 171-191, 1994.

Martinez, F., D.F. Naar, T.B. Reed(IV), and R.N. Hey, Three-dimensional SeaMARC II, gravity, and magnetics study of large-offset rift propagation at the Pito rift, Easter microplate, *Mar. Geophys. Res.*, 13, 255-285, 1991.

Minster, J.F., and C.J. Allegre, Systematic use of trace elements in igneous processes part III: Inverse problem of batch partial melting in volcanic suites, *Contrib. Mineral. Petrol.*, 68, 37-52, 1978.

Moores, E.M., and F.J. Vine, The Troodos massif, Cyprus, and other ophiolites as oceanic crust: evaluation and implications, *Philos. Trans. R. Soc. London Ser. A*, 268, 443-466, 1971.

Moores, E.M., Origin and emplacement of ophiolites, *Rev. Geophys. Space Phys.*, 20, 735-760, 1982.

Miyashiro, A., The Troodos ophiolitic complex was probably formed in an island arc, *Earth Planet. Sci. Lett.*, 19, 218-224, 1973.

Morgan, L.A., J.A. Karson, N.W. Hayman, R.J. Varga, and S.D. Hurst, Internal structure of basaltic lavas and sheeted dikes in 3 Ma super-fast EPR crust exposed at Pito Deep, *Eos. Trans. AGU*, 86, Fall Meet. Suppl., Abstract T33D-0588, 2005.

Myashita, S., Y. Adachi, and S. Umino, Along-axis magmatic system in the northern Oman ophiolite: Implications of compositional variations of the sheeted dike complex, *Geochem. Geophys. Geosyst.*, 4, doi:10.1029/2001GC000235, 2003.

Naar, D.F., and R.N. Hey, Tectonic evolution of the Easter Microplate, *J. Geophys. Res.*, 96, 7961-7993, 1991.

Naar, D.F., F. Martinez, R.N. Hey, T.B. Reed(IV), and S. Stein, Pito rift: How a large-offset rift propagates, *Mar. Geophys. Res.*, 13, 287-309, 1991.

Naidoo, D.D., Accretion of the upper oceanic crust, Ph.D. dissertation, Univ. of Washington, Seattle, Washington, 1998.

Natland, J.H., and R.A. Pockalny, Ultra-slow propagating ridges at eastern Pacific microplates, *Eos Trans. AGU* 87, Fall Meet. Suppl., Abstract V23E-0697, 2006.

Natland, J.H., A.C. Adamson, C. Laverne, W. Melson, and T. O'Hearn, A compositionally nearly steady-state magma chamber at the Costa Rica Rift: evidence from basalt glass and mineral data, Deep Sea Drilling Project sites 501, 504, and 505, in *DSDP Init. Repts.*, 68, 1983.

Nicolas, A., Structure of Ophiolites and Dynamics of Oceanic Lithosphere, 367 pp., Kluwer Acad., The Netherlands, 1989.

Nicolas, A., F. Boudier, and B. Ildefonse, Evidence from the Oman ophiolite for active mantle upwelling beneath a fast-spreading ridge, *Nature*, 370, 51-53, 1994.

Niu, Y., D.G. Waggoner, J.M Sinton, and J.J. Mahoney, Mantle source heterogeneity and melting processes beneath seafloor spreading centers: East Pacific Rise 18º-19ºS, *J. Geophys. Res.*, 101, 27711-27733, 1996.

Pallister, J.S., and C.A. Hopson, Semail ophiolite plutonic suite: field relations, phase variation and layering and a model of a spreading magma chamber, *J. Geophys. Res.*, 86, 2593-2644, 1981.

Pariso, J.E., and H.P. Johnson, Magnetic properties and oxide petrography of the sheeted dike complex in Hole 504B, in *Proc. ODP, Sci. Results*, 111, 159-166, 1989.

Parrish, R.R., J.C. Roddick, W.D. Loveridge, and R.W. Sullivan, Uranium-lead analytical techniques at the geochronology laboratory, *Geol. Survey Canada Paper*, 82, 3-7, 1987.

Pedersen, R.B., and H. Furnes, Nd- and Pb-isotopic variations through the upper oceanic crust in DSDP/ODP Hole 504B, Costa Rica Rift, *Earth Planet. Sci. Lett.*, 189, 221-235, 2001.

Perfit, M.R., D.J. Fornari, A. Malahoff, and R.W. Embley, Geochemical studies of abyssal lavas recovered by DSRV Alvin from eastern Galapagos Rift, Inca Transform, and Ecuador Rift: 3. Trace element abundances and petrogenesis, *J. Geophys. Res.*, 88, 10551-10572, 1983.

Perfit, M.R., D.J. Fornari, M.C. Smith, J.F. Bender, C.H. Langmuir, and R.M. Haymon, Small-scale spatial and temporal variations in mid-ocean ridge crest magmatic processes, *Geology*, 22, 375-379, 1994.

Perfit, M.R., and WW. Chadwick, Magmatism at mid-ocean ridges: constraints from volcanological and geochemical investigations, in *Faulting and Magmatism at Mid-Ocean Ridges*, Geophys. Monograph Series, vol. 106, edited by W.R. Buck, P. T. Delaney, J.A. Karson, and Y. LaGabrielle, pp. 59-116, AGU, Washington DC, 1998.

Perk, N.W., L.A. Coogan, J.A. Karson, E.M. Klein, and H. Hanna, Primitive high level plutonic rocks from Pito Deep: implications for accretion of the lower crust at the Southern East Pacific Rise, *Contrib. Mineral. Petrol., in press*.

Pito Deep Scientific Party, Structure and composition of super-fast spread crust at Pito Deep: AT11-23 Alvin, Jason II, DSL-120, *Cruise Report*, 2005.

Pockalny, R.A., R.L. Larson, C.T. Popham, J.H. Natland, L.J. Abrams, and L.J. Sonder, Morphology and tectonic evolution of Endeavor Deep, *Eos Trans. AGU*, Fall Meet. Suppl., Abstract T13B-1355, 2004.

Pollard, D.D., Elementary fracture mechanics applied to the structural interpretation of dykes, *Geol. Assoc. Can. Spec. Pap.*, 34, 5-24, 1987.

Pollock, M.A., E.M. Klein, J.A. Karson, and M.A. Tivey, Temporal and spatial variability in the composition of lavas exposed along the Western Blanco Transform Fault, *Geochem. Geophys. Geosyst.*, 6, doi:10.1029/2005GC001026, 2005.

Regelous, M., Y. Niu, J.I. Wendt, R. Batiza, A. Greig, and K.D. Collerson, Variations in the geochemistry of magmatism on the East Pacific Rise at 10°30'N since 800 ka, *Earth Planet. Sci. Lett.*, 168, 45-63, 1999.

Reynolds, J.F., C.H. Langmuir, J.F. Bender, K.A. Kastens, and W.B.F. Ryan, Spatial and temporal variability in the geochemistry of basalts from the East Pacific Rise, *Nature*, 359, 493-499, 1992.

Reynolds, J.F., and C.H. Langmuir, Petrological systematics of the Mid-Atlantic Ridge south of Kane: Implications for ocean crust formation, *J. Geophys. Res.*, 102, 14915-14946, 1997.

Riddihough, R.P., Recent movement of the Juan de Fuca plate system, *Nature*, 284, 6980-6995, 1984.

Rochette, P., L. Jenatton, C. Dupuy, F. Boudier, and I. Reuber, Diabase dikes emplacement in the Oman ophiolite: a magnetic fabric study with reference to geochemistry, in *Ophiolite genesis and evolution of the oceanic lithosphere*, edited by U. Peters et al., 55-82, 1991.

Rubin, A.M., Propagation of magma-filled cracks, *Ann. Rev. Earth Planet. Sci.*, 23, 287-336, 1995.

Ryan, M., Neutral buoyancy and the mechanical evolution of magmatic systems, in *Magmatic Processes: Physicochemical Principles*, edited by B.O. Mysen, 259-287, 1987.

Ryan, M., Neutral buoyancy and the structure of mid-ocean ridge magma reservoirs, *J. Geophys. Res.*, 98, 22321-22338, 1993.

Schouten, H., M.A. Tivey, D.J. Fornari, and J.R. Cochran, Central anomaly magnetization high: Constraints on the volcanic construction and architecture of seismic layer 2A at a fast spreading mid-ocean ridge, the EPR at 9°30'-50'N, *Earth Planet. Sci. Lett.*,169, 37-50, 1999.

Searle, R.C., R.I. Rusby, J. Engeln, R.N. Hey, J. Zukin, P.M. Hunter, T.P. LeBas, H.J. Hoffman, and R. Livermore, Comprehensive sonar imaging of the Easter Microplate, *Nature*, 341, 701-705, 1989.

Shaw, D.M., Trace element fractionation during anatexis, *Geochim. Cosmochim. Acta*, 34, 237-243, 1970.

Shervais, J.W., D.L. Kimbrough, P. Renne, B.B. Hanan, B. Murchey, C.A. Snow, M.M. Zoglman Schuman, and J. Beaman, Multi-stage origin of the Coast Range ophiolite, California: Implications for the life cycle of supra-subduction zone ophiolites, *Int. Geol. Rev.*, 46, 289-315, 2004.

Sinton, J.M. and P. Fryer, Mariana Trough lavas from 18ºN: Implications for the origin of back-arc basalts, *J. Geophys. Res.*, 92, 12782-12802, 1987.

Sinton. J.M., D.S. Wilson, D.M. Christie, R.N. Hey, and J.R. Delaney, Petrologic consequences of rift propagation on oceanic spreading ridges, *Earth Planet. Sci. Lett.*, 62, 193-207, 1983.

Sinton, J.M., S.M. Smaglick, J.J. Mahoney, and K.C. Macdonald, Magmatic processes at superfast spreading mid-ocean ridges: glass compositional variations along the East Pacific Rise 13º-23ºS, *J. Geophys. Res.*, 96, 6133-6155, 1991.

Sinton, J.M., and R.S. Detrick, Mid-ocean ridge magma chambers, *J. Geophys. Res.*, 97, 197-216, 1992.

Sinton, J.M., E. Bergmanis, K. Rubin, R. Batiza, T.K.P. Gregg, K. Gronvold, K. Macdonald, and S. White, Volcanic eruptions on mid-ocean ridges: New evidence from the superfast-spreading East Pacific Rise, 17 º-19 º S, *J. Geophys. Res.*, 107, doi:10.1029/2000JB000090, 2002.

Sisson, T.W. and T.L. Grove, Experimental investigations of the role of H_2O in calc-alkaline differentiation and subduction zone magmatism, *Contrib. Mineral. Petrol.*, 113, 143-166, 1993.

Smith, M.C., M.R. Perfit, and I.R. Jonasson, Petrology and geochemistry of basalts from the southern Juan de Fuca Ridge: Controls on the spatial and temporal evolution of mid-ocean ridge basalt, *J. Geophys. Res.*, 99, 4787-4812, 1994.

Soule, S.A., D.J. Fornari, M.R. Perfit, M.A. Tivey, W.I. Ridley, and H. Schouten, Channelized lava flows at the East Pacific Rise crest 9-10° N: the importance of off-axis lava transport in developing the architecture of young oceanic crust, *Geochem. Geophys. Geosyst.*, 6, doi:10.1029/2005GC000912, 2005.

Sparks, R.S.J., P. Meyer, and H. Sigurdsson, Density variation amongst mid-ocean ridges basalts: Implications for magma mixing and the scarcity of primitive lavas, *Earth Planet. Sci. Lett.*, 46, 419-430, 1980.

Stakes, D.S., M.R. Perfit, M.A. Tivey, D. Caress, T.M. Ramirez, and N. Maher, The Cleft Revealed: Geologic, magnetic and morphologic evidence for construction of upper oceanic crust along the southern Juan de Fuca Ridge, *Geochem. Geophys. Geosyst.*, 2005.

Staudigel, H., J.S. Gee, L. Tauxe, and R.J. Varga, Shallow intrusive directions of sheeted dikes in the Troodos ophiolite, *Geology*, 20, 841-844, 1992.

Stewart, M.A., E.M. Klein, and J.A. Karson, Geochemistry of dikes and lavas from the north wall of the Hess Deep Rift: Insights into the four-dimensional character of crustal construction at fast spreading mid-ocean ridges, *J. Geophys. Res.*, 107(B10), 2238,doi:10.1029/2001JB000545, 2002.

Stewart, M.A., E.M. Klein, J.A. Karson, and J.G. Brophy, 2003, Geochemical relationships between dikes and lavas at the Hess Deep Rift: Implications for magma eruptibility, *J. Geophys. Res.*, 108(B4), 2184, doi:10.1029/2001JB001622, 2003.

Stolper, E., and S. Newman, The role of water in the petrogenesis of Marina trough magmas, *Earth Planet. Sci. Lett.*, 121, 293-325, 1994.

Stolper, E., and D. Walker, Melt density and the average composition of basalt, *Contrib. Mineral. Petrol.*, 74, 7-12.

Sun, S.-S., and W.F. McDonough, Chemical and isotopic systematics of oceanic basalts: Implications for mantle composition and process, *In* A.D. Saunder and M.J. Norry, *Magmatism in the Ocean Basins,* Geol. Soc. Spec. Publ., 42, 3313-3345, 1989.

Tierney, S.E., Distribution and composition of lavas from the southern Cleft Segment of the Juan de Fuca Ridge: tectonomagmatic evolution of a ridge-transform intersection, Masters Thesis, University of Florida, 2003.

Tilton, G.R., C.A. Hopson, and J.E. Wright, Uranium-lead isotopic ages of the Semail ophiolite, Oman, with applications to Tethyan Sea ridge tectonics, *J. Geophys. Res.*, 86, 2763-2776, 1981.

Tivey, M.A., Vertical magnetic structure of ocean crust determined from near-bottom magnetic field measurements, *J. Geophys. Res.*, 101, 20275-20296, 1996.

Tivey, M.A., H.P. Johnson, C. Fleutelot, S. Hussenoeder, R. Lawrence, C. Waters, and B. Wooding, Direct measurement of magnetic reversal polarity boundaries in a cross-section of oceanic crust, *Geophys. Res. Lett.*, 25, 3631-3634, 1998.

Umino, S., S. Yanai, A.R. Jama, Y. Nakamura, and J.T. Iiyama, The transition from spreading to subduction: evidence from the Semail Ophiolite, northern Oman mountains, in *Ophiolites: oceanic crustal analogues*, *Proceedings of the symposium "Troodos 1987"*, edited by J. Malpas, E.M. Moores, A. Panayiotou, and C. Xenophontos, 375-384, 1990.

Umino, S., S. Miyashita, F. Hotta, and Y. Adachi, Along-strike variation of the sheeted dike complex in the Oman ophiolite: Insights into subaxial ridge segment structures and the magma plumbing system, *Geochem. Geophys. Geosyst.*, 4, doi:10.1029/2001GC000235, 2003.

Varga, R.J., J. Gee, and H. Staudigel, Dike surface lineations as magma flow indicators within the sheeted dike complex of the Troodos ophiolite, Cyprus, *J. Geophys. Res.*, 103, 5241-5256, 1998.

Vera, E.E., and J.B. Diebold, Seismic imaging of oceanic layer 2A between 9 º 30'N and 10º on the East Pacific Rise from two-ship wide-aperture profiles, *J. Geophys. Res.*, 99, 3031-3041, 1994.

Weaver, J., and C.H. Langmuir, Calculation of phase equilibrium in mineral-melt systems, *Comp. and Geosc.*, 16, 1-19, 1990.

Wilson, D.S., R.N. Hey, C. and Nishimura, Propagation as a mechanism of reorientation of the Juan de Fuca Ridge, *J. Geophys. Res.*, 89, 9215-9225, 1984.

Wilson, D.S., and Leg 206 Science Party, Drilling to Gabbro in Intact Ocean Crust, *Science*, doi:10.1126/science.1126090, 2006.

Workman, R.K., and S.R. Hart, Major and trace element composition of the depleted MORB mantle (DMM), *Earth Planet. Sci. Lett.*, 231, 53-72.

Biography

Meagen was born on June 30, 1979 in Hackettstown, NJ. Her passion for the natural world began as she grew up in rural northwest NJ, on the doorstep of the Appalachians, and expanded in high school, after relocating to the mountains of West Virginia. Meagen attended Marshall University in Huntington, WV where, in 2001, she graduated summa cum laude with a B.S. in Environmental Science and Geology. Inspired by an enthusiastic petrology professor, Meagen developed a love for all things igneous.

Meagen pursued her graduate career in high-temperature geochemistry through the study of mid-ocean ridges, truly one of the last frontiers on Earth. She has presented her research at numerous professional conferences and has published her work on the Temporal and Spatial Variability in the Composition of Lavas exposed along the Western Blanco Transform Fault in the journal *Geochemistry, Geophysics, Geosystems* in 2005. Meagen has spent a great deal of time at sea, and has had the fortunate experience of traveling to the ocean bottom in *Alvin*.

While in graduate school, Meagen developed an interest in geoscience education. She was a Preparing Future Faculty Fellow and spent the last year of her graduate career teaching at Dickinson College, a liberal arts college in Carlisle, PA.